ABSTRACT

Title of Dissertation: MEASUREMENT OF THE TOP QUARK PRODUCTION CROSS SECTION IN PROTON-ANTIPROTON COLLISIONS AT 1.8 TEV CENTER OF MASS ENERGY

Peter Dominic Tamburello, Doctor of Philosophy, 1998

Dissertation directed by: Professor Andrew Baden
Department of Physics

A measurement of the production cross section for $t\bar{t}$ quark pairs in $p\overline{p}$ collisions at $\sqrt{s} = 1.8$ TeV is reported. The data were taken with the DØ detector at the Fermilab Tevatron during the 1992-6 collider runs and constitute 108.3 pb^{-1} of integrated luminosity. The decay signature studied is $t\bar{t} \rightarrow e + \text{jets}$ with b-quark jets tagged by the presence of a muon. Five candidate events were found with an estimated background of about one event. Based on this signature the cross section $\sigma_{t\bar{t}}$ is measured to be $6.4^{+4.5}_{-2.9}\,(\text{stat.}) \pm 1.2\,(\text{sys.})\,\text{pb}$ assuming a top quark mass of 170 GeV/c^2.

MEASUREMENT OF THE TOP QUARK PRODUCTION CROSS SECTION IN PROTON-ANTIPROTON COLLISIONS AT 1.8 TEV CENTER OF MASS ENERGY

by

Peter Dominic Tamburello

Dissertation submitted to the Faculty of the Graduate School of the
University of Maryland at College Park in partial fulfillment
of the requirements for the degree of
Doctor of Philosophy
1998

Advisory Committee:

Professor Andrew Baden, Chair
Professor Nicholas Hadley
Professor Richard Herman
Professor Markus Luty
Professor Gregory Sullivan

DEDICATION

To Mom and Dad

ACKNOWLEDGEMENTS

This thesis was made possible by the work of the DØ Collaboration and the staffs of Fermilab and the collaborating institutions. Hundreds of people contributed to the design, construction, operation, and maintenance of the DØ detector and the Fermilab Tevatron and to the processing and interpretation of data from the experiment.

I am grateful to the University of Maryland High Energy Group for taking me on and supporting me as a graduate student. It was a pleasure working with all the members of this group. Thanks especially to my advisor, Drew Baden, for his patience, encouragement and perspective on the field of high energy physics. Thanks also to Nick Hadley, another good professorial influence. Thanks to Adam Lyon for selfless efforts to maintain the computer cluster which was crucial in carrying out this analysis.

This thesis benefitted from the expertise of the whole DØ Top Group. I particularly thank John Hobbs and Meena Narain for their essential help.

The person who directly contributed the most, by far, to getting this analysis off the ground was Bill Cobau. His help made the tricky tasks of operating in the Top Group and learning the ropes at DØ easy. I already miss working with him.

Thanks to Drew, Nick and Jim Cochran for valuable comments on the draft.

Thanks to Jane Hessing and Sally Megonigal for getting me through the university red tape countless times.

TABLE OF CONTENTS

LIST OF TABLES

LIST OF FIGURES

Chapter 1

Introduction

Among all of the particles of matter regarded as fundamental, the top quark is conspicuous because of its high mass: it is the only quark or lepton with a mass that is near the scale of electroweak symmetry breaking. The Standard Model (SM) of elementary particle physics attributes quark and lepton masses to a coupling with the same Higgs field that gives rise to the masses of the W and Z bosons [1]. However, this aspect of the theory has not been established experimentally, and it is intellectually unsatisfying because it provides no explanation for the spectrum of quark and lepton masses. The interactions of the top quark therefore invite particular scrutiny for clues to physics beyond the SM.

Searches for the top quark began soon after the discovery of the b-quark in 1977 [2]. Even before the weak isospin of the b-quark was first measured, it was natural to suppose, following the example of the previously known quarks, that the b-quark would prove to be a member of a weak-isospin pair. Experiments to test this idea sought to produce and detect the b-quark's postulated partner, the top quark. From the late 1970's throughout the 1980's, searches at increasingly higher energy e^+e^- and $p\overline{p}$ colliders around the world found no evidence for top quark production, resulting in increasingly higher lower bounds on the top quark mass. By 1994, results from the DØ experiment at the Fermilab Tevatron had pushed the mass limit to 131 GeV/c^2 (revised to 128 GeV/c^2 in 1995 due to a recalibration of the luminosity [4]).

While the top quark eluded direct searches, indirect evidence accumulated that it would eventually appear when the mass reach of experiments extended high enough. In 1984, crucial measurements of $b\bar{b}$ production in e^+e^- collisions found the forward-backward asymmetry to be just as predicted by the SM with the b-quark as the $T = -1/2$ member of a doublet [5]. This result made a persuasive case for the existence of the top quark. The question became whether the top quark remained unseen because it was too heavy to be produced, or because it was decaying in an unexpected way. In 1989, early estimates from global fits to electroweak data, sensitive to the top mass through radiative corrections, suggested a value in the ranges 140^{+43}_{-52} GeV/c^2 [7] or 132^{+31}_{-37} GeV/c^2 [8]. Lower mass limits that were independent of the top quark decay mode, based on indirect measurements of the W boson width, reached 51 GeV/c^2 by 1991 [9].

In 1994, the CDF collaboration reported finding evidence in data from the 1992-1993 Tevatron collider run for top quark production with a cross section of $13.9^{+6.1}_{-4.8}$ pb and a mass of $174 \pm 10^{+13}_{-12}$ GeV/c^2, but they concluded that the statistical significance of the signal was not sufficient to "firmly establish the existence of the top quark" [10]. DØ data from the same run was analyzed with an eye toward high mass top production and showed a less significant excess of candidate events, corresponding to a cross section of 8.2 ± 5.1 pb if attributed to production of a 180 GeV/c^2 top quark [11]. The first part of the following Tevatron run increased the DØ and CDF data samples by a factor of almost four. In February 1995, both collaborations announced discovery of the top quark. DØ found a mass of 199^{+19}_{-21}(stat.)± 22(sys.) GeV/c^2 and a cross section of 6.4 ± 2.2 pb [12]. CDF found a mass of 176 ± 8(stat.)± 10(sys.) GeV/c^2 and a cross section of $6.8^{+3.6}_{-2.4}$ pb [13]. By the end of the collider run in 1996 the amount of accumulated data had doubled again. DØ has now submitted for publication measurements of the top quark mass [14, 15] and production cross section [16] using the full data set.

The cross section measurement is the most basic test of top quark interactions. In the SM top quarks are produced primarily in $t\bar{t}$ pairs and decay almost exclusively through the process $t \to bW$. Each W boson subsequently decays to $l\nu_l$ ($l = e, \mu, \tau$), ud', or cs', and the quarks u, d, c, s and b yield jets of colorless particles. The decays of $t\bar{t}$ pairs are classified as dilepton, $l+$ jets or all-jets depending on whether both, one, or neither of the W bosons decays leptonically. The availability of alternative decay channels, such as $t \to H^+b$ [17], may appear as an anomalous branching ratio $BR(t\bar{t} \to ll)/(t\bar{t} \to l)$ ($l = e, \mu$) or a total cross section significantly lower than expected for the measured mass. An abnormally high cross section may be an indication of additional production mechanisms [18]. A deficit of B-flavored hadrons in top events could signal a fourth generation of quarks, since the branching fraction for $t \to Wb$ is constrained to be near one only if there are exactly three generations.

This thesis describes a measurement of the top quark production cross section based on the signature $e+$ jets where one of the jets is identified as originating from a b-quark. The analysis described here makes up one of the eight mutually exclusive channels in Reference [16], and is one of two which identify b-quarks.

In the next Chapter we survey the theoretical context within which this analysis proceeds, including a discussion of the challenges to studying top quarks at a hadron collider. Relevant features of the Tevatron and the DØ detector are reviewed in Chapter 3. Chapter 4 describes the trigger systems and particle identification. The selection of candidate $t\bar{t}$ events is discussed in Chapter 5 along with the estimation of backgrounds, acceptance and luminosity necessary for a determination of the cross section. Results of the present analysis and the combined results from all the signatures studied at DØ are summarized in Chapter 7.

Chapter 2

Theoretical Background

2.1 Particles and Forces

The most fundamental constituents of matter presently known are quarks and leptons. These particles have no known substructure. If they are composite objects, their binding energies must, in most cases, be greater than about one TeV [19], corresponding to a spatial size on the order of 10^{-18} meters.

Particles of matter influence one another through four known forces: the strong force, electromagnetism, the weak force, and gravity. All of these forces are described by field theories. Electromagnetism and the weak force are described in an interrelated way by the standard Electroweak Theory [1]. The strong force is described by Quantum Chromodynamics (QCD). Both the Electroweak Theory and QCD are relativistic quantum theories in which the dynamics can be derived from a gauge invariance postulate. Gravity is described, at macroscopic distance scales, by the theory of General Relativity. No viable quantum theory of gravity has yet been devised. However, the effects of gravity are expected to be negligible in the interactions of elementary particles in high energy physics experiments. There are presently no experimental results that contradict predictions of the Electroweak Theory, QCD, or General Relativity.

The Electroweak Theory and QCD together make up the Standard Model of particle physics. Table 2.1 lists the elementary particles in the minimal Standard Model.

	Name	Symbol	Mass [GeV/c^2]	Spin [$\hbar$]
Quarks				
	up	u	0.002–0.008	1/2
	down	d	0.005–0.015	1/2
	strange	s	0.1–0.3	1/2
	charm	c	1.0–1.6	1/2
	bottom	b	4.1–4.5	1/2
	top	t	172.0 ± 7.5	1/2
Leptons				
	electron neutrino	ν_e	$< 15 \times 10^{-9}$	1/2
	muon neutrino	ν_μ	< 0.00017	1/2
	tau neutrino	ν_τ	< 0.024	1/2
	electron	e	0.00051099907(15)	1/2
	muon	μ	0.105658389(34)	1/2
	tau	τ	$1.77700^{+0.00030}_{-0.00027}$	1/2
Bosons				
	photon	γ	$< 6 \times 10^{-25}$	1
	W bosons	$W^\pm$	80.33 ± 0.15	1
	Z boson	Z	91.187 ± 0.007	1
	gluons	g	$\leq$ a few $\times$ 0.001	1
	Higgs boson	H	> 58.4	0

Table 2.1: Elementary particles in the Standard Model and their intrinsic kinematic properties. The value of the top quark mass is from [15]; all other mass values are from [19]. The u, d, and s mass estimates are for the $\overline{\mathrm{MS}}$ "current-quark masses"; the c and b estimates are for the $\overline{\mathrm{MS}}$ "running" masses; the t value represents the pole mass. The photon and gluons are massless in the Standard Model. The uncertainties in the last two digits of the muon and electron masses are shown in parentheses after the values.

2.2 The Electroweak Theory

The Electroweak Theory has an SU(2)$\times$U(1) gauge symmetry. The right handed projections of the quark and lepton fields transform as singlets in the SU(2) space.

The left handed projections make up SU(2) doublets. The SU(2)×U(1) eigenstates and their eigenvalues are shown in Table 2.2. The weak isospin T is the eigenvalue

Dirac field component			T	T^3	Y	Q
$\begin{pmatrix} \nu_{eL} \\ e_L \end{pmatrix}$	$\begin{pmatrix} \nu_{\mu L} \\ \mu_L \end{pmatrix}$	$\begin{pmatrix} \nu_{\tau L} \\ \tau_L \end{pmatrix}$	$1/2$ $1/2$	$1/2$ $-1/2$	-1 -1	0 -1
ν_{eR}	$\nu_{\mu R}$	$\nu_{\tau R}$	0	0	0	0
e_R	μ_R	τ_R	0	0	-2	-1
$\begin{pmatrix} u_L \\ d'_L \end{pmatrix}$	$\begin{pmatrix} c_L \\ s'_L \end{pmatrix}$	$\begin{pmatrix} t_L \\ b'_L \end{pmatrix}$	$1/2$ $1/2$	$1/2$ $-1/2$	$1/3$ $1/3$	$2/3$ $-1/3$
u_R	c_R	t_R	0	0	$4/3$	$2/3$
d_R	s_R	b_R	0	0	$-2/3$	$-1/3$

Table 2.2: Electroweak eigenstates and eigenvalues. Each pair of states that makes up an SU(2) doublet is enclosed in parentheses. T, T^3, and Y are defined in the text. Q is the electric charge in units of the absolute value of the charge of the electron.

of the SU(2) Casimir operator. T^3 is the eigenvalue of the third SU(2) generator. The hypercharge Y is the $U(1)$ generator. The down components of the quark doublets d'_L, s'_L, and b'_L are related to mass eigenstates by the CKM matrix V

$$\begin{pmatrix} d'_L \\ s'_L \\ b'_L \end{pmatrix} = \begin{pmatrix} V_{ud} & V_{us} & V_{ub} \\ V_{cd} & V_{cs} & V_{cb} \\ V_{td} & V_{ts} & V_{tb} \end{pmatrix} \begin{pmatrix} d_L \\ s_L \\ b_L \end{pmatrix}. \tag{2.1}$$

The three columns of quarks and leptons in Table 2.2 are called, from left to right, the first, second, and third generations. The three generations have identical SU(2)×U(1) properties.

The SU(2) invariance of the Lagrangian requires three vector fields: W^1, W^2, and W^3. The doublets couple to these fields with strength g. The U(1) gauge field B couples to a left (right) handed quark or lepton with strength $g'Y_L$ ($g'Y_R$), where Y_L (Y_R) is the hypercharge. To respect SU(2) invariance, Y_L is the same for components of the same doublet.

The condition $Y_R = Y_L + 2\,T^3$ is adopted. It guarantees that the Lagrangian will separate in such a way that one piece has the form for quantum electrodynamics—i.e., left and right handed bi-spinors couple to a vector field with the same strength. The electromagnetic field is thus identified as $A = B\cos\theta_W + W^3\sin\theta_W$, where $\tan\theta_W = g'/g$; the electric charge of a particle is Qe, where $Q = Y_L/2 + T^3$ and $e = g\sin\theta_W$.

The combination $Z = -B\sin\theta_W + W^3\cos\theta_W$ (orthogonal to A) represents an additional field, which couples to left and right handed states with different strengths. The electrically charged fields $W^\pm = W^1 \mp iW^2$ mediate transitions between members of a doublet. The $W^\pm$, Z and A coupling constants are of comparable size, but the $W^\pm$ and Z interactions are suppressed at low energy by the $W^\pm$ and Z masses.

Explicit mass terms for the quarks and leptons would break the SU(2) symmetry, and explicit mass terms for gauge bosons are generically not gauge invariant. Such terms are disallowed because the gauge invariance of the Lagrangian protects the theory's renormalizability. To give masses to the $W^\pm$, Z, quarks, and leptons, while preserving the gauge invariance of the Lagrangian, the SU(2)$\times$U(1) symmetry is spontaneously broken by means of the Higgs mechanism. The Higgs field ϕ in the minimal theory is an SU(2) doublet consisting of two complex scalar components. It contributes a potential energy term $\mu^2\phi^\dagger\phi + \lambda(\phi^\dagger\phi)^2$ to the Lagrangian. For $\mu^2 < 0$ and $\lambda > 0$, ϕ has degenerate ground states defined by $\langle 0|\phi^\dagger\phi|0\rangle = -\mu^2/\lambda \equiv v/2$. The set of ground states is invariant under SU(2), but settling on any particular one of them breaks the symmetry. The actual ground state is defined to have $T^3 = -1/2$ and postulated to have $Y = 1$, so that its electric charge is zero and A remains massless. When ϕ is expressed in terms of deviations from the ground state, three of its degrees of freedom can be eliminated from the Lagrangian by gauge transformation. The eliminated degrees of freedom reappear as longitudinal polarization states of the $W^{\pm}$ and Z, for which mass terms arise corresponding to masses $M_W = gv/2$ and $M_Z = M_W/\cos\theta_W$ respectively. The fourth degree of freedom appears as a real scalar field, the Higgs boson H, with mass $m_H = v\sqrt{2\lambda}$. Gauge invariant couplings of ϕ to the quarks and leptons can also be added; after symmetry breaking, these terms give rise to masses m_f for quark or lepton flavor f and to couplings of f with H of strength $\propto m_f/v$.

The quark and lepton mass eigenstates are nearly the same; that is, the matrix V in Equation 2.1 is nearly diagonal. (The absolute value of V_{tb} is particularly close to one, between about 0.9989 and 0.9993 if there are only three generations [20].) Associating each mass state with its closest weak state, we can say that the masses of the quarks and leptons all (except perhaps for the neutrinos) increase with each generation. The non-zero off-diagonal elements of V mean that the quarks and leptons in the second and third generations decay by the charged interaction. For this reason, and because neutrinos only interact weakly, the everyday objects with which we are familiar consist principally of u, d, and e. (The d quarks would presumably decay also, if the u-d mass difference were not so small that a proton is lighter than a Δ^{++}.)

The Electroweak Theory is well tested experimentally. Measurements of the fine structure constant α_{EM}, the muon lifetime, and $e\nu_{mu}$ scattering determine the parameters e, v, and $\sin\theta_W$ respectively; this allowed the masses of the W and Z to be predicted before the particles were discovered. The Z mass, width, and its interactions with quarks and leptons have now been measured precisely. These measurements tightly over constrain parts of the theory, and they are sensitive to corrections beyond leading order perturbative calculations [21]. Some of the higher order corrections include effects which depend on the top quark mass m_t; this led to estimates of m_t that eventually proved consistent with the directly measured value. The part of the theory that is not well tested is the Higgs field. The Higgs boson has not been observed. Its couplings to quarks and leptons have not been measured.

Despite its success, several features of the Electroweak Theory beckon to be explained: Why are there three (or more) generations? Why does the electron have an even multiple of the electric charge of the down quark? Why is it the massive bosons that participate in parity violating interactions? What determines the values of the quark and lepton masses and mixings? Perhaps such questions will be answered. Perhaps the clues will be found in $p\overline{p}$ collisions.

2.3 QCD

The gauge group of Quantum Chromodynamics is SU(3). The theory contains eight massless vector bosons, known as gluons. Each flavor of quark, u,d,c,s,b, and t, has three internal degrees of freedom, conventionally labelled 'red,' 'green' and 'blue.' These 'color' states of a quark transform as an SU(3) triplet.

The color terminology reflects a (partial) analogy between ways QCD states combine and ways colors of light combine: white light is formed from an equal combination of red, green, and blue light, or from a color of light and its conjugate (such as red and cyan); similarly, QCD states that transfrom as an SU(3) singlet are formed from three quarks of different type, or from (the totally color symmetric combination of) a quark and its charge conjugate.

SU(3) singlets are important because experimental and theoretical evidence suggests that the QCD force confines a colored particle to within about 10^{-15} meters of other particles with which it forms a singlet. Free quarks or gluons have never been observed. Instead there are color neutral bound states of three quarks, such as the proton (uud), and bound states of quark-antiquark pairs, such as the π^+ ($u\overline{d}$). In a high energy interaction involving quarks or gluons, as may occur in proton-antiproton collisions, rather than a free colored particle, a shower of hadrons emerges along the direction of a scattered quark or gluon.

The strength of the QCD force is attributed to the self couplings of gluons, which result from the gauge group being non-abelian. In the case of three colors and six flavors of quarks, the gluon-gluon interactions cause the coupling constant to increase with decreasing momentum scale (or increasing distance). It is only for momentum transfers well above the scale of hadron binding energies that pertubative calculations can be made using QCD. Even then, non-perturbative effects make the theory difficult to test precisely. A recent review of QCD phenomenology and tests is given in [22].

2.4 Top Quark Production and Decay

The high value of m_t is not only interesting in its own right but is important to bear in mind because of its influence on the production of top quarks at the Tevatron and on their decay modes. At the Tevatron, top quarks are produced primarily in pairs through $q\overline{q} \to t\overline{t}$ and $gg \to t\overline{t}$. The former process contributes about 90% of the total rate because m_t is almost 20% of the Tevatron beam energy and it is mostly quarks which can be found with such a high fraction of the p or $\overline{p}$ momentum. The next to leading order calculation of the cross section for the gg process is over 70% higher than the leading order calculation. This is attributed to contributions from gluon radiation from initial state gluons [23]. Procedures to take these contributions into account have been implemented by several authors [23, 24, 25] and give results ranging from 4.7 pb to 5.8 pb assuming $m_t = 170$ GeV/c^2. The results are lower (higher) by about a factor of two for every 20 GeV/c^2 higher (lower) m_t is assumed to be. The value of the cross section is quite small compared to other processes, as seen in Figure 2.1. The amount of data

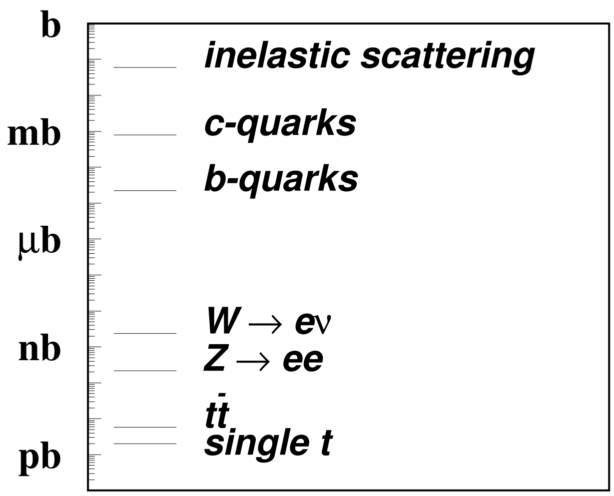

Figure 2.1: Cross sections for selected processes.

recorded by the DØ experiment represents a little more than 100 pb^{-1}of integrated luminosity, so the total number of $t\bar{t}$ pairs produced was about six hundred. This is to be compared to about six trillion inelastic $p\bar{p}$ interactions. Thus the challenge faced in the present analysis was to filter the data for the exceptionally rare signal events.

In the Electroweak Theory, top quarks decay almost exclusively to a W boson and b-quark; the branching fractions to Ws and Wd are lower by factors of 0.0025 and 10^{-4} respectively. Because the top quark mass is high, there is a lot of phase space available for decay products, resulting in a lifetime that is so short that the decay occurs before hadronization can take place [6]. The W boson subsequently decays to $l\nu_l$ ($l = e, \mu, \tau$), ud, or cs with branching fractions of 1/9 for each of the leptonic modes and 1/3 for each of the quark modes. The quarks u, d, c, s and b yield jets of hadrons. The decays of $t\bar{t}$ pairs are classified according to the decay products of the two W bosons into dilepton, single lepton and hadronic modes, depending on whether one both, or neither W decays leptonically. The easiest objects to measure in a detector are electrons and muons. Furthermore, the backgrounds levels of leptons from other processes are relatively small compared to the high rate of jets from scattering among quarks and gluons. As a result, the dilepton decay modes $e\mu$, ee and $\mu\mu$ and the single lepton ($l+\text{jets}$) decay modes $e\nu qq$ and $\mu\nu qq$ provide the best signatures. The jets of particles originating from the hadronization of quarks can be identified, but it is not generally possible to distinguish one type of quark from another or from jets arising from gluons. One useful exception is b-quarks. Amid the other hadrons in a b-quark jet is one carrying the b-quark itself, which decays by $b \to c\mu\nu$ about 11% of the time. Most jets from background processes contain only light flavors of hadrons and only rarely ($< 1\%$) include a muon with a significant amount of energy.

Chapter 3

Apparatus

3.1 Accelerator

This section outlines the principle stages in the process of accelerating protons and antiprotons at the Fermilab collider. The features of this process which impact directly on the data are noted. An introduction with more detail can be found in Reference [26].

Figure 3.1 shows the layout of the accelerator complex. The protons begin as hydrogen gas in a pressurized bottle. They are released into a chamber where the H_2 molecules dissociate into a plasma in the vicinity of a cathode. Protons land on the surface of the cathode and are knocked off again by other incoming protons. Sometimes a proton coming off the cathode carries with it a pair of electrons, forming an H^- ion. The H^- ions are extracted and fed into an electrostatic accelerator where their kinetic energy is increased from 18 keV to 750 keV through a potential difference produced by a Cockcroft-Walton generator. The H^- source and the electrostatic accelerator together are called the Preaccelerator. From the Preaccelerator the H^- ions move to a linear accelerator, the Linac, where the energy is increased to 400 MeV. After exiting the Linac the beam enters a 500 ft diameter synchrotron ring called the Booster.

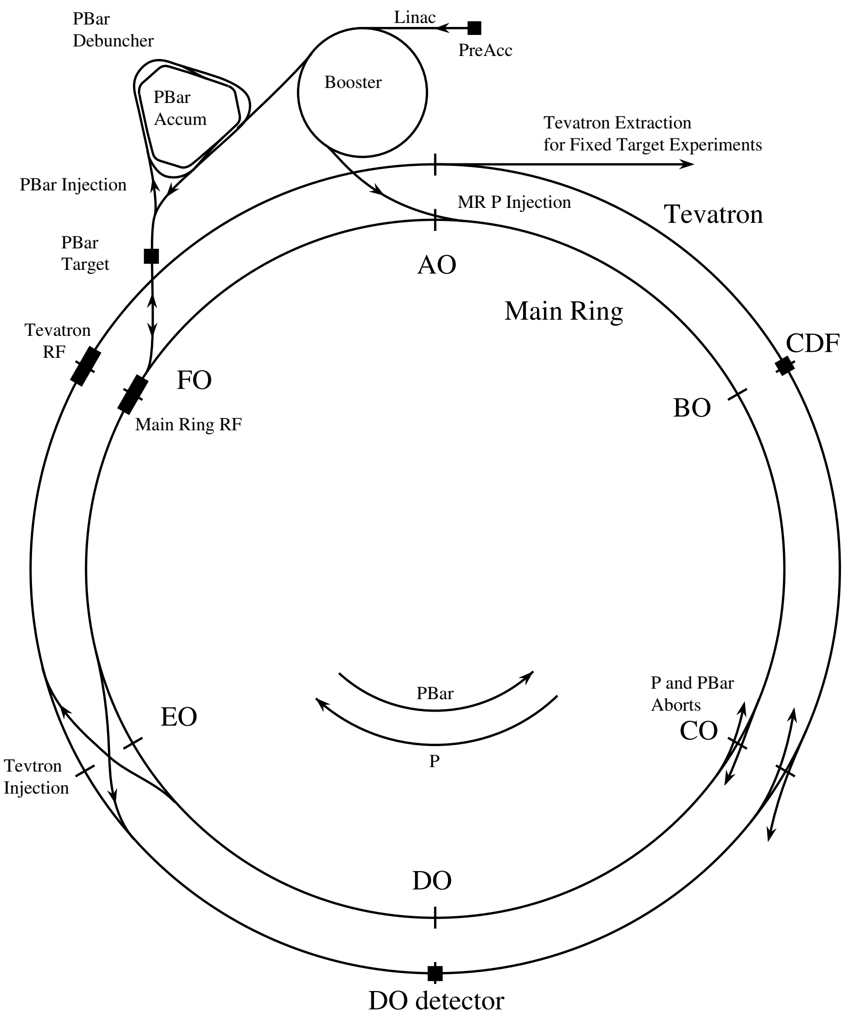

Figure 3.1: The Fermilab accelerator complex.

In a synchrotron, the beampipe forms a toroidal ring. Dipole magnets along the ring ensure that particles follow an approximately circular orbit. Once each orbit, the particles pass through an RF cavity where their energy is ramped up. The cavity frequency and the field strength of the dipole magnets are increased synchronously to keep the radius of the orbit constant. The beam is focused in the transverse direction by quadrapole magnet lensing. Longitudinal stability is maintained by matching the RF phase to the arrival of the bunches so that the slower particles encounter the accelerating field when it is at a higher amplitude than when the faster particles arrive. As the beam energy increases, a point is reached at which the wider orbit followed by higher momentum particles causes them to complete an orbit in more time than slower particles. At this point, called transition, the phase of the RF relative to the bunches must be shifted so that the beam is not defocused longitudinally.

To gather enough beam into the Booster it must be filled for longer than one period of revolution. However, as a consequence of Liouville's Theorem, it is normally impossible to put an additional bunch at exactly the same point in phase space as a previous one. To see this, imagine the Booster with the dipole bending magnets at discrete points along the ring and the beam traveling in a straight line between them. The initial round of beam could enter the ring on a line between two dipole locations if the first one were initially turned off, but once the first bunch comes back around the ring the magnet must be on. This problem is solved using a procedure called 'called exchange,' the principle of which is the following. A pair of adjacent dipole magnets with opposite parity is placed at a point along a straight section of the ring. The beam from the Linac is directed through the adjacent pair, tangent to the ring but with a slight outward offset so that it misses the bending magnet preceding the pair. The H^- beam curves inward toward the center of the ring $\pi/4$ radians while passing through the field of the first dipole of the pair, then promptly enters the second field and curves $\pi/4$ radians back. The net result is that the direction of the beam is unchanged but its position is shifted toward the ring so that it will intercept the next bending magnet. First, however, before it reaches the next magnet, the beam is passed through a thin foil which strips off the electrons; it is thus an H^+ beam which circulates around the ring. Before arriving back at the double dipole, the H^+ beam is given an offset radially toward the center of the ring. Upon passing through the double dipole, it is shifted outward and merges with the incoming beam from the Linac. This is why H^- is used in the first stages of the accelerator rather than H^+. After enough protons have been gathered, their energy is ramped up to 8 MeV and they are transferred to a 1 km radius synchrotron called the Main Ring.

The Main Ring serves a dual purpose: it is an injector for the final accelerator stage, the Tevatron; and it is the source of a 120 GeV proton beam used to produce antiprotons. In the latter mode, the Main Ring is filled, ramped up, and the entire beam is focused and dumped on a target once every 2.4 seconds. The hadronic debris emerging from the target includes about 20 antiprotons for every million incident protons. The antiprotons, with typical energies around 8 GeV, are focused and captured into a storage ring called the Debuncher. After an initial period of stochastic cooling in the Debuncher, the antiprotons are moved into another storage ring, the Accumulator, located in the same tunnel where they undergo further cooling and are held until a large enough batch has been gathered for use in the collider. Like the Booster, the Accumulator is connected to the Main Ring for transfer to the Tevatron.

When a 'stack' of about a trillion antiprotons is ready, protons are accelerated to 150 GeV in the Main Ring and transfered to the Tevatron. If all goes well, the antiprotons follow. The Tevatron, like the Main Ring, is a 1 km radius synchroton. The two are located in the same tunnel, the former about one meter below the latter. The main difference is that the Tevatron uses superconducting bending and focusing magnets which allow the beam energy to reach 900 GeV. It is presently the highest energy accelerator in the world. Viewed from above, protons travel clockwise around the Tevatron and antiprotons travel counterclockwise. Both beams are composed of six bunches each. The bunches are about 50 cm long and are spaced (nearly) evenly around the ring. Each proton (antiproton) bunch contains on the order of 10×10^{10} (5×10^{10}) particles. Two locations on the ring, denoted BØ and DØ, are the site of large detectors where the two beams are focused to a transverse radius of 40 μm and brought together to collide. The time between bunch crossings is 3.5 μs.

Over the course of the run, the accelerator delivered a total integrated luminosity of about 161 pb^{-1} for about 78% [1] of which unprescaled triggers at DØ were written to tape. The distribution of instantaneous luminosity $\dot{\mathcal{L}}$ at which high p_T data was accumulated is shown in Figure 3.2. The average number of inelastic

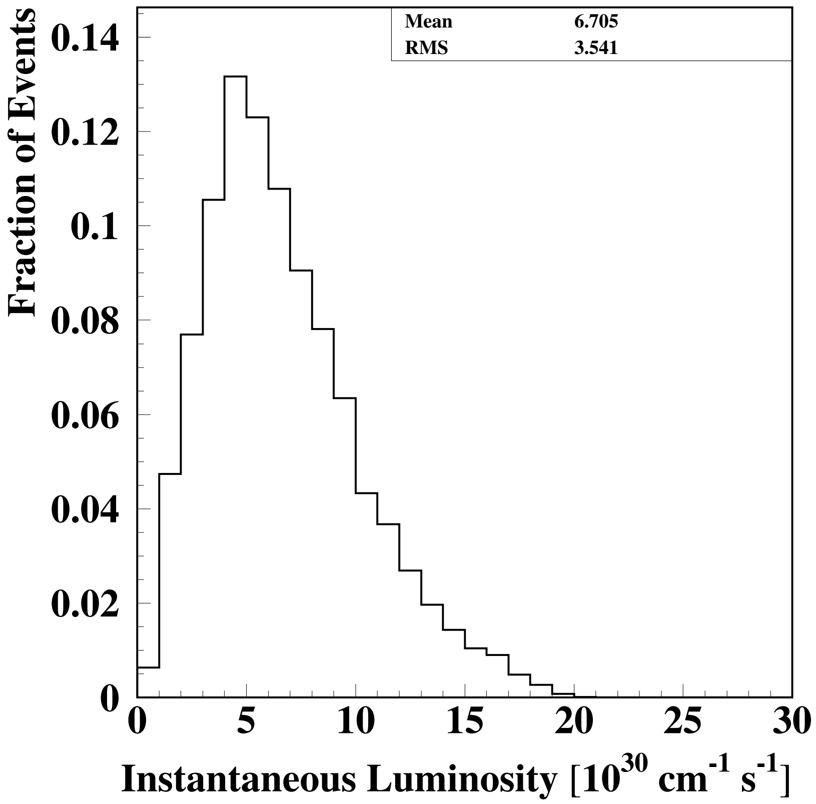

Figure 3.2: Distribution of instantaneous luminosity during Run 1.

interactions per crossing $\overline{n}$ is given by

$$\overline{n} = \dot{\mathcal{L}}\sigma\tau, \tag{3.1}$$

[1] Not including data taken while protons in the Main Ring were undergoing transition, see below and Section 5.2.

where τ is the time between crossings and σ, the inelastic cross section, is about 60 mb (see Appendix A) or 6×10^{-26} cm^2. At an instantaneous luminosity of about 5×10^{30} cm^{-1}s^{-1} there was an average of about one inelastic interaction per crossing. The number of interactions in randomly chosen crossings varies according to the Possion distribution, so for $\overline{n} = 1$ as many as three or more interactions would occur about 8% of the time. Furthermore, the tail in Figure 3.2 extends beyond 20×10^{30} cm^{-1}s^{-1}. Note that the high p_T interactions in which we are interested constitute a very small, specially chosen fraction of inelastic interactions, see Figure 2.1. Thus $\overline{n}$ gives the average number of *additional* interactions occurring in the crossing with an interesting event.

It takes several hours to produce a stack of antiprotons, so this is done while the previous batch are in the Tevatron colliding. Because the Main Ring is right above the Tevatron, there are complications introduced by colliding and stacking concurrently. At DØ, the Main Ring beam pipe makes a slight detour upwards to increase the separation to two meters; it thus passes through a part of the detector where the presence of a hole does not significantly affect the coverage. However, when the Main Ring bunches are passing through the detector or when there are losses in the beam a significant amount of noise can occur in the detector.

3.2 Detector

A detailed description of the DØ detector is given in Reference [27]. A cutaway view is shown in Figure 3.3. There are three main systems: the inner tracking chambers, the calorimeter, and the muon spectrometer. The detector is cylindrically symmetric about the Tevatron beam pipe, except for the muon system which is square viewed from the end. Consider the perspective in Figure 3.3 to be from inside the ring—the protons then enter from the lower left and the antiprotons

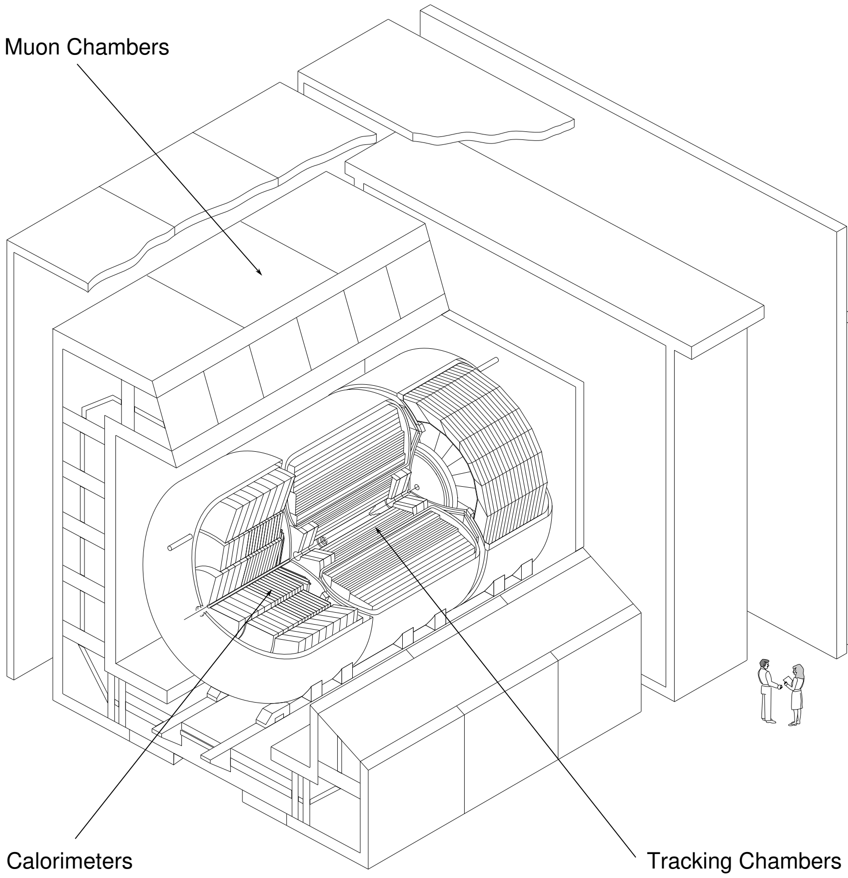

Figure 3.3: Cutaway view of the DØ detector.

from the upper right. The z-axis is along the direction of the proton beam, the y-axis points upward and the x-axis is radially outward from the center of the accelerator ring. The azimuthal angle ϕ is measured from the x-axis and the polar angle θ is zero along the positive z-axis. The pseudo-rapidity η, defined to be $-\ln(\tan(\theta/2))$, is often used in place of the polar angle θ because the difference in η between the trajectories of two highly relativistic particles is invariant under a boost in the z direction. The cylindrical radius coordinate $\sqrt{x^2+y^2}$ is denoted r.

3.2.1 Central Detectors

Figure 3.4 shows a cross-sectional r-z view of the central detectors. There are

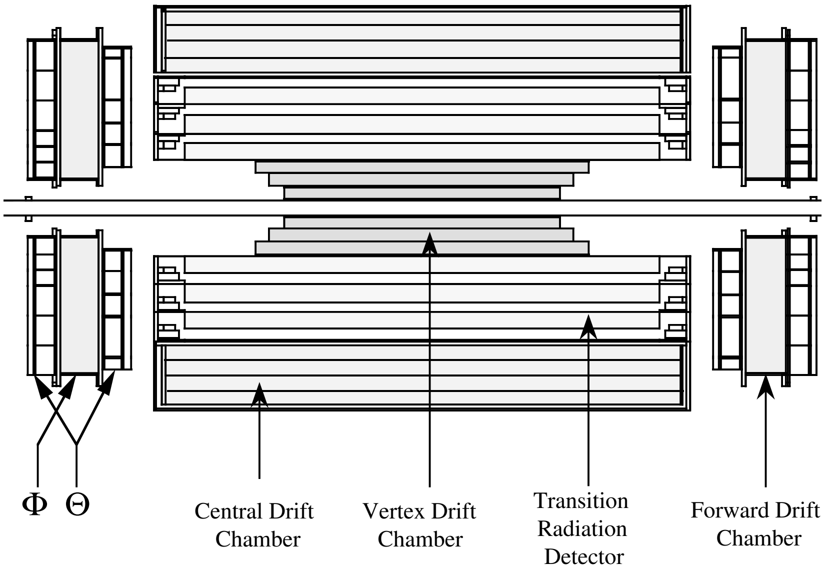

Figure 3.4: Central Detectors.

four subsystems. Nearest to the beampipe is a system of gas drift chambers (VTX) designed to measure the tracks of charged particles for use in vertex reconstruction. Surrounding the VTX is the transition radiation detector (TRD), used to discriminate between electrons and pions. The Central Drift Chambers (CDC), located between the TRD and central calorimeters, measure the position, direction and ionization deposited along charged particle tracks. The CDC extends to approximately $|\eta| = 1$; beyond there the Forward Drift Chambers (FDC) serve. There is no central magnetic field.

In general, a drift chamber operates in the following way [28]. The chamber contains a gas or mixture of gasses, and a sense wire. The sense wire is kept at high positive voltage, typically ~ 1 kV, with respect to the chamber boundary. There may be other electrodes present to shape the electric field. When an energetic charged particle passes through the chamber it leaves a trail of ionized gas along its path. The positive ions then drift in the direction away from the sense wire and the electrons drift toward the sense wire. In the immediate vicinity of the wire, typically within a few thicknesses, the field rapidly becomes very intense. As a result, after the drifting electrons have almost arrived at the wire they gain enough energy between collisions to cause further ionization, leading to a localized cascade of charge. As the positive ions from the avalanche recede from the sense wire they induce a voltage pulse which is read out. The difference in time between the passage of the particle through the chamber (basically the same as the time of the beam crossing), together with the known drift velocity in the gas, allow the distance of closest approach between the sense wire and the trajectory of the particle to be determined. If the drift field is not so high that the size of the cascade distorts the field, then the magnitude of the signal is proportional to the amount of ionization left by the original particle.

3.2.1.1 VTX

An r-ϕ view of a quadrant of the VTX is shown in Figure 3.5. The VTX consists of three concentric layers. The inner radius of the inner layer is 3.7 cm and the outer radius of the outer layer is 16.2 cm. The inner layer is 96.6 cm long and the outer layer is 116.8 cm long. The inner layer is divided into 16 cells in ϕ and the outer two layers are each divided into 32. Each cell contains eight sense wires. The sense wires are strung parallel to the beam in order to accurately measure the ϕ position of tracks. The z position of hits is measured by charge division; each end of the wire is read out and the relative size of the signals on the two ends indicates the relative distance from the chamber ends to the hit. The position resolution of hits measured in test beam is about 50 μm in the r-ϕ direction and 1 cm in the z direction. In practice, the charge division method is complicated by the presence of multiple hits per wire. The drift velocity of electrons in the VTX is about 7.3

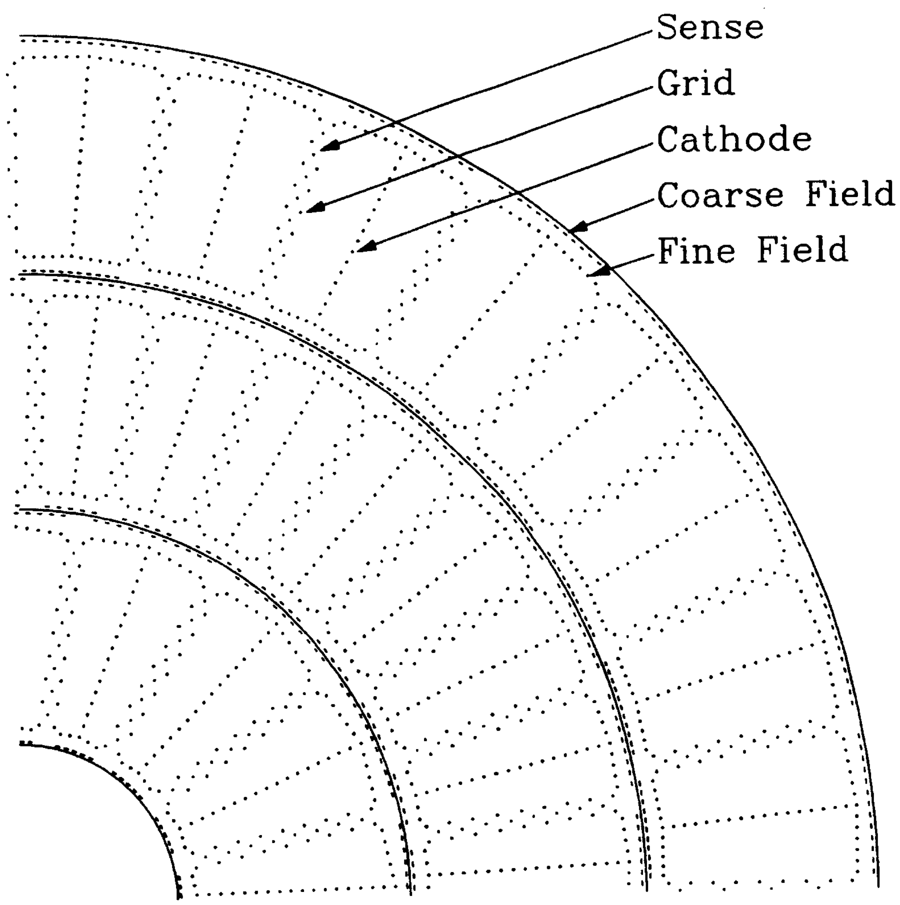

Figure 3.5: r-ϕ view of a quadrant of the Vertex Chamber

mm/μs so the maximum drift time within a cell, about 2.2 μs, is within the 3.5 μs between bunch crossings.

3.2.1.2 TRD

When a charged particle crosses the boundary between two media with different dielectric constants a small amount of its energy is lost to radiation. This energy, called transition radiation, generally emerges at an angle of about $1/\gamma$ with respect to the direction of motion of the particle. Most of the energy is emitted at low frequency but the frequency spectrum shifts higher as the γ of the particle increases

[19]. DØ uses transition radiation to aid in distinguishing between electrons ($\gamma = 4 \times 10^4$ for E=20 GeV) and pions ($\gamma = 140$ for E=20 GeV).

In the TRD, a stack of radiators is followed by a proportional drift chamber. The radiators are stacks of 393 18 μm thick foils of polypropylene separated by gaps of about 150 μm. The configuration is shown in Figure 3.6. For high energy

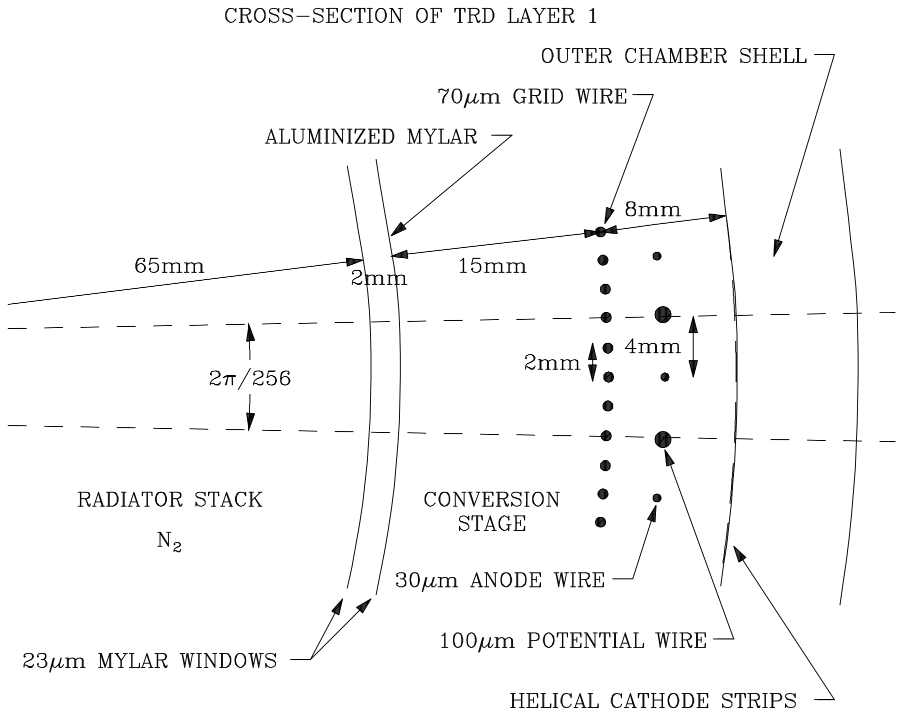

Figure 3.6: Transition Radiation Detector

electrons a substantial amount of the transition radiation is in the x-ray range, while for pions it is almost all at lower frequencies. The x-rays convert to e^+e^- pairs in the front of the drift chamber and the charge is accumulated at the anode. The TRD consists of three concentric sets of these radiator/detector systems.

3.2.1.3 CDC

An r-ϕ view of part of the CDC is shown in Figure 3.7. The CDC consists of four concentric layers. The inner radius is 49.5 cm and the outer radius is 74.5 cm.

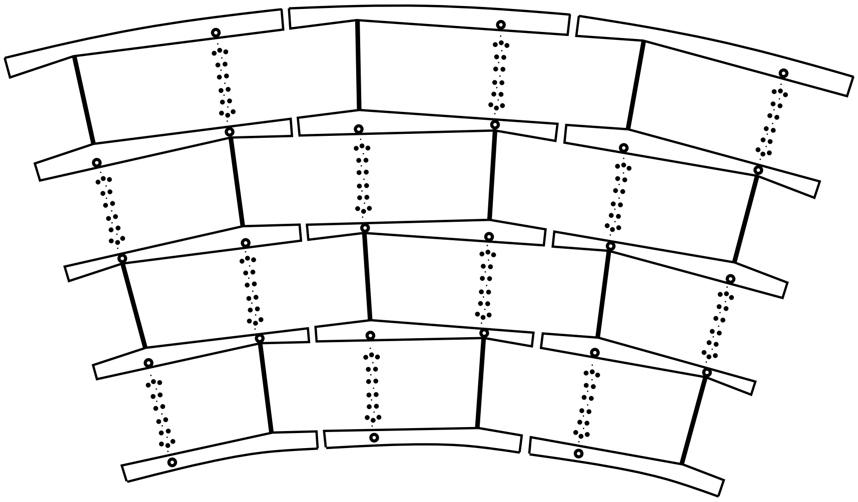

Figure 3.7: Central Drift Chamber

Each layer is 184 cm long and is divided into 32 cells in ϕ. There are seven sense wires and two delay lines per cell.

The delay lines are wire coils running through the interlayer shelf next to the first and last sense wire in each cell. They are used to measure the z positions of tracks. Hits on the adjacent sense wire induce a signal in the delay lines which propagates to each end at a speed of about 2.35 mm/ns. The signal is read out at both ends and the time difference gives the z coordinate.

The position resolution of hits measured in test beam is about 200 μm in r-ϕ and several mm in z. The drift velocity in the CDC is about 34 mm/μs for a maximum drift time in a cell of 2.2 μs.

3.2.1.4 FDC

There are two FDC systems, one at each end of the cylindrical central detector region. Each system consists of three modules: one with radially oriented sense wires to measure the ϕ coordinate and two with sense wires oriented to measure the θ coordinate. This arrangement is illustrated in Figure 3.8. The outer radius

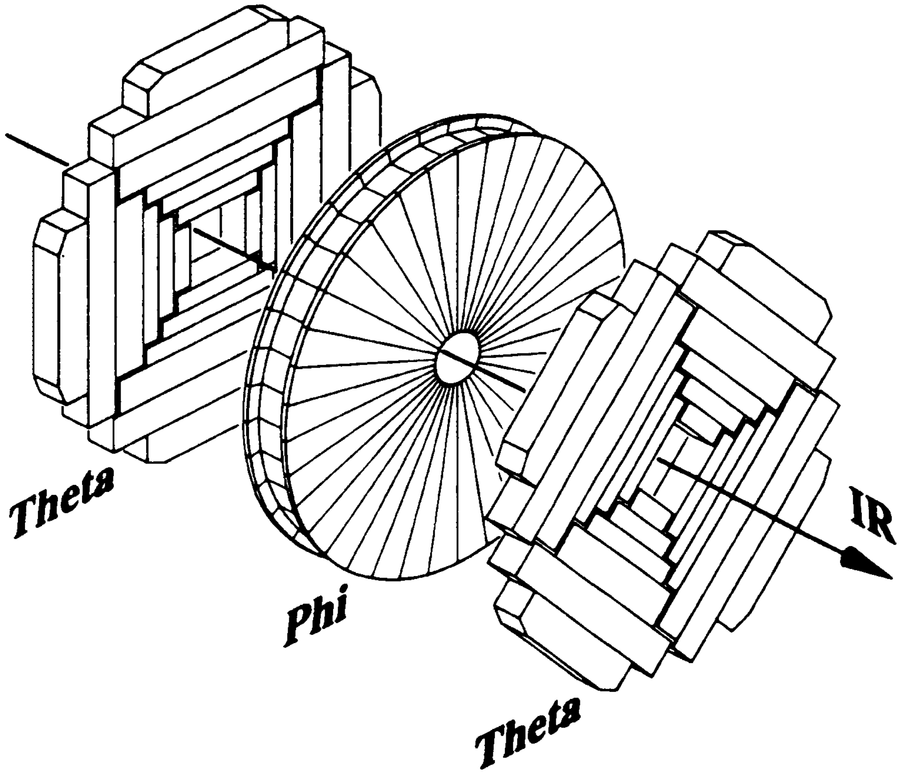

Figure 3.8: Forward Drift Chamber

of the modules is within 61 cm. The ϕ modules are divided into 36 radial sectors. Each sector contains 16 sense wires at different z locations. The θ modules consist of four sets of rectangular cells. Each cell has eight sense wires at different z locations. The θ cells include delay lines, as in the CDC, for a measurement of the hit position along the sense wires. The position resolution of hits measured in test beam is comparable to that achieved with the CDC for the direction perpendicular to the sense wires. The delay line resolution is about 4 mm. The maximum drift time in a cell or sector is 1.5 μs.

3.2.2 Calorimeters

Any charged particle passing through a material loses some energy to ionization. For an electron with energy greater than a few hundred MeV, however, the only significant mechanism for energy loss is photon radiation. In classical terms, the electron radiates as it is accelerated in the coulomb field of a nucleus. In this process, called bremsstrahlung, the initial energy of the electron is shared between the photon and the electron. The primary energy loss mechanism for high energy photons is conversion into an e^+e^- pair. As these processes repeat the energy of the original electron (or photon) becomes distributed among an exponentially increasing number of particles, called a shower. On average, the energy of an electron decreases as $\exp(-x/L_{rad})$ due to radiation as it moves a distance x through material. The quantity L_{rad}, called the radiation length, is a property of the material. The shower continues until the individual particle energies become so low that ionization becomes the main sources of energy loss. Ultimately then, most of the energy of the original particle does go into ionization. By measuring the amount of liberated charge the initial energy can be inferred. This is the basis of a calorimeter for electromagnetic particles. [28]

Particles other than electrons do not undergo bremsstrahlung (at the energies with which they are produced at the Tevatron) because they accelerate less in the nuclear coulomb field than do electrons. This is a result of their higher masses: the probability for bremsstrahlung scales as m^{-2}. Energetic hadrons therefore travel nearly unimpeded through material until undergoing a strong interaction with a nucleus. The typical length scale on which this occurs is called the nuclear interaction length λ. The interaction products may then go on to initiate further interactions and develop a shower of hadronic particles, some of the energy of which goes into measurable ionization. This is the basis of a calorimeter for hadronic particles.

In the DØ calorimeters, a layer of absorber (uranium, copper or steel) is followed by a 2.3 mm gap containing liquid argon (LAr) followed by a readout board in a repeating pattern as shown in Figure 3.9. Most of the shower development

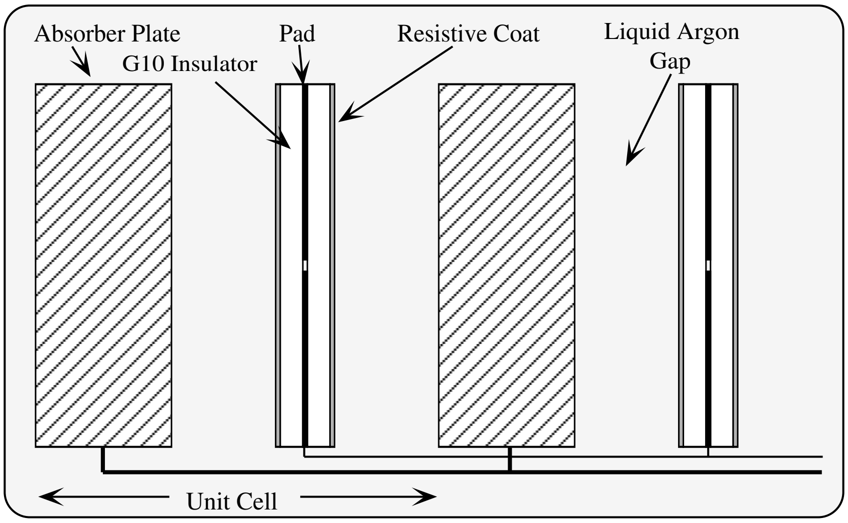

Figure 3.9: Structure of a calorimeter cell.

takes place in the absorber, which is chosen for its short radiation and interaction lengths. The resistive coat on the outer surfaces of the readout pads are kept at a high positive voltage to accumulate ionization from particles traveling through the liquid argon. The signal induced by this charge on the copper pad at the center of the board is read out. Liquid argon is used as the medium in which to sample the charge because it is not susceptible to variations in gain as a gas would be, and because it is not susceptible to radiation damage as scintillator would be. To keep the liquid argon cold, the calorimeters are contained in three steel cryostats, one for the Central Calorimeter (CC) and one for each End Calorimeter (EC) as shown in Figure 3.10. The CC begins just outside the Central Drift Chambers, at a radius of 78 cm, extends to a radius of about 2.5 m, and is about 3 m long. The two EC calorimeters cap the ends of the CC cylinder and extend down to a radius of a few cm.

There are three types of calorimeter layers: Electromagnetic (EM), Fine Hadronic (FH) and Coarse Hadronic (CH). The absorber in the EM and FH layers is

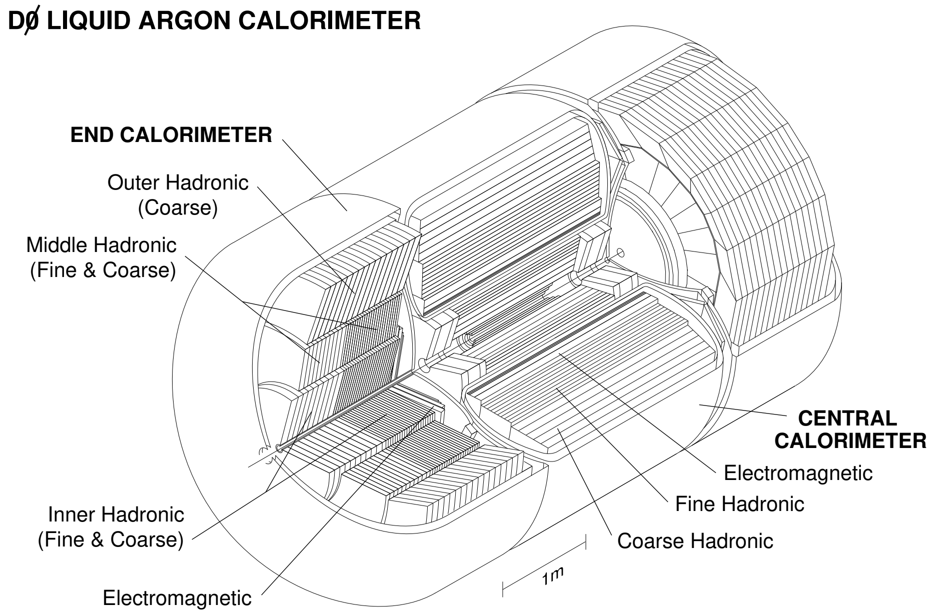

Figure 3.10: Cutaway view of the calorimeter geometry.

depleted uranium. The EM plates are 3 (4) mm thick in the CC (EC) and the signal boards are grouped in depth into four readout layers. The FH plates are 6 mm thick and are grouped into three (four) readout layers in the CC (EC). The CH absorber is 46.5 mm thick plates of copper (steel) in the CC (EC). The CC and inner EC CH sections are read out as one layer, while the outer CH section in the EC is read out as three. The signal boards in each type of layer are segmented transversely into dimensions of 0.1 in both η and ϕ; exceptions are the very forward sections of the EC, where the cells are 0.2×0.2, and the third EM layer, which has a granularity of 0.05×0.05 to better measure the shape of electromagnetic showers near the point of maximum particle multiplicity. The space between the CC and EC cryostats is instrumented with tiles of scintillator to improve the shower sampling there. Figure 3.11 shows an r-z view of one quadrant of the calorimeter system, indicating the segmentation into readout cells. The cells are arranged in

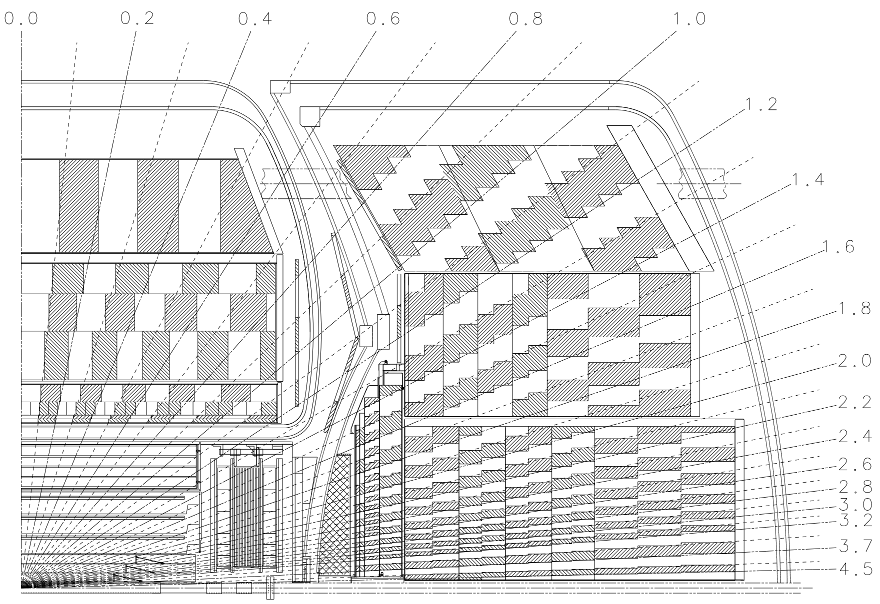

Figure 3.11: Side view of the calorimeter.

towers along lines emanating from the center of the interaction region to facilitate triggering and reconstruction for jets, electrons and photons.

The energy resolution σ for single charged pions measured in test beam as a function of the energy E (measured in GeV) is given by $(\sigma/E)^2 = 0.50^2/E$. For electrons the resolution is found to be $(\sigma/E)^2 = 0.015+0.16^2/E+(0.4/E)^2)$, where the first term was determined from a fit to the width of the mass of electron pairs in Z boson events [29] and the latter two were measured in test beam data.

3.2.3 Muon System

Ionization losses in the calorimeter can stop muons with energy below a few GeV but muons are too heavy to shower electromagnetically in the calorimeter and they do not interact hadronically. The muon lifetime, 2.2 μs, is long enough that they almost never decay in flight before exiting the detector. Because of the thickness of the DØ detector, see Figure 3.12, almost no particles other than muons emerge from the interaction region and pass through the muon system.

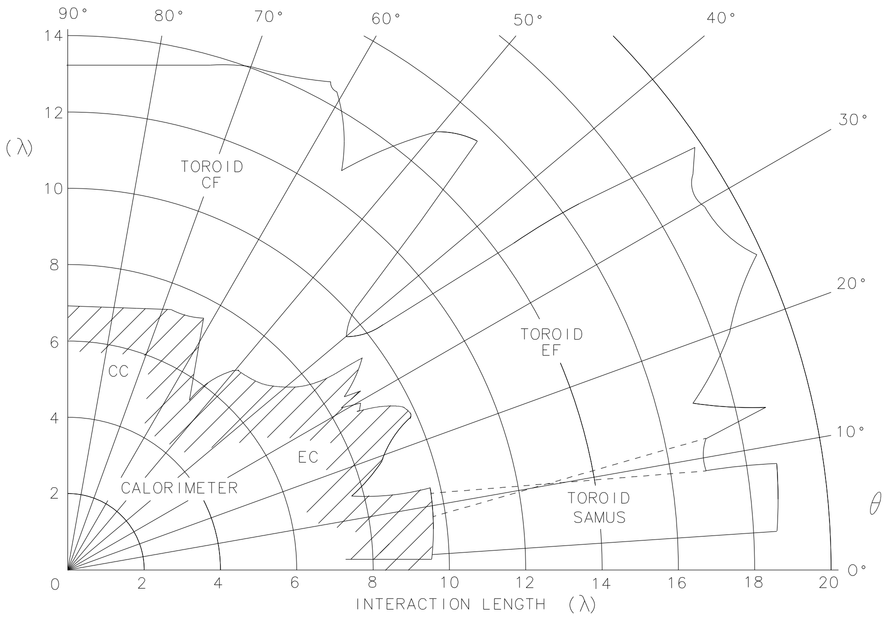

Figure 3.12: Depth of the detector in interaction lengths.

The muons are detected in an array of rectangular shaped, single wire drift tubes located outside the calorimeters. The design, shown in Figure 3.13, is one layer of chambers (the A-layer) inside an iron toroid magnet and two layers (B and C) outside the magnet. The trajectory of a charged particle curves as it passes through the magnet. The angle between the entering and exiting track indicates the momentum of the particle.

There are five magnets altogether. The central magnet (CF) covers the region $|\eta| < 1$. The two EF magnets extend to approximately $|\eta| < 2.5$. The CF and EF magnets together with the drift chambers in front of and behind them constitute the Wide Angle Muon System (WAMUS). The Small Angle Muon System (SAMUS), with toroids located inside the inner radius of the EF WAMUS toroids, reaches down to $|\eta| = 3.5$. This analysis does not involve forward muons so the

SAMUS system is not used. The B field in the magnets is 1.9 T, oriented around the beam line (so that tracks bend in the r-z plane). The drift tube wires run parallel to the B field direction for accurate measurement of the bend angle of tracks. An end view of a WAMUS layer is shown in Figure 3.14. The width of a tube is about 10 cm. Different tubes vary in length between 191 and 579 cm. The drift velocity in the WAMUS cells is 6.5 cm/μs for a maximum drift time in a cell is about 0.77 μs. The drift field is shaped by a cathode pad running along the inside front and back of the tube. The cathode pads are divided into two separate pieces with a diamond pattern as shown in Figure 3.15. The two pieces of the cathode are read out independently. The relative sizes of the two signals are used to determine the position of a hit along the wire, apart from ambiguity due to the periodic repetition of the cathode pattern. The ambiguity is resolved using a coarse estimate of the position based on the time difference between signals on each end of the anode. In test data, the distance resolution was 1.3 mm in the coordinate along a wire and 0.3 mm in the coordinate perpendicular to a wire. The resolution $\sigma_{1/p}$ of the inverse of the muon momentum has been parametrized based on a fit to the $\mu\mu$ mass distribution in Z and J/ψ data as $(\sigma_{1/p}/(1/p))^2 = (0.18(p-2))^2 + (0.008p)^2$, where the muon momentum is measured in units of GeV/c [30].

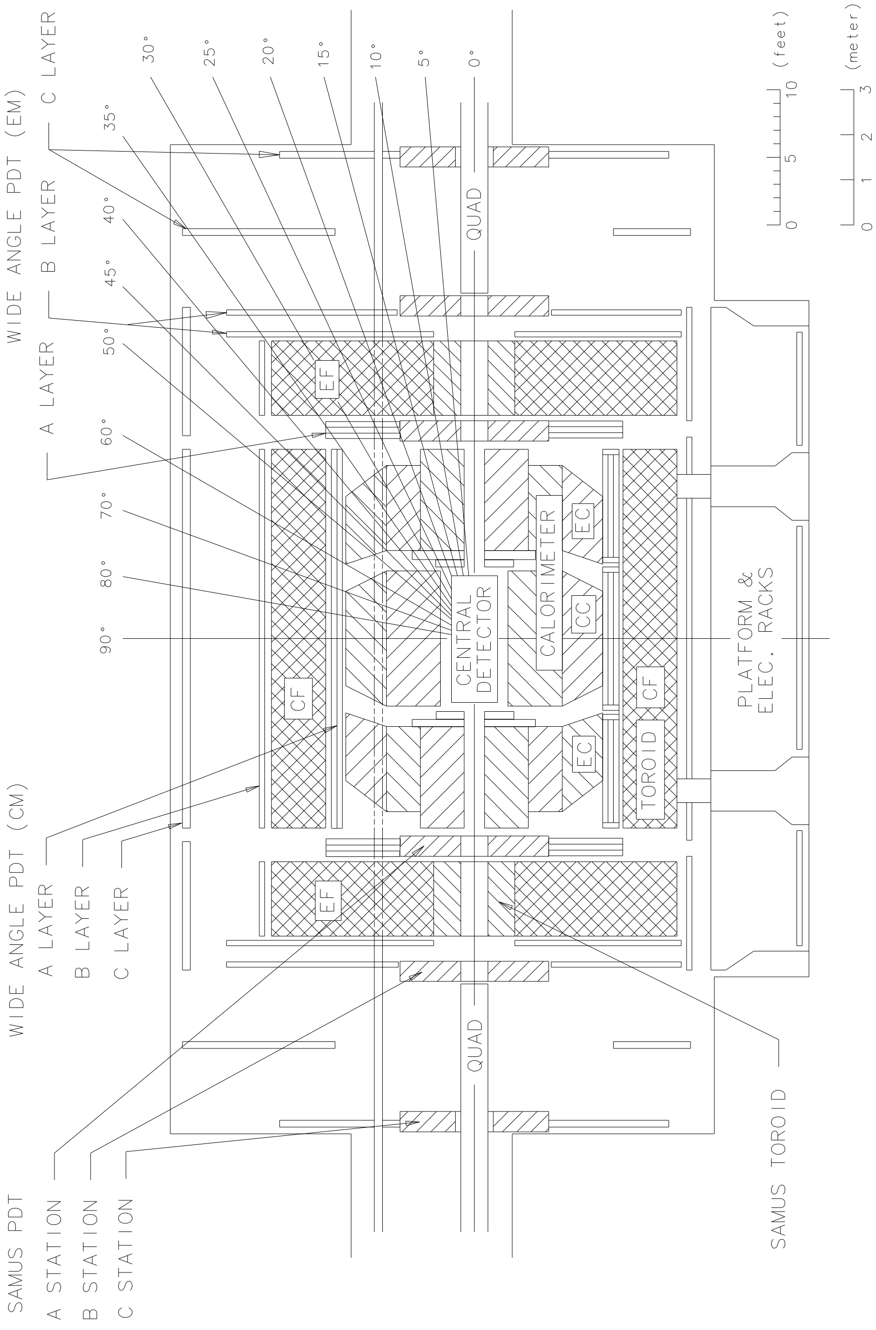

Figure 3.13: Muon Layers.

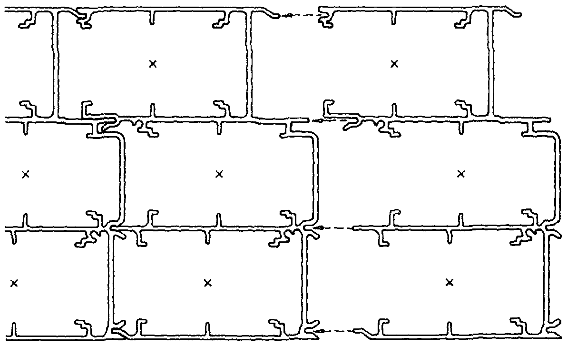

Figure 3.14: End view of a three plane WAMUS layer.

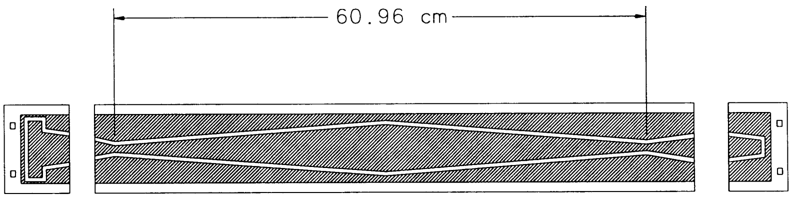

Figure 3.15: WAMUS cathode pad.

Chapter 4

Data Handling

4.1 Triggering

During the 1992-6 collider run, proton and antiproton bunches crossed at the interaction region approximately $286,000$ times per second. Over half of all the crossings produced at least one inelastic collision. Bandwidth and storage considerations limited the rate at which events could be saved to magnetic tape to an average of about two events per second. The decisions as to whether to keep events were made in several stages.

The first stage, called Level 0, required hits in the two arrays of scintillator at each end of the detector consistent with an inelastic interaction. The timing information from these hits was used to determine the z position of the interaction for use by the subsequent trigger stages. A fast estimate was provided to the next stage, Level 1, and a slower more precise calculation was available for the final stage, Level 2. Nominally, the resolution of the fast (slow) measurement is about 15 (3.5) cm [33]. The resolution deteriorated when there were multiple interactions, which occurred for over half of the events firing a high p_T trigger.

At Level 1, the calorimeter towers, with dimension 0.1×0.1 in $\eta \times \phi$, were grouped 2×2 into sets of trigger towers. Analog to digital readouts (along with the tower position) provided the transverse EM energy as well as the total transverse energy in each trigger tower to hardware based logic units which passed or rejected events depending on the number of EM and jet trigger towers above various E_T thresholds. The Level 1 decisions were made within the 3.5 μs between bunch crossings.

Some triggers made use of a Level 1.5 system which allowed for a calculation of EM tower energy and isolation using individual tower energies in a time slightly longer than one bunch spacing.

Events passing the Level 1 and Level 1.5 triggers were passed to Level 2. At Level 2 the full detector readout was available to software algorithms running on VAX computers which provided preliminary particle identification and a missing transverse energy calculation.

The triggers used to select data for this analysis and the minimum conditions required by them were the following:

`ele_1_mon` Level 1: one EM trigger tower with $E_T > 7$ GeV. Level 2: one electron candidate with $E_T > 16$ GeV. Prescaled.

`ele_jet` Level 1: one EM trigger tower with $E_T > 10$ GeV and one jet trigger tower with $E_T > 5$ GeV. Level 2: one electron candidate with $E_T > 15$, one 0.3 cone jet with $E_T > 10$, $\not\!\!E_T > 10$.

`ele_jet_high` Level 1: one EM trigger tower with $E_T > 12$ GeV and one jet trigger tower with $E_T > 5$ GeV. Level 2: one electron candidate with $E_T > 15$, one 0.3 cone jet with $E_T > 10$, $\not\!\!E_T > 14$.

`ele_high` Level 1: one EM trigger tower with $E_T > 10$ GeV. Level 2: one electron candidate with $E_T > 20$ GeV.

`em1_eistrkcc_ms` Level 1: one EM trigger tower with $E_T > 10$ GeV Level 1.5: one EM tower with $E_T > 15$ GeV. Level 2: one electron candidate with isolation isolation, associated hits in the CDC for clusters in the CC, $E_T > 20$ GeV.

`em1_eistrkcc_esc` Level 1: one EM trigger tower with $E_T > 10$ GeV. Level 1.5: one EM tower with $E_T > 15$ GeV. Level 2: two electron candidates—one with loose electron shape cuts, $E_T > 16$ GeV; one with standard shape cuts, isolation, associated hits in the CDC for clusters in the CC, $E_T > 20$ GeV.

`gis_dijet` Level 1: one EM trigger tower with $E_T > 10$ GeV Level 2: one isolated photon (same as electron) candidate with $E_T > 15$ GeV; two jets with $E_T >$ 15 GeV, $|\eta| < 2.0$.

`jet_multi` Level 1: three jet trigger towers with $E_T > 7$ and three large sized trigger towers (0.4×0.8) with $E_T > 15$ GeV and $|\eta| < 2.4$. Level 2: five 0.3 cone jets with $E_T > 10$ GeV and $|\eta| < 2.5$. For part of the run it was also required that the scalar sum of the energies of all Level 2 jets with $|\eta| < 2.0$ be greater than 115 GeV.

`jet_min` Level 1: one jet trigger tower with $E_T > 3$ GeV. Level 2: two 0.3 cone jets with $E_T > 20$ GeV. Prescaled.

`jet_3_mon` Level 1: Two jet trigger towers with $E_T > 5$ GeV. Level 2: Three 0.3 cone jets with $E_T > 10$ GeV. Prescaled.

`jet_4_mon` Level 1: Two jet trigger towers with $E_T > 5$ GeV. Level 2: Four 0.3 cone jets with $E_T > 10$ GeV. Prescaled.

The triggers `ele_jet` and `ele_high` were active while the first 13.5 pb^{-1} of data were taken. The other triggers were active for the remainder of the data. The triggers marked 'prescaled' accepted only a fraction of the events that satisfied their conditions, usually 5% or less, in order to control high acceptance rates.

4.2 Particle Identification

4.2.1 Electrons

Electrons were identified by the distinctive pattern of energy deposited in the calorimeter by electromagnetic showers and by the presence of a track leading from the interaction vertex to the cluster of hit calorimeter cells. Since there is no magnetic field in the inner tracking region the sign of tracks cannot be determined and no distinction is made between electrons and positrons. The energy scale for electrons was calibrated to the Z boson mass. Several quantities were used to distinguish electrons from other sources of EM energy clusters such as $\pi^0 \to \gamma\gamma$.

Electromagnetic energy clusters were formed by combining calorimeter towers using a nearest neighbor algorithm with EM tower seeds. The electromagnetic energy fraction f_{EM} of a cluster is the ratio of its energy found in EM calorimeter cells to its total energy. By definition all electron candidates satisfy $f_{\mathrm{EM}} > 0.9$.

Electron showers are compact and were mostly contained in the core of EM cells within a radius $R = \sqrt{\eta^2 + \phi^2}$ of 0.2 around the shower center. The isolation fraction $\mathcal{I}$ is defined as the ratio of energy in non core EM and FH cells within a cone of 0.4 around the center to the energy in the cluster core. This quantity tends to be substantially lower for electrons from the decay of W and Z bosons than for the backgrounds, most of which originated in hadronic jets and were usually accompanied by nearby energetic particles.

A covariance matrix was used to compute a variable χ^2_e representing the consistency of the cluster with the shape of an electron shower. The covariance matrix includes forty-one variables: the fractions of energy deposited in the first, second, and fourth layers of the EM calorimeter; the fractions of energy in each cell of the third EM layer lying in a six by six array around the tower containing the highest energy cell; the logarithm of the cluster energy; and the z position of the interaction vertex. The elements of the covariance matrix were determined using a `GEANT` model of the detector and were binned in the η location of the shower.

Calorimeter clusters were required to match a charged particle track in the CDC, FDC or VTX . The cluster-track match significance σ_{trk} is a measure of the distance between the cluster centroid and the intersection of the extrapolated track to the third EM calorimeter layer.

Photons which converted to e^+e^- pairs before the calorimeter sometimes produced pairs of tracks which matched a cluster well and were too close together to be resolved. These cases were identified by the amount of ionization along the track dE/dx; conversions typically deposited twice the charge expected from one minimum ionizing particle.

The transition radiation signal was quantified by summing the energies deposited along the track in the TRD. In order to suppress fluctuations, the layer with the highest energy was excluded from the sum. The TRD efficiency $\varepsilon_{\mathrm{TRD}}$ was defined as the cumulative distribution of the energy sum for real electrons, normalized to lie between zero and one, with low energies, as from pion backgrounds, corresponding to high values of $\varepsilon_{\mathrm{TRD}}$ [32].

The four variables f_{EM}, χ^2_e, σ_{trk} and dE/dx were combined into an approximate likelihood ratio L_4 for the hypotheses that a candidate electron is signal or background [31]. The likelihood function was constructed using distributions measured in inclusive W and Z data. These distributions are shown in Fig. 4.1. Also shown are the distributions for $\varepsilon_{\mathrm{TRD}}$ and L_5. L_5 a likelihood variable which includes $\varepsilon_{\mathrm{TRD}}$ in additions to the quantities used in L_4. The present analysis does

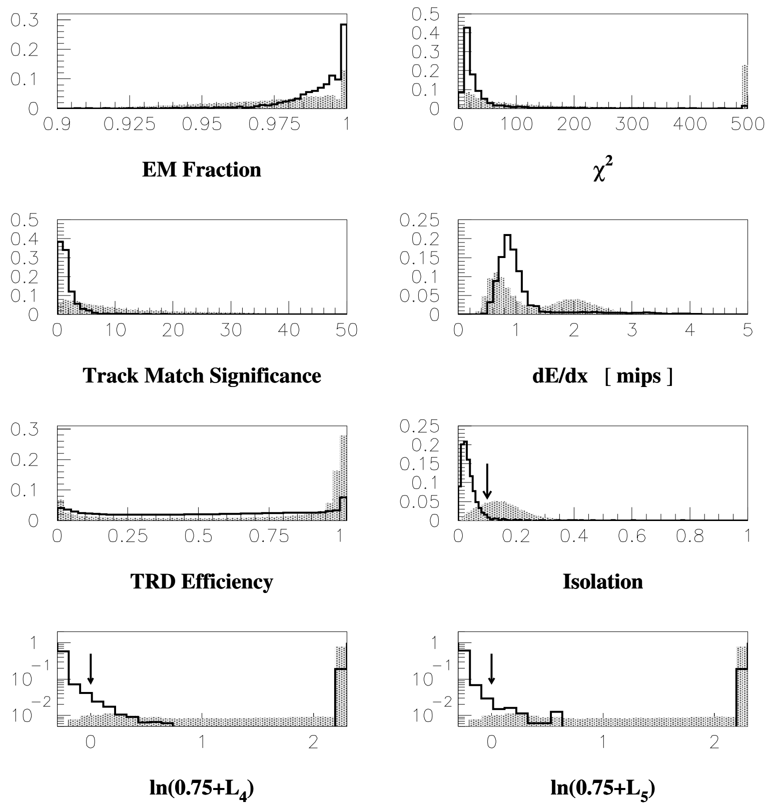

Figure 4.1: Quantities used in the electron likelihood test. The arrows indicate the position of the cut for tight electrons in the CC.

not make explicit use of L_5, however, the dilepton signatures ee and $e\mu$ (see Section 6.3) do and the values of $\varepsilon_{\rm TRD}$ for the $e+$jets (μ-tag) candidates are included in Appendix B.

Based on these quantities, two classes of electron candidates were defined. Objects satisfying $\mathcal{I}< 0.3$ and $\chi^2_e < 300$ are termed 'loose.' The loose sample was used in the estimation of background from false electrons. 'Tight' electron candidates are the subset of loose ones which passed the additional requirements $\mathcal{I}< 0.1$ and $L_4 < 0.25(0.3)$ for CC (EC) clusters. The calculation of the efficiency of the electron identification criteria is discussed in Appendix C.

4.2.2 Photons

'Loose' photon candidates were defined to be EM clusters with no associated track, $\chi^2_e < 100$ and $\mathcal{I} < 0.1$. For 'tight' photon candidates the χ^2_e threshold was lowered to 50 and the cluster was required to be away from cryostat edges, where the tracking coverage is not complete.

4.2.3 Muons

Muons were identified by connecting track segments found in the A, B and C layers of the muon system. [1] The momentum was determined by the bend angle of the combined track as it passed through the iron toroid magnet located between the A and B layers and was corrected for the expected amount of energy lost due to ionization in the calorimeter, typically about 2 GeV. The background from random hits due to noise was reduced by requiring good quality of the reconstructed track and a matching trace of energy through the calorimeter.

For the purpose of muon identification the run is divided into three periods. Muon identification for data taken during the first period, 1A [2], was as described in [4]. Beginning with the second period, 1B(a), the criteria were simplified by the availability of information about muon tracks in the calorimeter [34]. The muon drift chambers, particularly the ones around the EF toroid, suffered efficiency loss due to the accumulation of a substance on the anode wires in chambers exposed to high radiation doses from the Main Ring and Tevatron [35]. This substance originated from outgassing of the polyester-epoxy-glass material used in the construction of the cathode pads. Between 1B(a) and 1B(b) the anode wires were cleaned by zapping the wires with a high current [36]. As a result, only muons de-

[1] Tracks with only an A-layer segment were not allowed.

[2] See Table A.1 for the luminosity corresponding to the intervals 1A, 1B(a), 1B(b) and 1C.

tected in the CF system, approximately $|\eta| < 1$, were used prior to 1B(b). For data taken during the third period, 1B(b) and 1C, muons detected in the EF system (excluding ones with some hits in the SAMUS system) were used as well [37].

The quality of a muon track was measured by testing the following conditions [38].

- None of the layers have zero hits.
- The impact parameter with the vertex is less than 100 cm in the non bend view.
- The impact parameter with the vertex is less than 80 cm in the bend view.
- The rms residual of the hits used in the fit is less than 7 cm in the non bend view.
- The rms residual of the hits used in the fit is less than 1 cm in the bend view.

Muons candidates in the CF (EF) were allowed to fail at most one (zero) of these conditions.

The track from the muon system was used to define a path through the calorimeter to the position of the interaction vertex. A 5×5 wide road of calorimeter cells was defined along this path. Any of these cells with energy two standard deviations above noise level [3] was counted as a hit. The longest chain of contiguous hit cells constituted the calorimeter track. Muon candidates were required to have tracks with hits in at least 70% of the possible layers in the hadronic calorimeter. If the track did not have hits in all of the possible hadronic layers then it was also required that at least one of the nine central cells in the outermost layer of the 5×5 wide road be hit.

[3] To reduce the event size, cells for which the signal was within two standard deviations of zero were not read out.

4.2.4 Jets

The jets of particles resulting from hadronization of quarks and gluons were identified by applying a fixed cone clustering algorithm to calorimeter towers. The central steps in the algorithm are the following. Calorimeter towers with $E_T > 1$ GeV serve as seeds. After preliminary combinations are formed from neighboring seeds, a cone with a radius of 0.5 in $\eta \times \phi$ is drawn around the seed and the E_T weighted η and ϕ of the towers within the cone are calculated. These values define the axis of a new cone and the process is iterated until the position of the axis converges. The energy and momentum of a jet are given by

$$\begin{aligned} E &= \sum_i E_i \\ p_x &= \sum_i E_i \sin(\theta_i)\cos(\phi_i) \\ p_y &= \sum_i E_i \sin(\theta_i)\sin(\phi_i) \\ p_z &= \sum_i E_i \cos(\theta_i) \end{aligned} \tag{4.1}$$

where the sums are over each cell in the final cone, E_i is the energy in the ith cell, and θ_i and ϕ_i are the angles from the reconstructed vertex to center of the ith cell.

For jets with at least 15 GeV of transverse momentum in the calorimeter, the momenta of any good quality muons within the jet cone were included. The jet energy scale [67] was calibrated with respect to the electron and photon energy scale by enforcing transverse energy balance in $\gamma +$ jet events. Corrections were made for energy in the jet cone from uranium noise and the underlying event and for energy flow in and out of the cone due to the lateral size of hadronic showers in the calorimeter.

4.2.5 Missing Energy

Neutrinos escape the detector without interacting. The presence of a high energy neutrino, as from W boson decay, was inferred from the imbalance of momentum measured in the calorimeter and muon system. Even in a high energy interaction such as $t\bar{t}$ production, where the center of mass energy of the $t\bar{t}$ pair is typically almost 400 GeV [39], much of the 1800 GeV in the $p\overline{p}$ system remains and is carried away down the beampipe at very low angles by the p and $\overline{p}$ remnants. As a result, it is not possible to constrain the z component of momentum in an event. However, the low angle particles do not have a substantial component in the transverse direction. Thus the momentum measured in the detector should balance in the x and y directions unless some of it is carried away by a noninteracting particle. The missing energy in the x (y) direction $\not\!\!E_x$ ($\not\!\!E_y$) was defined to be minus the sum of the x (y) components of energy associated with each cell of the calorimeter, the corrections for jet and electron energies, and good quality muons. The missing transverse energy $\not\!\!E_T$ is given by $\sqrt{\not\!\!E_x^2 + \not\!\!E_y^2}$.

Chapter 5

The $e + \text{jets}$ (μ-tag) Signature

5.1 Cross Section Results

We have measured $\sigma_{t\bar{t}}$ by counting events which have the characteristics expected of $t\bar{t}$ decays. In this Chapter, we consider the decay modes that yield an isolated high p_T electron, $\not\!\!E_T$, and jets, including at least one jet containing a muon to indicate the decay of a b-flavored hadron. In the data sample of 108.3 ± 5.8 pb^{-1} there are five candidate events with this signature. The expected background is 1.06 ± 0.39. The cross section was calculated from the formula

$$\sigma_{t\bar{t}} = \frac{N - B}{\mathcal{L}\,\varepsilon} \tag{5.1}$$

where N is the number of candidates; B is the background; $\mathcal{L}$ is the integrated luminosity; and ε, the efficiency, is the fraction of $t\bar{t}$ events expected to satisfy the selection criteria. For an assumed top quark mass of 170 GeV/c^2, [1] ε is 0.00568 ± 0.00084, giving $\sigma_{t\bar{t}} = 6.4^{+4.5}_{-2.9}\,(\text{stat.}) \pm 1.2\,(\text{sys.})\,\text{pb}$.[2] The sources of uncertainty in the measurement are summarized in Table 5.1. The efficiency depends on m_t—for greater m_t, the decay products will be more energetic and will more frequently be above the various p_T thresholds in the event selection. The cross section as a

[1] DØ has measured $m_t = 172.0 \pm 7.5$ GeV/c^2 using kinematic fitting of lepton plus jets and dilepton events [15]. In this dissertation, results are always given for $m_t = 170$ GeV/c^2 unless

Statistics	$^{+70.3}_{-43.8}$ [%]
Efficiency	$\pm$ 14.8 [%]
Backgrounds	$\pm$ 9.9 [%]
Luminosity	$\pm$ 5.4 [%]

Table 5.1: Relative uncertainties in the $e+$jets (μ-tag) measurement of $\sigma_{t\bar{t}}$.

function of assumed top quark mass is shown in Figure 5.1. The measurement of the luminosity is discussed in Appendix A. The following sections describe how the other quantities in Equation 5.1 were determined.

5.2 Event Selection

The analysis of this signature uses events recorded with the trigger `ele_jet` during Run 1A or with the trigger `ele_jet_high` during Runs 1B and 1C. As discussed in Section 4.1, these triggers required three kinds of objects—an electron, $\not\!\!E_T$ and a jet—all with relatively low E_T thresholds. They were thus not efficient for inclusive W boson events but were designed to be efficient for events which would pass the full set of anticipated offline requirements for $t\bar{t}$ events while maintaining a manageable trigger rate. Events recorded during runs in which parts of the detector did not function properly, about 1% of the data, were removed. Furthermore, beam losses from the Main Ring during antiproton production sometimes hit parts of the detector near the Main Ring beam pipe—sections of the coarse hadronic calorimeter and muon system in particular. This occurred mostly when protons in the Main Ring underwent transition (see Section 3.1), about 0.3 s after injection,

otherwise specified; 170 GeV/c^2 is the closest value to the measured mass for which we have generated simulated $t\bar{t}$ events with which to study the efficiency.

[2]In this Chapter we quote an asymmetric statistical uncertainty on the cross section because there are only five candidate events. The upper (lower) error is the difference between $\sigma_\pm$ and the central value $\sigma_{t\bar{t}}$, where σ_+ and σ_- are defined by $\sigma_\pm \mp \sqrt{\sigma_\pm \mathcal{L}\varepsilon + B}/\mathcal{L}\varepsilon = \sigma_{t\bar{t}}$, i.e. $\sigma_\pm$ is the cross section for which a measured value of $\sigma_{t\bar{t}}$ would be a one standard deviation fluctuation downward (upward).

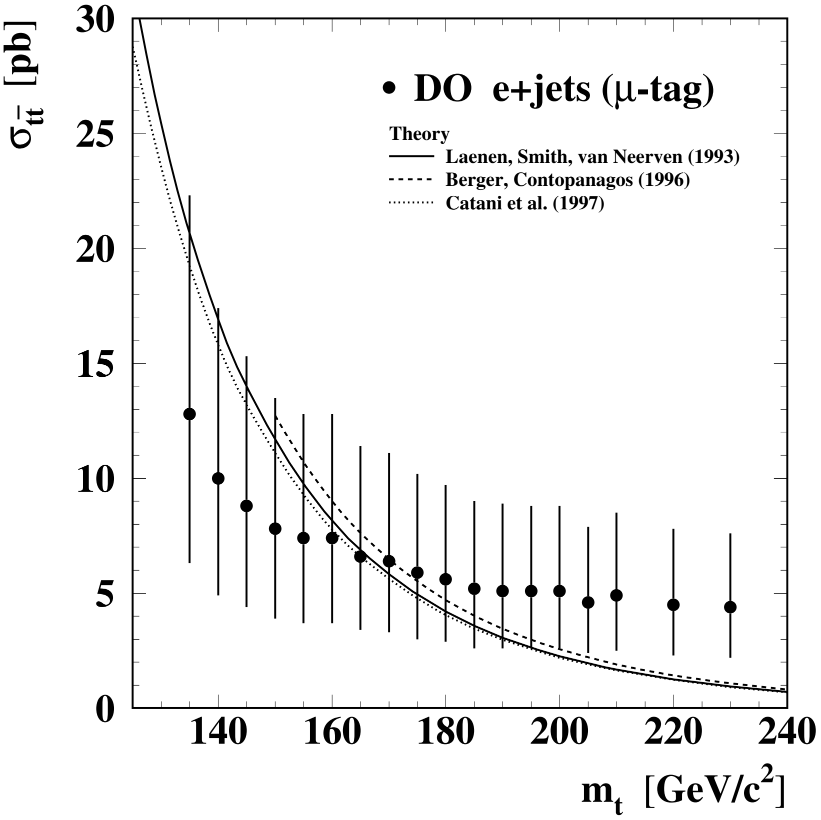

Figure 5.1: Cross section from the e+jets (μ-tag) signature. The error bars indicate the systematic and statistical uncertainties combined in quadrature. The deviation of the points from a smooth curve is due to the finite statistics of the Monte Carlo efficiency calculation. Also shown are the theoretical calculations from [23, 24, 25].

and when the bunch train itself passed through DØ, which took about 1.6 μs each revolution. Thus events which occurred during the 0.4 s interval beginning 0.1 s after injection were removed. This amounts to a 10% loss of data. Events which occurred while Main Ring bunches passed through DØ were also removed. This is an additional 5% loss. The value 108.3 pb^{-1} for the integrated luminosity applies after imposing the conditions described above.

At least one electron candidate per event must have satisfied $p_T > 20$ GeV/, $|\eta_{det}| \leq 20$, [3] and the tight electron definition from Section 4.2.1. The p_T threshold separates $t\bar{t}$ events from the bulk of the rapidly falling spectrum of high EM fraction jets which can mimic electrons. Figure 5.2 shows the p_T distributions of electrons for the expected signal, calculated by Monte Carlo (as described in Section 5.3), and the tail of the distribution for tight electrons in data taken with the trigger `ele_1_mon`. In the data there is a bump near 40 GeV from $W \to e\nu$, but most of the events have false electrons. Below 20 GeV the trigger is not fully efficient; the distribution would continue to rise steeply if it were. Both histograms are shown normalized to unit area. If they were normalized to equal luminosity, the signal height would be lower by a factor of more than three thousand. All of the decay products in $t\bar{t}$ events tend to be 'central,' but the distribution of jets from ordinary QCD processes is nearly flat in rapidity. Furthermore, it is more difficult to discriminate between true and false electrons in the forward region. The signal to background ratio thus worsens significantly at high η as seen in Figure 5.3.

A minimum $\not\!\!E_T$ of 20 GeV was required next. The distribution of $\not\!\!E_T$ for simulated $t\bar{t}$ data and real data is shown in Figure 5.4. The events with $\not\!\!E_T$ greater than 20 GeV are predominantly $W \to e\nu$ with some background from false electrons. In $W +$ jets events the sharp drop after 40 GeV is smeared out by the hadronic energy resolution.

On rare occasions noise or sampling fluctuations in calorimeter cells could inflate the energy of a jet substantially and lead to a significant amount of $\not\!\!E_T$. An offline noise suppression algorithm which identified anomalous isolated energy deposits was applied during event reconstruction. This corrected for most cases of

[3] η_{det} is the tower index of the highest energy cell in the third layer of the EM calorimeter, equal to 10 times the eta position of the tower center measured from $z = 0$. The cut is made on η_{det} rather than η because the efficiencies and background rejection depend on location in the detector.

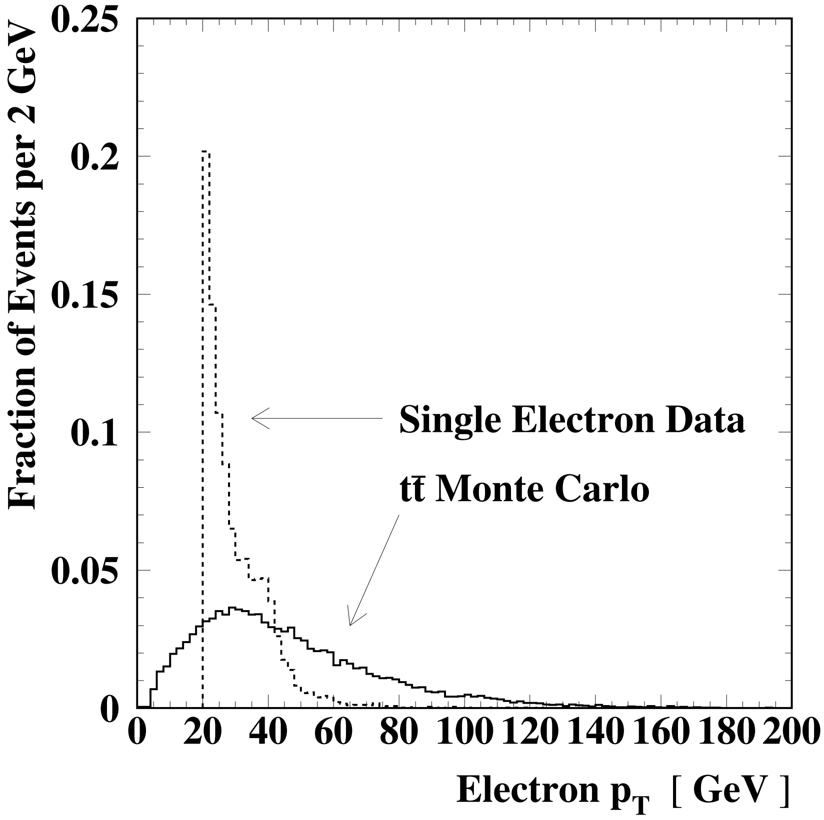

Figure 5.2: Electron p_T distributions for data (dashed) and simulated $t\bar{t}$ events (solid).

high voltage discharge. However, the CH layers of the calorimeter were also susceptible to large sampling fluctuations, leaving jets with a high fraction of energy in the outer layer. Figure 5.5 shows the distribution of CHF − EMF, where where CHF and EMF are the fractions of transverse energy in the CH and EM layers of the calorimeter, for three different classes of events: simulated $t\bar{t}$ events, $W+$jets candidates, and multijet events with a significant amount of measured $\not\!\!E_T$. Since ordinary multijet events normally have very little real $\not\!\!E_T$, selecting a sample with $\not\!\!E_T$ > 20 GeV has given us events with large fluctuations in the calorimeter energy measurements. This is reflected in the peak in the number of jets with CHF − EMF near one. This peak is significantly less pronounced in $W+$jets candidates with

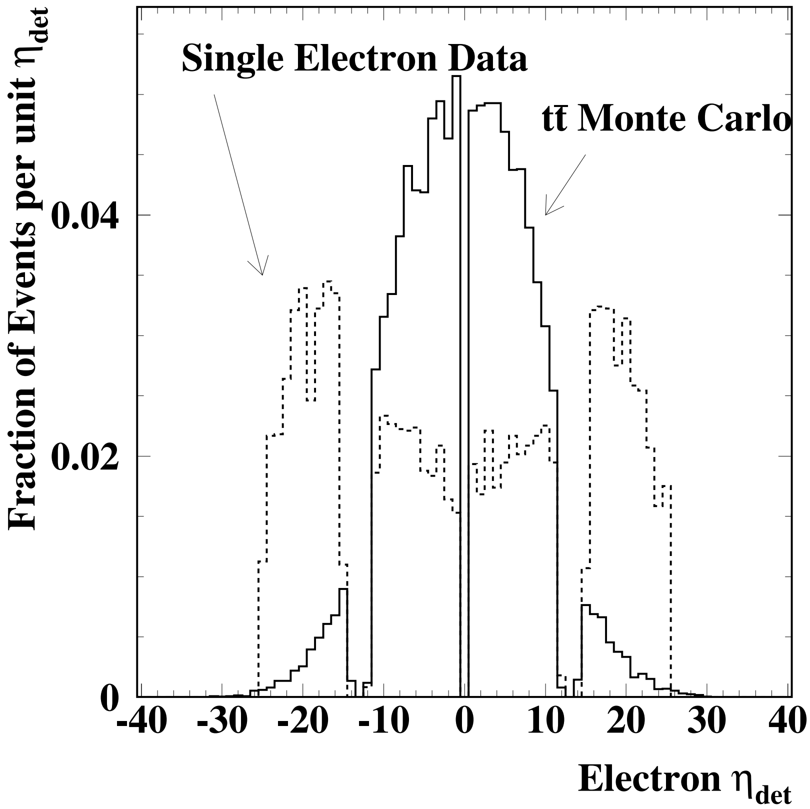

Figure 5.3: Electron η_{det} distributions for data (dashed) and simulated $t\bar{t}$ events (solid).

a tight electron because the multijet background is only about 20%, leaving most of the events without a bias toward mismeasured jets. In the simulated $t\bar{t}$ events, less than 1% of the jets have CHF $-$ EMF > 0.5 (this prediction of the simulation is confirmed in $Z \to ee$ data). As a result, we removed events containing a jet for which CHF $-$ EMF > 0.5.

Sometimes the offline noise suppression algorithm erred and mistook a cell within a compact, energetic jet for noise [40], sometimes resulting in an artificially large $\not\!\!E_T$. To guard against this, we required that the $\not\!\!E_T$ would not fall below 20 GeV if the energy of suppressed cells were restored for those cells which were in jets.

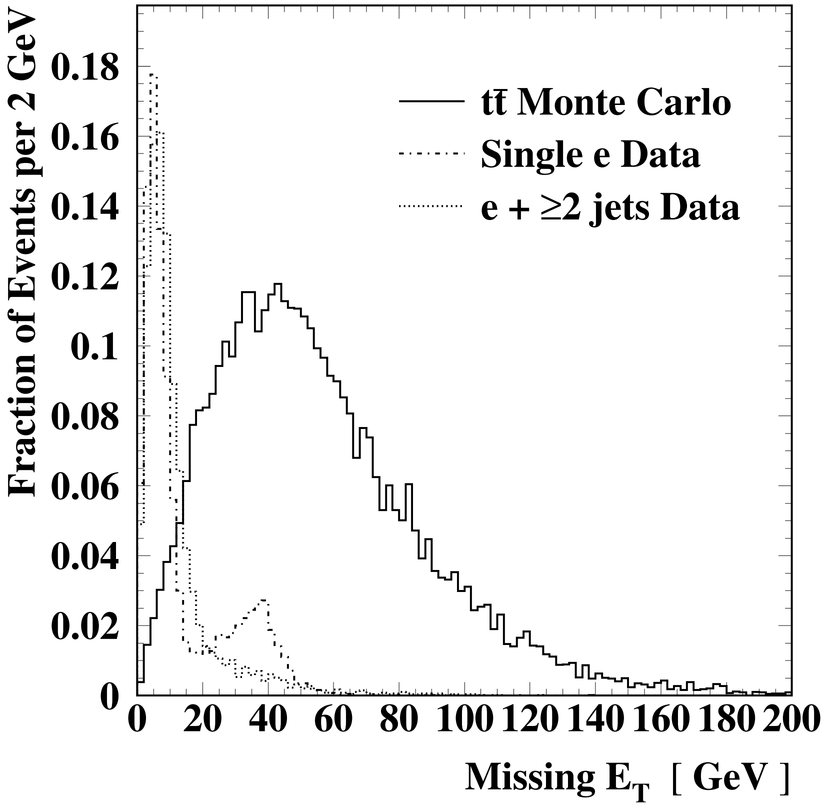

Figure 5.4: $\not\!\!E_T$ distributions for events containing a tight electron candidate. The solid histogram is simulated $t\bar{t}$ data; the dashed histogram is data taken with the trigger `ele_1_mon`; and the dot-dashed histogram is data taken with `gis_dijet` having two jets offline.

Having muons in an event tends to degrade the $\not\!\!E_T$ resolution. In multijet data, the distribution of the ϕ angle between a muon and the $\not\!\!E_T$, $\Delta\phi(\mu, \not\!\!E_T)$, peaks at 0 and 180 degrees, while for $t\bar{t}$ events it rises monotonically from 0 to 180 degrees, as in Figure 5.6. We therefore rejected events with $\not\!\!E_T < 35$ GeV if $\Delta\phi(\mu, \not\!\!E_T)$ was less than 25 degrees.

Events with more than one tight electron candidate were removed. This is designed to eliminate background from Z boson events. The invariant mass of the

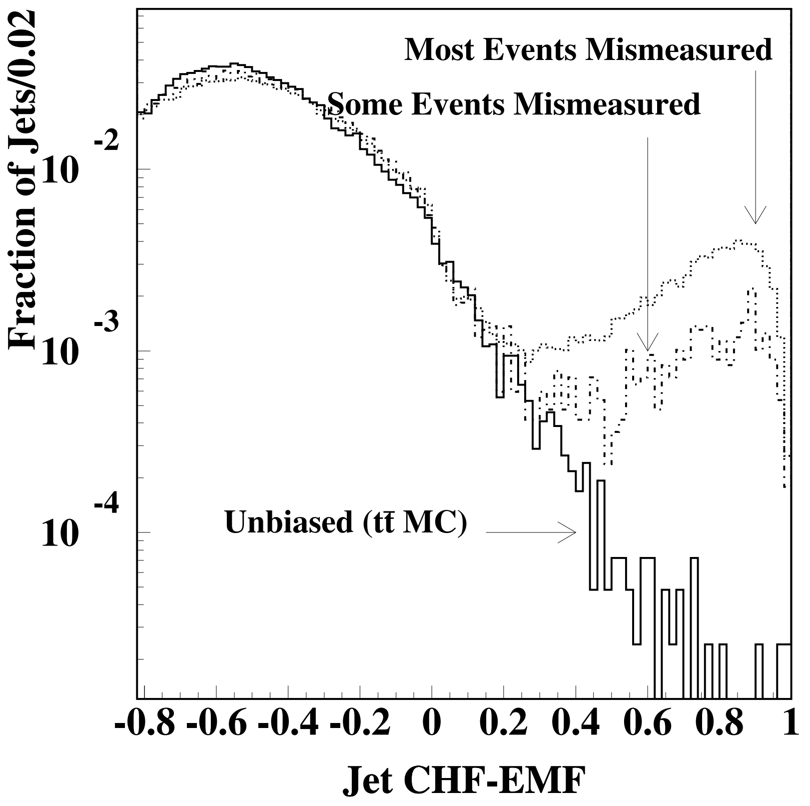

Figure 5.5: The difference between the coarse hadronic and electromagnetic E_T fractions in jets. The dotted (dot-dashed) histogram is data after the $\not\!\!E_T$ requirement without (with) the tight electron requirement. The solid histogram is simulated $t\bar{t}$ data. The histograms are normalized to unit area.

ee pair in the events that were removed is clustered at the Z mass, as seen in Figure 5.7.

Virtually every object found by the EM cluster algorithm was also found by the jet cone algorithm. For each jet associated with a tight electron we recalculated the energy of the jet, ignoring the energy of the cells which make up the EM cluster. If the recalculated jet E_T was still above 15 GeV then event was rejected, otherwise the jet was just removed from further consideration. Furthermore, if there was a not associated jet within $\Delta R < 0.5$ of a tight electron then the event

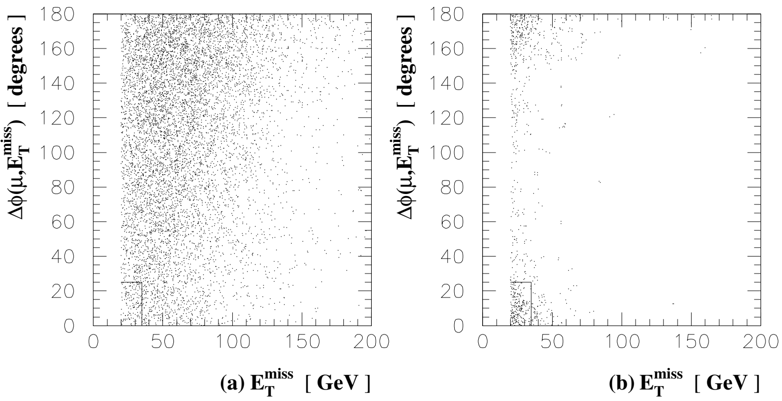

Figure 5.6: $\Delta\phi(\mu, \not\!\!E_T)$ vs. $\not\!\!E_T$ for (a) expected $t\bar{t}$ signal (b) data without the tight electron requirement.

was rejected. The purpose of these cuts is to remove the possibility of anomalous events with miscounted jets and to enforce an additional measure of isolation around the electron. They affect less than 0.5% of the data.

The jet multiplicity distribution for data and the expected signal is shown in Figure 5.8. At low jet multiplicities, the $t\bar{t}$ signal is overwhelmed by the $W+$jets background. Even at higher multiplicities the signal is well below the background level, but the situation has improved enough to be manageable with the help of further kinematic cuts and b-jet tagging. The requirement for $t\bar{t}$ candidates is three or more jets with $|\eta| < 2$ and (muon corrected) $p_T > 20$ GeV/c. Figures 5.9 and 5.10 show the jet p_T and η distributions respectively for both data and the expected signal. Almost all of the jets in $t\bar{t}$ events are within $|\eta| < 2$. The cut at $p_T = 20$ GeV on the third highest p_T jet gives good separation between signal and background.

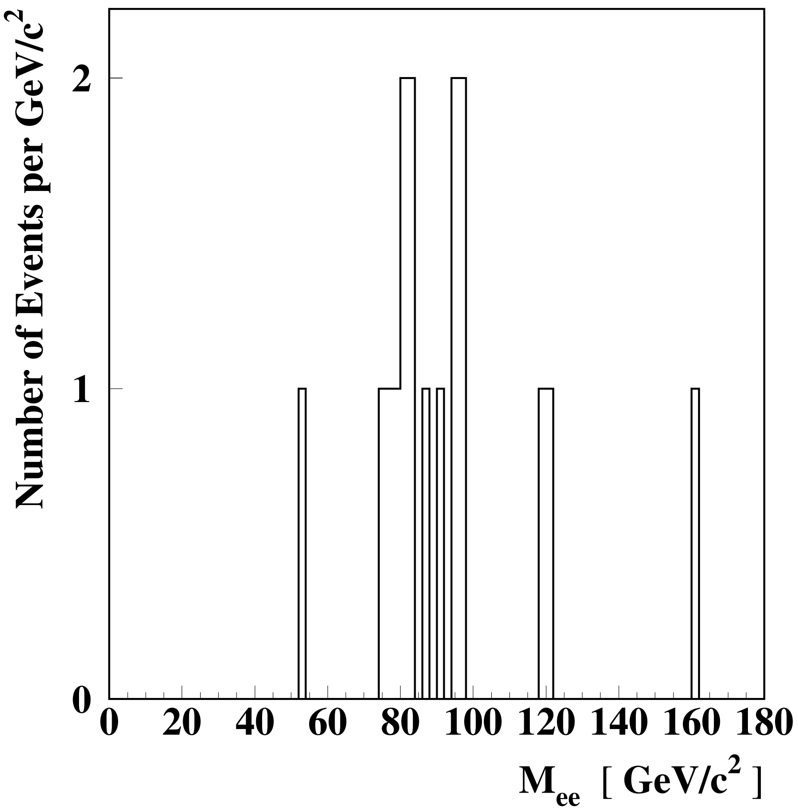

Figure 5.7: The electron–electron invariant mass of W candidates with two tight electrons.

The quantity H_T [41] is defined as the scalar sum of the transverse momenta of all jets satisfying $|\eta| < 2$ and $p_T > 15$ GeV/c^2. We required $H_T > 110$ GeV/c. The distributions for data and the expected signal are shown in Figure 5.11.

The aplanarity [42] $\mathcal{A}$ of an event is defined to be 3/2 times the smallest eigenvalue of the momentum tensor $M_{ij} = \sum_n p_i^n p_j^n / \sum_n (p^n)^2$, where p_i^n is the ith three-momentum component of the nth object in the event, and p^n is its momentum magnitude. The objects which enter in the sum are jets with $|\eta| < 2$ and $p_T > 15$ GeV/c, plus the leptonically decaying W boson. The momentum of the W boson was estimated by combining the three components of the electron momentum and the two components of the missing transverse energy with the con-

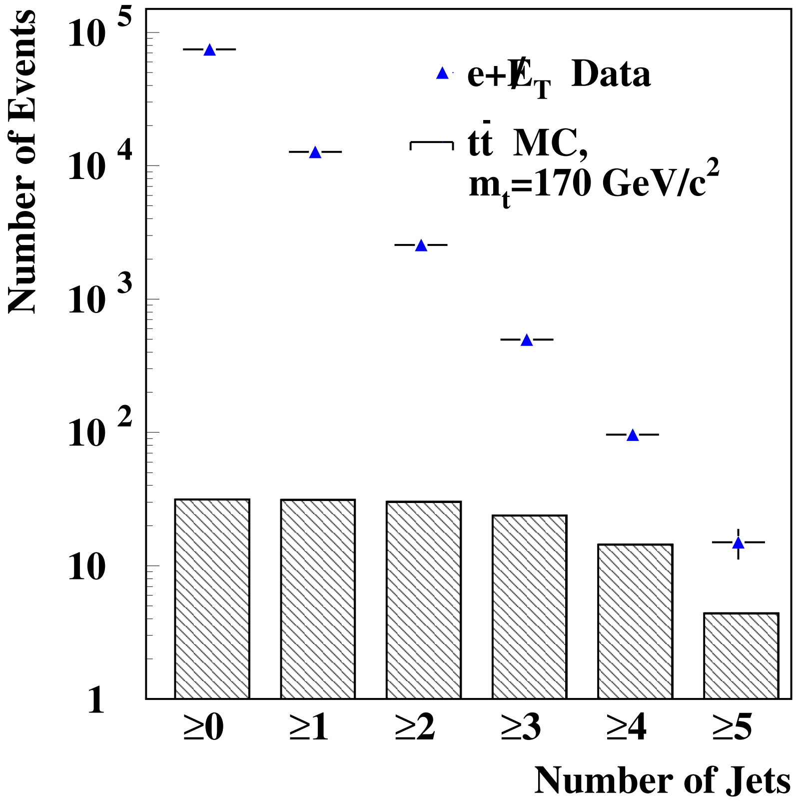

Figure 5.8: The jet multiplicity distribution for $W +$ jets data (solid histogram) and $t\bar{t}$ Monte Carlo (dashed histogram). The Monte Carlo does not include trigger inefficiency.

straint that the mass of the electron–missing energy system be 80 GeV/c^2. There are normally two solutions for the longitudinal momentum of the W; the smallest was used—this is the correct choice for $\sim 70\%$ of $t\bar{t}$ events at the Tevatron energy. If the transverse mass of the electron and missing energy is greater than 80 GeV there is no real solution. In this case the combined mass was constrained to equal the transverse mass.

$\mathcal{A}$ takes a value in the range 0 to 1/2. Events with objects having equal magnitude momenta and isotropic angular distribution have the highest value of $\mathcal{A}$ and are said to be spherical. $t\bar{t}$ events are generally more spherical than $W +$ jets

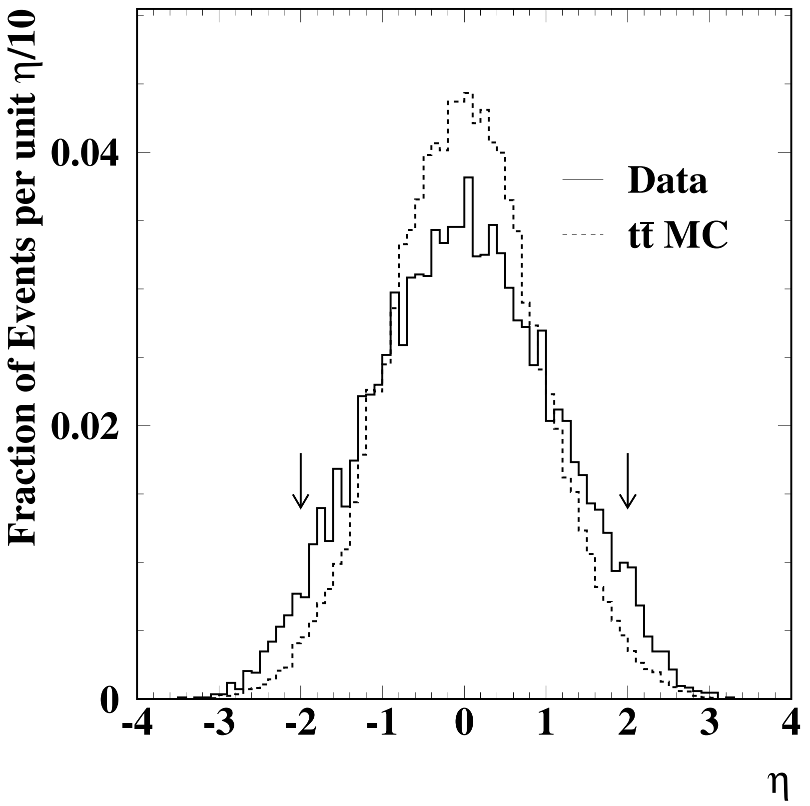

Figure 5.9: η of jets with $p_T > 20$ GeV. The solid histogram is data and the dashed histogram is the expected signal. Both are normalized to unit area.

events. In the latter case, the jets tend to be forward because of the t-channel matrix element, and they tend to be planar because of color connection effects. The distributions for data and the expected signal are shown in Figure 5.12.

Jets containing a muon candidate within a radius of 0.5 in $\eta \times \phi$ were considered to be tagged as b-quark jets if they satisfied $|\eta| < 2$, $p_T > 15$ GeV/c before correcting for muon momentum and $p_T > 20$ GeV/c after correcting for muon momentum. The conditions for muon candidates were that they have $p_T > 4$ GeV and satisfy the good quality requirements from Section 4.2.3.

The numbers of events remaining after each stage of selection are listed in Table 5.2. After all cuts, five events remain. The kinematic properties of these

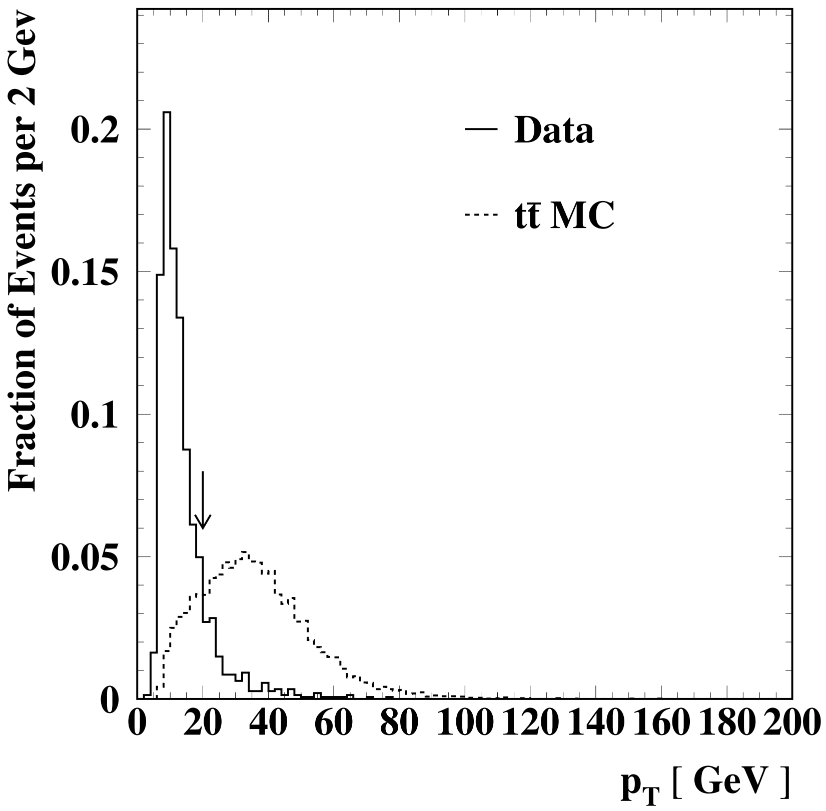

Figure 5.10: p_T of the jet with the third highest p_T and $|\eta| < 2$. The solid histogram is data and the dashed histogram is the expected signal. Both are normalized to unit area.

events are given in Appendix B. One of the candidates appears to be a dielectron event in which the track associated with the second electron was not reconstructed because it is not fully contained within the CDC. The presence of such an event is not surprising since about 17% of the $t\bar{t}$ events which satisfy the selection requirements are predicted to be from decay modes other than $e\nu_e qq'$. Contributions are expected from $e\nu_e\tau\nu_\tau$ (5%); $e\nu_e e\nu_e$ or $e\nu_e\mu\nu_\mu$ (6%); and $\tau\nu_\tau qq'$, $\tau\nu_\tau\tau\nu_\tau$, or $\tau\nu_\tau\mu\nu_\mu$ (6%).

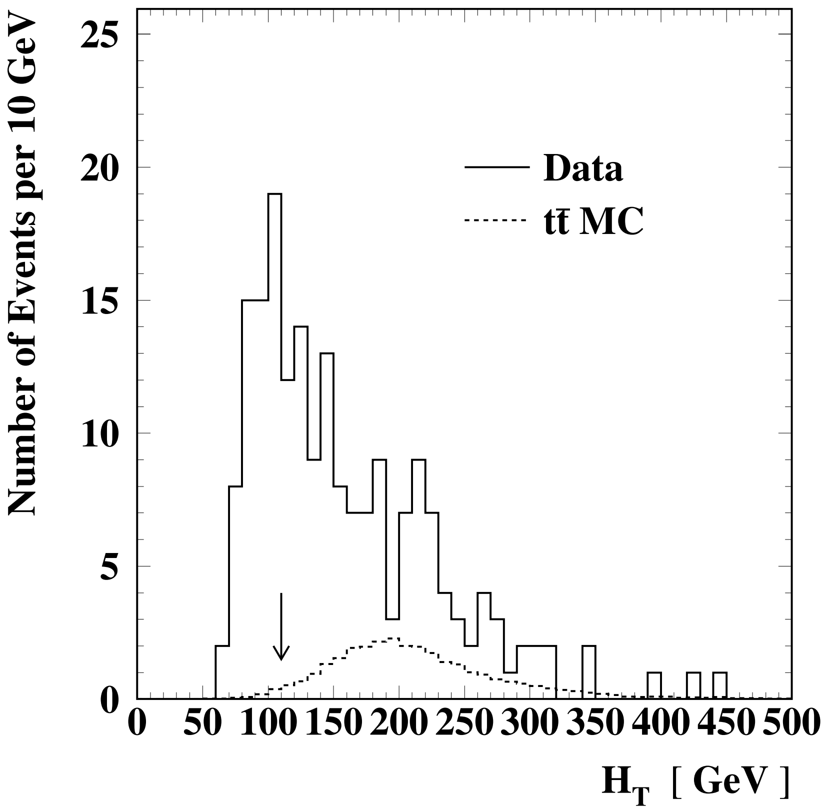

Figure 5.11: H_T

5.3 Efficiencies

The fraction of $t\bar{t}$ events expected to satisfy the selection criteria was calculated by Monte Carlo using simulated samples of $t\bar{t}$ pairs produced with `HERWIG 5.7` [43] and a model of the DØ detector based on `GEANT 3.14` [44]. The detector simulation writes output in the same format as raw data from the real detector. The simulated events were reconstructed and the reconstructed events were selected according to the same criteria as real events (with a view variations discussed below).

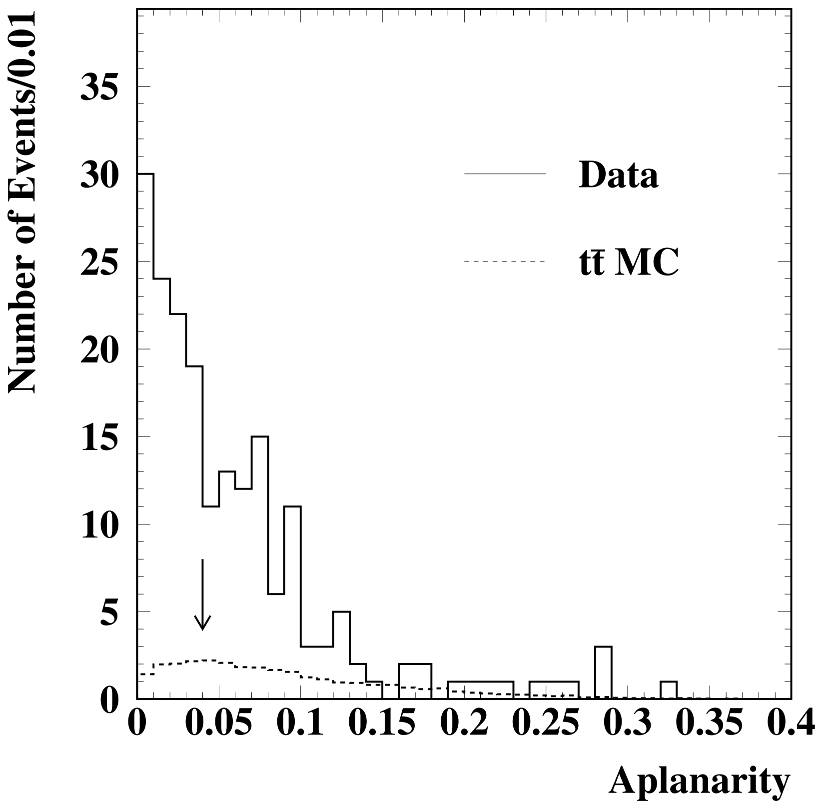

Figure 5.12: $\mathcal{A}$

5.3.1 Event Generation

`HERWIG` is a package of FORTRAN routines for computer simulation of high energy physics interactions. It produces hard scatter processes, such as $q\overline{q} \to t\overline{t}$ and $gg \to t\overline{t}$, according to the leading order cross section, adds initial and final state parton showers, decays heavy particles, groups colored partons into hadrons, and includes a model of the p and $\overline{p}$ remnants. The events for the present analysis were produced with the CTEQ3M parton distribution functions. The hadronization and heavy particle decays are modeled relatively simply compared to the parton showering. After the perturbative showering phase, gluons are split into $q\overline{q}$ pairs.

Cut	No. of Events
electron & $\not{E}_T$	84350
trigger	11972
bad runs	11864
micro blank	11284
MRBS	9219
CHF − EMF	8940
$\not{E}_T$ with suppressed cells	8858
$\Delta\phi(\mu, \not{E}_T)$	8852
no 2nd electron	8835
$\Delta R(e, j)$	8798
$\geq$ 1 jet	6350
$\geq$ 2 jets	1164
$\geq$ 3 jets	192
H_T	133
$\mathcal{A}$	67
μ-tag	5

Table 5.2: The number of events passing various stages of selection.

Quarks and antiquarks are then grouped into color neutral clusters which decay into hadrons according to phase space, spin and the flavor of the cluster.

The largest sources of uncertainty in the efficiency calculation come from the Monte Carlo generator. To estimate the uncertainty due to the modeling of the kinematic properties of $t\bar{t}$ events, the acceptance after all selection requirements except for the μ-tag requirement was calculated using the `ISAJET` [45] generator and the results compared to those obtained using `HERWIG`. The difference is about 7% for an assumed top quark mass of 170 GeV/c^2. The dependence as a function of m_t is shown in Figure 5.13. The aspect of the generator to which the kinematic acceptance is most sensitive is the parton showering. `HERWIG` has been shown to reproduce jet properties well at both the Tevatron [52] and LEP [53]. Reference [52] studied the topological properties (spectra of angles and energy distribution among jets) in inclusive three and four jet events and found that '[a]part from the $\cos(\theta^*)$ distributions, the `HERWIG` event generator provides a reasonably good description

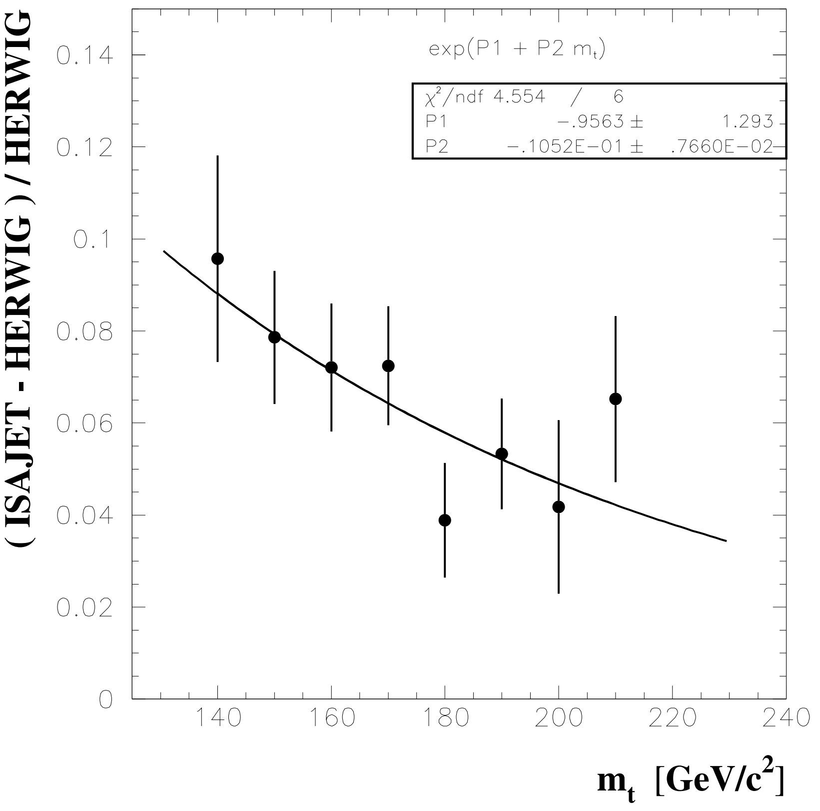

Figure 5.13: Uncertainty in acceptance for $t\bar{t}$ events due to the Monte Carlo generator modeling of kinematics.

of the data while the differences between the data and the predictions of [the] `ISAJET` and `PYTHIA` event generators are large in many distributions.' Thus the differences between the `HERWIG` and `ISAJET` efficiency calculations are not expected to seriously underestimate the difference between the `HERWIG` prediction and the actual efficiency.

In `HERWIG 5.7` all b-flavored hadrons decay by a spectator model with a branching fraction to muons $\mathrm{B}(b \to \mu) = 0.11$. This branching fraction is consistent with the rate measured at LEP for b-quark jets from Z boson decay $\mathrm{B}(b \to l + X) = 0.1113 \pm 0.0029$ and $\mathrm{B}(b \to \mu + X) = 0.107 \pm 0.007$ [19]. Using the CLEO Monte Carlo `QQ` [54] to decay b hadrons in place of the default `HERWIG` model reduces the tagging efficiency by a factor of 0.874. Differences between the two models include the p_T spectrum of the muons and the semileptonic branching fractions of charm mesons. However, the event simulation does not include π and K decays, which are believed to account for $\sim 30\%$ of muons with $p_T > 4$ GeV in jets from ordinary QCD production [4] [30]. As discussed in Section 5.4.2.4, we would expect an average of 0.034 muon tags per event from $t\bar{t}$ events in the candidate sample if the flavor composition of the jets were the same as in ordinary multijet events. Thus π and K decays may be expected to contribute an additional 1% to the tagging efficiency, partially compensating for the reduction suggested by the `QQ` model. For the cross section calculation, the efficiency result from the default `HERWIG` model was used and an uncertainty of 10% was assigned for the probability of a jet to contain a detectable muon.

5.3.2 Detector Simulation

`GEANT` is a system for describing the geometry and material content of a detector, propagating particles through the geometry and modeling their interactions in the material. The time required by the program to follow all the final state particles from a `HERWIG` $t\bar{t}$ event through the detector and generate showers in the calorimeters for the photons, electrons and hadrons, about half an hour per event on a VAX Model 9000, is too long for the size data samples needed. Instead DØ has created a large library of reusable electromagnetic and hadronic showers in the calorimeter [46]. There are about 1.2 million particles in the library, binned in the z position of the vertex, calorimeter tower index, momentum, ϕ distance from a module boundary, and particle type (hadrons and electrons/photons). Rather than generating a new shower for every particle in an event, the detector simulation selects a shower from the library in the appropriate bin and scales the energy deposited in calorimeter cells by the ratio of the event particle's energy to the library particle's energy. This procedure introduces a slight smearing of the spatial location of particles but the effect is not large compared to the scale of jets and, for electrons, is reduced further by choosing the library particle with the best spatial match. The simulation also saves time by only propagating electrons and muons through the tracking chambers. These strategies improve the speed of the simulation by a factor of about 120.

Despite the detail of the `GEANT` model, it is an idealization of the actual detector. This is most significant for the central tracking, calorimeter energy scales, and particularly the muon system, which is subject to various sources of inefficiency and resolution loss, such as chamber aging and misalignment, that are not incorporated into the simulation.

Since tracking information was only created for electrons, and since the all tracks found in the CDC are used to measure to vertex location, the reconstruction program used the generated vertex. In real data the resolution of the z position of the vertex is $\simeq 1.5$ cm and can be much worse if there are multiple vertices within about 10 cm of each other. This degraded the p_T resolution of objects in the event. The main effect for this analysis, however, is the possibility that electrons were lost in events with multiple interactions when the wrong vertex was identified as the principle one because the reconstruction program normally only looked for tracks in a road between an EM calorimeter cluster and the principle vertex. This resulted in a loss of about 9% of the electrons in inclusive W and Z events (see Appendix C). Fortunately, the loss appears to be only a few percent for events with multiple jets such as $t\bar{t}$ or $W+$jets, where the high particle multiplicity makes it unlikely that a typical inelastic interaction would produce more tracks [47].

The hadronic energy scale for jets is believed to be accurate to within $\pm(4\% + 1\,\mathrm{GeV})$ after standard corrections. This has been determined by comparing the

p_T balance in $Z +$ jets events between data and Monte Carlo [55]. Raising and lowering the energy of jets by this amount and correcting the $\not\!\!E_T$ accordingly, the acceptance for $t\bar{t}$ events varied approximately 5% for an assumed top quark mass of 170 GeV/c^2. The dependence as a function of m_t is shown in Figure 5.14.

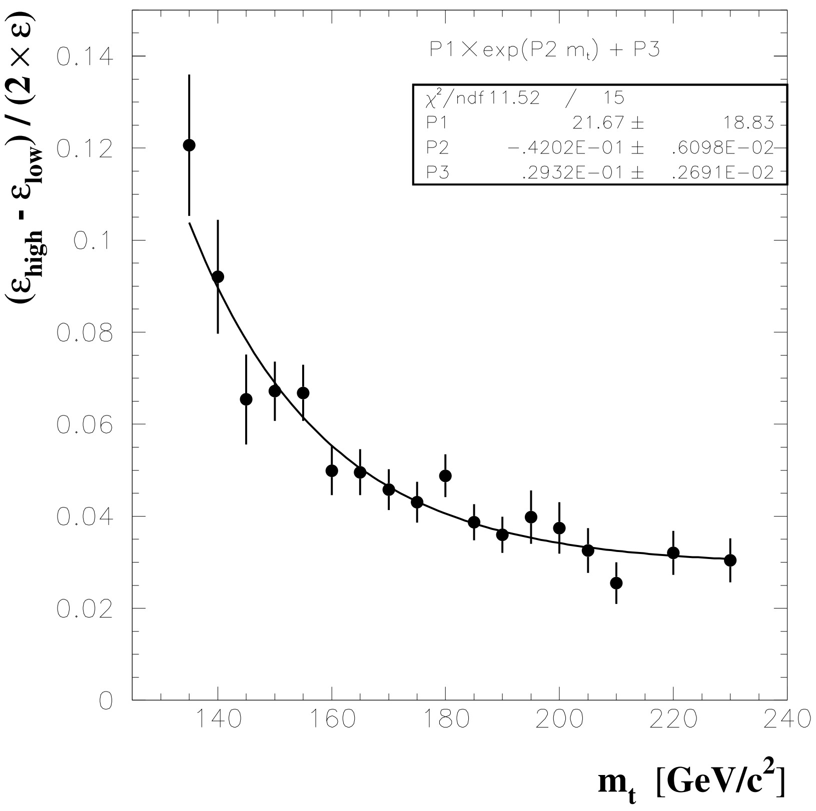

Figure 5.14: Uncertainty in acceptance for $t\bar{t}$ events due to the jet energy scale.

For Monte Carlo data, any EM cluster with an associated track satisfying the p_T, η_{det} and isolation requirements was called a tight electron. The events were weighted to account for the differences between the electron finding efficiencies predicted by the Monte Carlo and those observed in the data (see Appendix C). The electron finding efficiencies are given in Table C.1. The ith electron in a Monte Carlo event was thus assigned a weight w_i^e of 0.713 or 0.495 depending upon whether the electron was in the CC or EC. Each Monte Carlo event was assigned a weight $\sum_i w_i^e \prod_{j\neq i}(1-w_j^e)$, where the sum and product are over all of the 'tight' electron candidates in the event. This weight represents the probability that exactly one electron in the event would pass the tight electron quality requirements.

The differences between the real and simulated muon system were treated at two stages, partly before reconstructing the simulated data and partly after. Before reconstruction, a set of adjustments, collectively termed `MUSMEAR`, were made to the simulated raw muon data to replicate the timing resolution, hit finding efficiency and alignment errors measured for the actual detector [48]. The `MUSMEAR` adjustments reduce the muon efficiency by a factor of about 0.91. Because they do not include all of the factors which affect the efficiency of the actual detector, weights were applied for muon finding as well as electron finding. A loss of a factor 0.941 ± 0.032 (0.911 ± 0.061) in the CF (EF) region has been attributed to effects such as correlated hit losses and non-gaussian tails in the timing resolution [49] based on an extensive program of event scanning [50]. Additionally, a comparison of the ϕ distribution of muons before and after the chamber cleaning shows that before cleaning there was a hole in the acceptance at the location of the Main Ring which reduced the total efficiency by an average factor of 0.95 ± 0.02 for the first 13.9 pb^{-1} of data and 0.90 ± 0.02 for the following 50.9 pb^{-1} [51]. The combined muon weights are summarized in Table 5.3. We are interested in events with at

Run Range	Toroid	Weight
1C	CF	0.941
1C	EF	0.911
1B post-zap	CF	0.941
1B post-zap	EF	0.911
1B pre-zap	CF	0.847
1A	CF	0.894

Table 5.3: Efficiency weights for tag-muons. The uncertainty in the muon weights is 3.5% (6.7%) in the CF (EF).

least one good muon so the weight assigned to an event for muon efficiency was $1 - \prod_i (1 - w_i^\mu)$ where w_i^μ is the weight of the ith muon candidate and the product is over all good muons found in the event. The total weight for an event was the product of the electron and muon weights. The efficiency is then the sum of the weights for each simulated event that passed the event selection divided by the total number of simulated events.

5.3.3 Trigger

For simulated data the trigger efficiency is better than 99% for events passing the offline selection. The efficiency of the `ele_jet_high` trigger requirements—jet, $\not{E}_T$ and electron—have been checked in data and on the basis of these checks a combined uncertainty of 5% was assigned.

The jet requirement was checked against data that was taken with the trigger `em1_eistrkcc_ms`, which had no jet requirement and had $\not{E}_T$ and electron requirements which are more strict than those of `ele_jet_high`. The fraction of W candidates from `em1_eistrkcc_ms` that also passed `ele_jet_high` is plotted in Figure 5.15 as a function of the offline jet requirement. To preserve statistics, a muon tag was not required, but the p_T threshold for the last jet was lowered to 15 GeV, corresponding to the cut on the calorimeter energy for tagged jets. There are 50 events from `em1_eistrkcc_ms` satisfying ≥ 2 jets with $p_T > 20$ GeV, at least one additional jet with $p_T > 15$ GeV, and the H_T and $\mathcal{A}$ requirements. All 50 pass `ele_jet_high`. We conclude that the jet requirement in the trigger is better than 98% efficient at the one sigma level for $W +$jets events with some (20%) multijet background. This is a conservative estimate for $t\bar{t}$ events which on average have more jet energy than multijet or $W +$jets events.

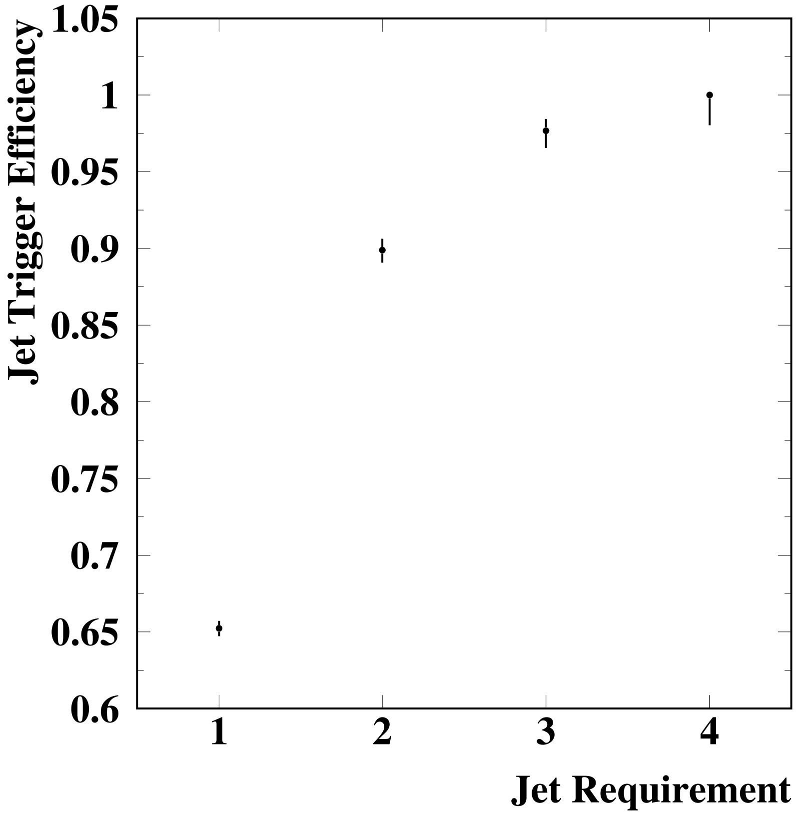

Figure 5.15: Efficiency of the trigger jet requirement. Counted in the first bin are events with ≥ 1 jet with $p_T > 15$ GeV; in the second (third) bin are events with ≥ 1 (2) jets with $p_T > 20$ GeV plus at least one additional jet with $p_T > 15$ GeV; in the last bin are events from the third bin which also pass the H_T and $\mathcal{A}$ requirements.

The $\not\!\!E_T$ requirement was checked against data taken with the `gis_dijet` trigger, which had more strict electron and jet requirements than `ele_jet_high` but did not require $\not\!\!E_T$. There are 40 events from `gis_dijet` satisfying ≥ 2 jets with $p_T > 20$, at least one additional jet with $p_T > 15$ GeV, and the H_T and $\mathcal{A}$ requirements. Two of these fail `ele_jet_high`. The multijet events in the sample have $\not\!\!E_T$ much closer to the threshold than either $t\bar{t}$ or $W +$jets events. With the multijet background subtracted, there are 30.96 (30.12) events before (after) ele_jet_high, giving an efficiency of $1.026 \pm 0.032 \pm 0.05$ where the first error is statistical and the second is from the background subtraction.

The electron requirement was tested using $Z \to ee$ events as in Appendix C, but in this case with data from the trigger ele_1_mon, which required only one electron candidate. The efficiency of the ele_jet_high requirements was found to be 0.98 ± 0.02 (1.05 ± 0.05) in the CC (EC).[4] Determining whether an electron found offline would have satisfied the trigger requirements involves matching offline and online objects after the fact. The matching algorithm itself has about a 1% inefficiency, also the p_T spectrum of electrons from Z boson decay is closer to the threshold than for $t\bar{t}$ events, so these are conservative estimates.

5.3.4 Results

The results for a range of top quark masses from 135 to 230 GeV/c^2 are summarized in Table 5.4. About 25% of $t\bar{t}$ events contain an electron from $W \to e$ or $W \to \tau \to e$, of which 75% have an electron with $p_T > 20$ GeV. Some of these electrons pass through gaps between cells or between the CC and EC cryostats but almost 16% of $t\bar{t}$ events contain an electron reconstructed as an EM cluster with $p_T > 20$ GeV and $\eta_{det} \leq 20$. Over 13% of these have a track associated with the primary interaction vertex and over 11% also pass the isolation requirement. This is reduced to under 9% after the electron likelihood requirement. The efficiency after each subsequent stage of selection is shown in Table 5.5 for a top quark mass of 170 GeV/c^2. Up until to the μ-tag requirement the major efficiency losses are from the demands for $\not\!\!E_T$, $\mathcal{A}$, and three jets—the last of which removes most of the dilepton decays. The standard HERWIG b-quark decay model puts at least one muon, not from W or τ decay, in 43% of $t\bar{t}$ events which pass the kinematic selection. In 26% there

[4] The errors are statistical only.

		Sources of Uncertainty						
m_t [GeV/c^2]	ϵ (%)	Kin.	μ-tag	Stat.	Trig.	e Id.	μ Id.	E. Scale
135	.286 ± .058	.029	.029	.019	.014	.011	.011	.030
140	.364 ± .069	.034	.036	.022	.018	.014	.014	.033
145	.413 ± .074	.036	.041	.023	.021	.016	.016	.032
150	.469 ± .078	.037	.047	.017	.023	.019	.018	.032
155	.494 ± .080	.037	.049	.017	.025	.020	.019	.030
160	.491 ± .077	.034	.049	.017	.025	.020	.019	.027
165	.555 ± .085	.035	.056	.018	.028	.022	.021	.028
170	.568 ± .084	.034	.057	.017	.028	.022	.022	.026
175	.616 ± .090	.034	.062	.019	.031	.024	.023	.027
180	.656 ± .094	.033	.066	.020	.033	.026	.025	.027
185	.697 ± .099	.033	.070	.020	.035	.028	.026	.027
190	.709 ± .099	.031	.071	.021	.035	.028	.027	.026
195	.716 ± .102	.029	.072	.030	.036	.028	.027	.025
200	.721 ± .102	.027	.072	.030	.036	.029	.027	.025
205	.799 ± .111	.028	.080	.031	.040	.032	.030	.027
210	.746 ± .104	.024	.075	.030	.037	.030	.028	.024
220	.812 ± .111	.023	.081	.031	.041	.032	.031	.026
230	.822 ± .112	.020	.082	.032	.041	.032	.031	.025

Table 5.4: Efficiencies for $t\bar{t}$ events.

is a muon with $p_T > 4$ GeV. Averaged over the run, the efficiency and acceptance reduce this to the 15.8% shown in the last row of Table 5.5. The tagging muons originate from direct b quark decays (54%), $b \to c$ cascade decays (33%), c quarks from on shell W decays (7%), direct on shell W decays or $W \to \tau$ (2%), and other sources including light quarks and gluons.

5.4 Backgrounds

The principle source of background is $W+$jets events with jets produced by gluon radiation and splitting. The rest is mostly from ordinary QCD multijet production with a false isolated electron (including both instrumental fakes and real electrons from b or c quark decays) and $\not\!\!E_T$ due to measurement fluctuations. There are small contributions from single t-quark, WW and WZ production.

Cut	Absolute	Relative
electron	8.80 ± .08	19.38 ± .14
$\not\!\!E_T$	7.86 ± .07	89.37 ± .26
trigger	7.86 ± .07	100.00 ± .00
clean event	7.85 ± .07	99.79 ± .04
$\not\!\!E_T$ with suppressed cells	7.79 ± .07	99.31 ± .07
$\Delta\phi(\mu, \not\!\!E_T)$	7.75 ± .07	99.49 ± .06
no 2nd electron	7.54 ± .07	97.21 ± .04
$\Delta R(e, j)$	7.18 ± .07	95.26 ± .19
$\geq$ 1 jet	7.15 ± .07	99.63 ± .06
$\geq$ 2 jets	6.75 ± .06	94.32 ± .22
$\geq$ 3 jets	4.93 ± .06	73.02 ± .43
H_T	4.82 ± .05	97.78 ± .17
$\mathcal{A}$	3.59 ± .05	74.60 ± .50
μ-tag	.57 ± .02	15.80 ± .44

Table 5.5: Signal acceptance [%] at various stages of selection for $m_t = 170$ GeV/c^2. The uncertainties due to Monte Carlo statistics are indicated.

5.4.1 False Electrons

The false electron background was estimated by relaxing the electron identification criteria and observing the number of additional events (mostly multijet) which enter the sample. The method is similar to that in Reference [56]. Of the five candidates four (one) have the electron in the CC (EC). With the loose electron definition from Section 4.2.1 used in place of the tight definition, i.e. the likelihood-ratio cut is not imposed, the numbers increase to eight (six). We know from having studied the electron efficiencies that the fraction of true electrons which pass the tight electron criteria given that they pass the loose criteria, ϵ_{te}, is 0.828 ± 0.010 (0.453 ± 0.015); so if there were no false electron events in the data we would have expected only about five (two) events in the loose sample. On the other hand, the fraction of false electrons which pass the tight electron criteria given that they pass the loose criteria, ϵ_{tf}, is expected to be 0.027 ± 0.009 (0.053 ± 0.012); so we would expect about 148 (19) if the data consisted entirely of false electron events in the loose sample. We suppose then that the samples of tight and loose electron candidates are mixtures of real and false electrons.

The parameter ϵ_{tf} was measured using data taken with the trigger `ele_1_mon` and having one electron candidate, no other good EM cluster, at least one jet and $\not\!\!E_T$ < 10 GeV. These conditions were designed to select a sample of false electrons minimally contaminated by real electrons from W and Z boson decays. To estimate of ϵ_{tf}, we use the ratio of the number of events containing a tight electron candidate to the number of loose electron events. The $\not\!\!E_T$ distributions for loose and tight CC candidates is shown in Figure 5.16. We found ϵ_{tf} to

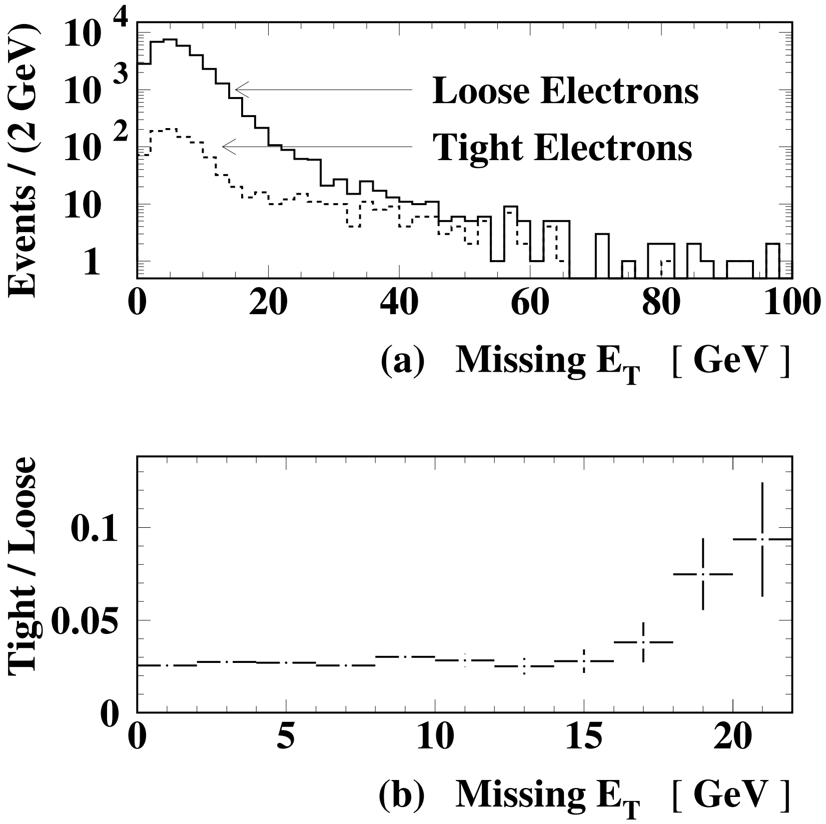

Figure 5.16: $\not\!\!E_T$ distributions for loose (solid histogram) and tight (dashed histogram) electron candidates in the CC.

be $.027 \pm .010(.053 \pm .010)$ in the CC (EC). The uncertainty in this quantity is dominated by our confidence in its stability as a function of jet multiplicity. Figure 5.17 shows that for events with at least one jet it appears to be stable within the statistical precision.

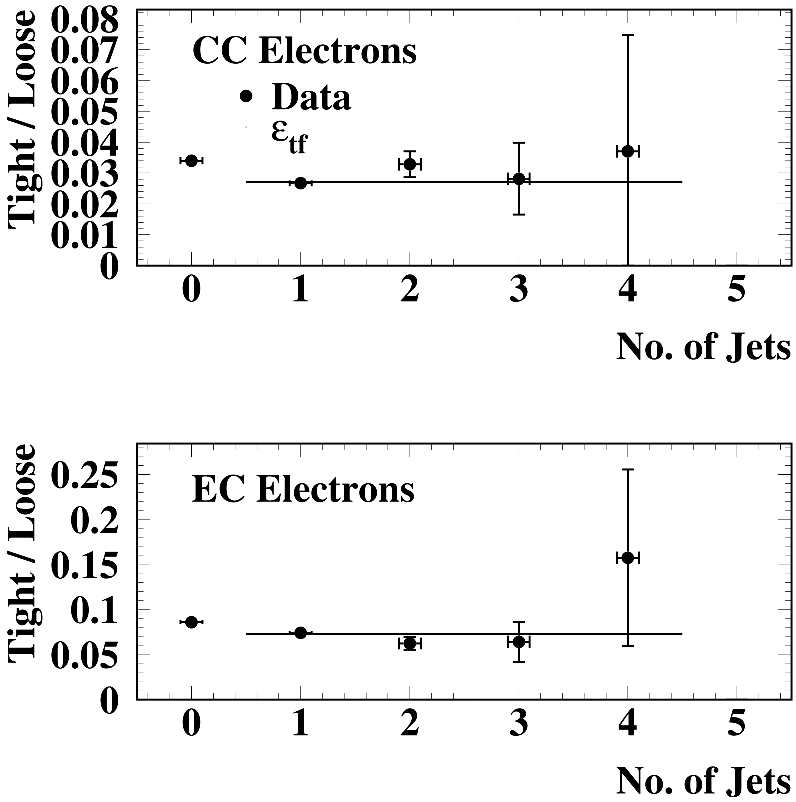

Figure 5.17: Stability of ϵ_{tf} as a function of jet multiplicity.

Let N_f (N_e) represent the number of false (real) electrons in the loose sample and let N_{tf} (N_{te}) represent the number of false (real) electrons in the tight sample. The actual values of these quantities are not known, but approximating the ratios N_{tf}/N_f and N_{te}/N_e by their expected values ϵ_{tf} and ϵ_{te} leads to the expression

$$N_t = \epsilon_{tf} N_f + \epsilon_{te} N_e \tag{5.2}$$

where N_t and N_l are the number of events in the tight and loose sample. The number of events in the loose sample is

$$N_l = N_e + N_f. \tag{5.3}$$

Equations 5.2 and 5.3 give

$$N_f = \frac{\epsilon_{te} N_l - N_t}{\epsilon_{te} - \epsilon_{tf}}. \tag{5.4}$$

For eight loose and four tight CC electrons N_f is estimated to be 3.28 and the expected number of false electrons in the tight electron sample is $\epsilon_{tf} \times N_f = 0.088$. The background for events with an electron in the EC was calculated in the same way. The total for CC and EC combined is 0.32.

These estimates are subject to a systematic uncertainty of 0.066 events (CC and EC combined) due to the uncertainties in ϵ_{te} and ϵ_{tf} and to a statistical uncertainty of 0.62 events due to the binomial fluctuations of N_{te}/N_e and (especially) N_{tf}/N_f about their expected values. It is worth noting that the statistical uncertainty assigned to the cross section, based on the square root of the number of candidate events, implicitly includes a factor of $\sqrt{B_i}$ for the Poisson fluctuations of each background i about its expected value B_i, but because $\sqrt{0.32} < 0.62$ an additional background uncertainty of $\sqrt{0.62^2 - 0.32} = 0.25$ was propagated to the cross section.

5.4.2 $W+$ jets

5.4.2.1 The Tag Rate

The fraction of jets that contain a muon was measured in a control sample of multijet data. The resulting measured tag rate was used to predict the number of tagged jets in the $W+$jets data. The control sample consists of events taken with the trigger `jet_multi`, having four or more jets reconstructed offline ($|\eta| < 2$,

$p_T > 15$ GeV), and satisfying the same event clean up conditions as the signal candidates (namely, the vetos on Main Ring activity and high CHF jets described in Section 5.2). This is a high statistics data set with more than 7×10^5 events taken almost continuously over the course of the run under essentially the same detector and accelerator conditions as the signal data. The control data and W + jets background have similar jet p_T and η distributions. Because both samples owe their high jet multiplicity to gluon radiation and splitting they also have similar quark flavor content.

The tag rate was parametrized explicitly as a function of jet p_T and η. The fractions of jets tagged by muons detected in the CF and EF parts of the muon system were parametrized separately. The η dependence was independently fit for three intervals of the run. Figure 5.18 shows the tag rate in the control sample as a function of jet p_T. The tag rate increases with jet p_T because higher energy jets have higher energy muons that are more likely to penetrate the calorimeter and magnet. The data were fit to the functional form

$$f(p_T) = \begin{cases} A_1 + A_2\, p_T + A_3\, p_T^2 & \text{for } p_T \leq \rho \\ A_1 + A_2\, \rho + A_3\, \rho^2 & \text{for } p_T > \rho \end{cases} \tag{5.5}$$

where $\rho = -\frac{1}{2}A_2/A_3$ and the parameters A_1, A_2 and A_3 were free. The resulting curves for CF and EF muons are denoted f^{CF} and f^{EF}. The dependence on jet η is shown in Figure 5.19. The shape is mostly due to the geometrical acceptance of the muon system but varies somewhat from one interval of the run to the next because of changes in the efficiency of the chambers. The data for CF muons were fit to the functional form

$$g^{\mathrm{CF}}(\eta, r) = B_{1,r}\,(1 + B_{4,r}\eta^2)\,[\mathrm{erf}(\eta B_{2,r} + B_{3,r}) - \mathrm{erf}(\eta B_{2,r} - B_{3,r})] \tag{5.6}$$

where r labels the three periods of the run, $\mathrm{erf}(x) = 2/\sqrt{\pi}\int_0^x \exp(-t^2)\,dt$ and the parameters $B_{1,r}$, $B_{2,r}$, $B_{3,r}$ and $B_{4,r}$ were free to vary. The data for EF muons were

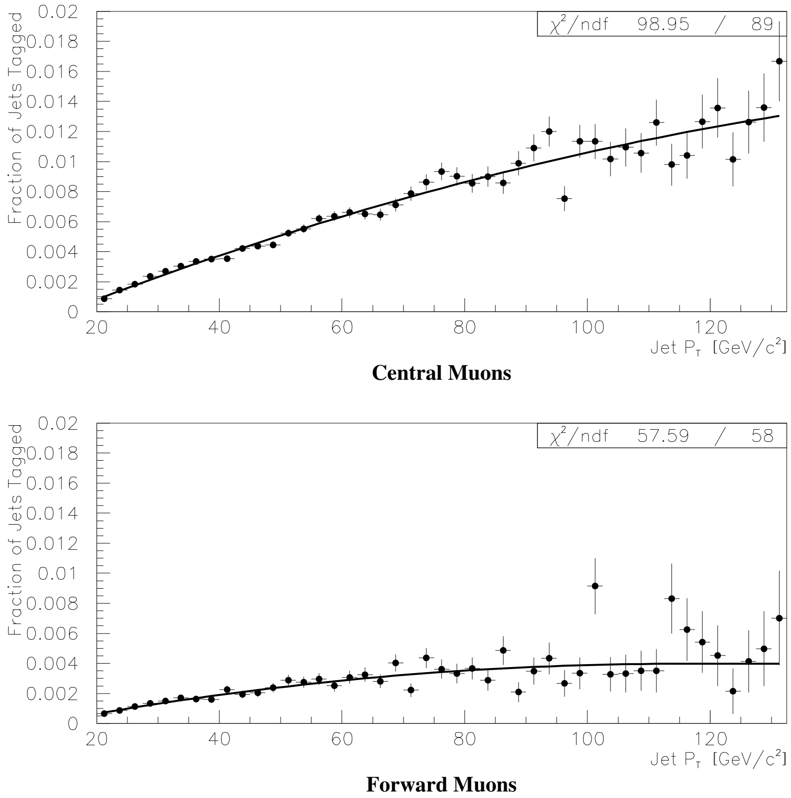

Figure 5.18: The dependence of the tag rate on jet p_T. The points are the multijet data and the curves are the results of the fit. The χ^2 per degree of freedom is shown in the upper right corner.

fit to

$$g^{\mathrm{EF}}(\eta) = C_1 \left\{ \mathrm{erf}[(|\eta| - C_4)C_2 + C_3] - \mathrm{erf}[(|\eta| - C_4)C_2 - C_3] \right\} \tag{5.7}$$

with free parameters C_1, C_2, C_3 and C_4. The complete tag rate is

$$R(p_T, \eta, r) = D_r^{\mathrm{CF}}\, f^{\mathrm{CF}}(p_T)\, g^{\mathrm{CF}}(\eta, r) + D_r^{\mathrm{EF}}\, f^{\mathrm{EF}}(p_T)\, g^{\mathrm{EF}}(\eta) \tag{5.8}$$

where D_r^{CF} and D_r^{EF} are constants which normalize the predicted number of tagged jets in the control sample to the actual number. Recall that muons from the EF were only used in the last part of the run. The values of the parameters are given in Table 5.6. To predict the number of tagged jets in a set of events, $R(p_T, \eta, r)$

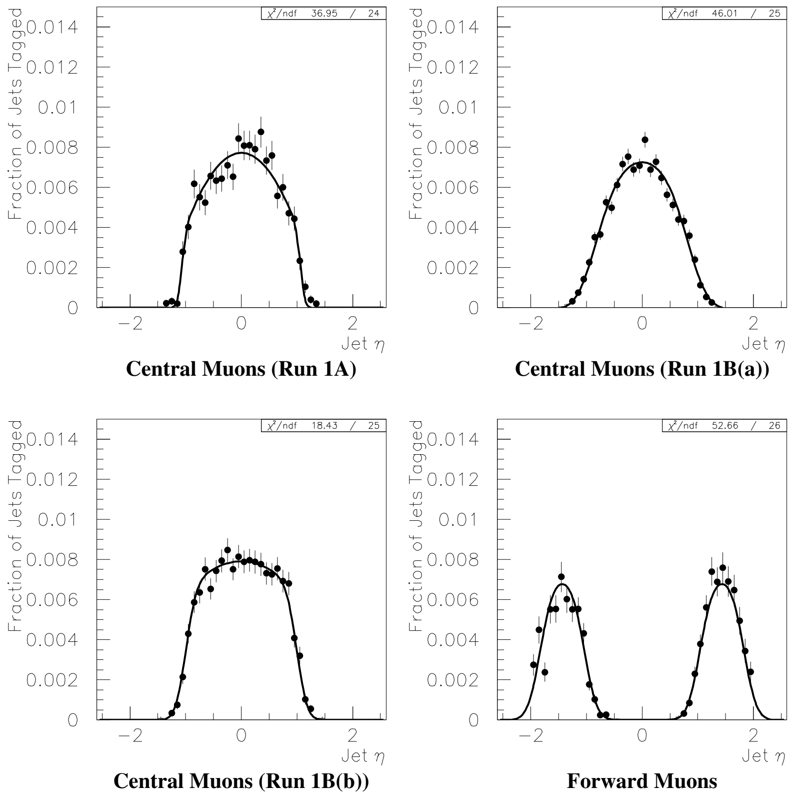

Figure 5.19: The dependence of the tag rate on jet η. The points are the multijet data and the curves are the results of the fit. The χ^2 per degree of freedom is shown in the upper right corner.

is summed over each eligible jet in all the events. The value of the tag rate is typically $\simeq 0.5\%$ per jet so there is little error in equating the predicted number of tagged jets to the expected number of events with a tagged jet.

5.4.2.2 Tests of the Tag Rate

The accuracy of this procedure has been studied by comparing the predicted to observed number of events having a tagged jet for a variety of data samples representing different trigger conditions, physics processes and jet multiplicities. Figure 5.20 lists these data samples and shows the results of the test. The test samples

f Parameters

	CF value	EF value
A_1	-0.2430E-02	-0.9022E-03
A_2	.1699E-03	0.8471E-04
A_3	-0.3967E-06	-0.3682E-06

g^{CF} Parameters

	r=1	r=2	r=3
$B_{1,r}$	0.3861E-02	0.3634E-02	0.3954E-02
$B_{2,r}$	11.45	2.264	4.783
$B_{3,r}$	12.37	2.166	4.846
$B_{4,r}$	-0.4825	-0.4766	-0.1982

g^{EF} Parameters

C_1	C_2	C_3	C_4
0.3489E-02	3.919	1.539	1.434

Normalization Parameters

	r=1	r=2	r=3
D_r^{CF}	249.638	248.697	223.355
D_r^{EF}	—	—	528.835

Table 5.6: Coefficients in the tag rate function.

were all subject to the event clean up conditions from Section 5.2.

The multijet sets with minimum jet multiplicity of two, three, four and five were taken with the triggers `jet_min`, `jet_3_mon`, `jet_4_mon` and `jet_multi` respectively. The last set is a complete subset of the data used to measure the tag rate, comprising about a third of the jets.

The electron sets consist of events with a tight electron candidate, taken with `ele_1_mon` (`gis_dijet`) for the case of one (two) or additional jets. Almost all of the 'electrons' are false. The purpose of examining these events is to check for an excess of tags due to $b\bar{b}$ or $c\bar{c}$ production where one heavy quark decays to an electron and the other to a muon. There is no evidence of an excess and none is expected because of the isolation and high p_T requirements on the electron.

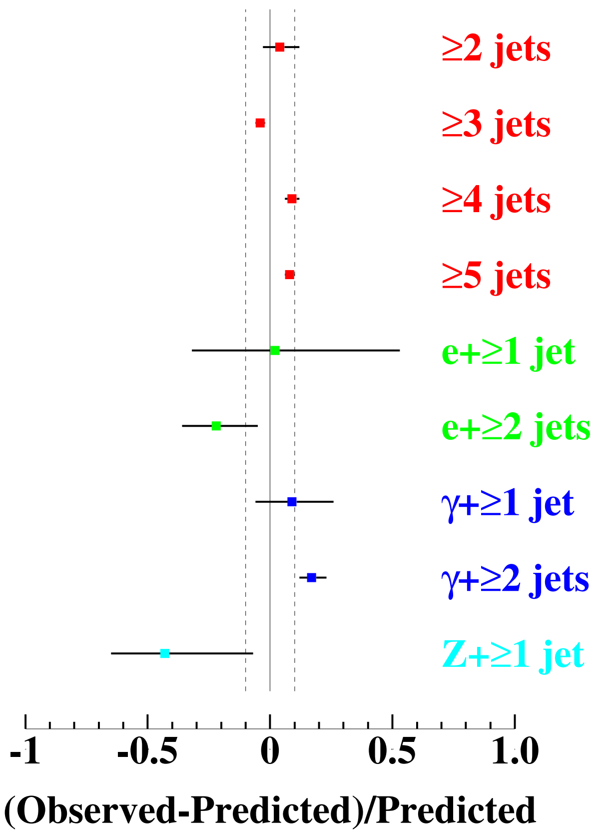

Figure 5.20: Results of applying the tag rate to test samples. Jets jets with $p_T > 20$ GeV and $|\eta| < 2$ are counted.

The photon sets consist of events with a tight photon candidate (see Section 4.2.2), taken with the same triggers as the electron sets. About 30% of the $\gamma+\geq 1$ jet data is from direct photon production and the rest is multijet background [57]. The purity is less in the $\gamma+\geq 2$ jet data.

The $Z+$jet data was from the trigger `em1_eistrkcc_esc`, with two loose electron candidates including at least one tight candidate. The invariant mass of the electron pair was required to be between 80 and 100 GeV. The background in this sample is low (10%); unfortunately so are the statistics—only four events with a tagged jet.

Some of the scatter in Figure 5.20 is due to statistics (indicated by horizontal error bars); the remainder is ascribed to systematic errors in the tag rate procedure. The value extracted for the systematic error using the formula from Appendix D is 8.2%. Note that the functional dependence of the tag rate is only important to the extent that the target sample differs from the control sample. The test samples with low jet multiplicity have a significantly steeper jet p_T spectrum than either the control sample or the $W+$jets data after the H_T and $\mathcal{A}$ cuts.

Since we are interested in the number of tagged events in a data sample which has been selected with cuts on H_T and aplanarity, we have checked that the tag rate does not depend on these quantities in an unexpected way. Figure 5.21 compares the predicted and observed numbers of tagged events as a function of H_T and $\mathcal{A}$ for the three jet and four jet multijet test samples. The aplanarity distributions are in very good agreement. The high statistics reveal differences in the H_T distributions such that a cut could result in a discrepancy of a few percent between the predicted and observed number of events.

The assumption that the flavor content in $W+$jets events is the same as in QCD multijet events was tested for the `HERWIG/QQ` model. After parton showering and hadronization, particle energies (for hadrons, electrons and photons) were recorded in 'towers' 0.1×0.1 in $\eta\times\phi$. Jets were reconstructed with a cone algorithm designed to match the one used for DØ data. Tagged jets were those containing muons with $p_T > 4$ GeV and having jet $p_T > 20$ (15) GeV after (before) adding the muon momentum. A tag rate was measured for events generated with the QCD $2\to 2$ hard parton scattering process with a minimum p_T of 50 GeV in which four jets with $p_T > 15$ GeV were found with the cone algorithm. This tag rate was applied to QCD $2\to 2$ hard parton scattering events generated with minimum p_T thresholds between 20 and 40 GeV, direct photon events with a 20 GeV p_T

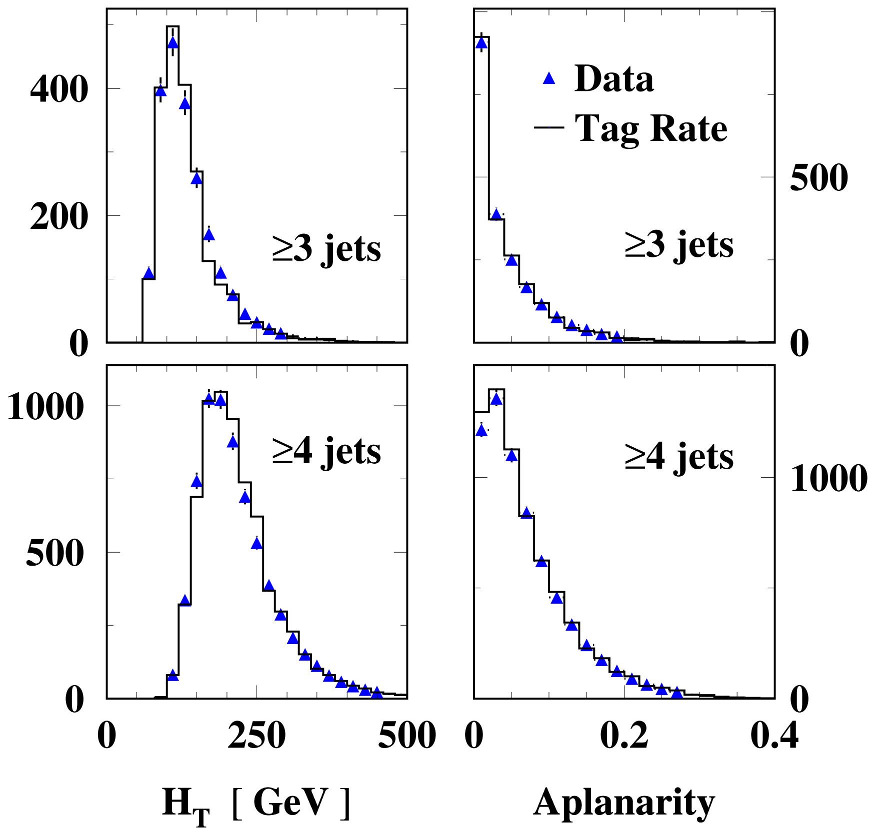

Figure 5.21: Predicted and observed number of tags in mulitjet data as a function of H_T and $\mathcal{A}$.

threshold, $W+$jet events with a 20 GeV p_T threshold, and Z boson events.[5] The results are shown in Figure 5.22. These results can not, of course, be compared directly to those from the data, since no account is taken of backgrounds, detector resolution, trigger biases, efficiencies, or uncertainties in the model of the physics processes. However, they give validity to the claim that the multijet tag rate can be used to predict the tags in $W+$jets events.

The number of $W+$jets candidates with a μ-tag, along with the estimated background distribution, is plotted in Figure 5.23 as a function of jet multiplicity.

[5]All of the jets in the Z boson events were from parton showers. There is not a $Z+$jet process in `HERWIG v. 5.8`.

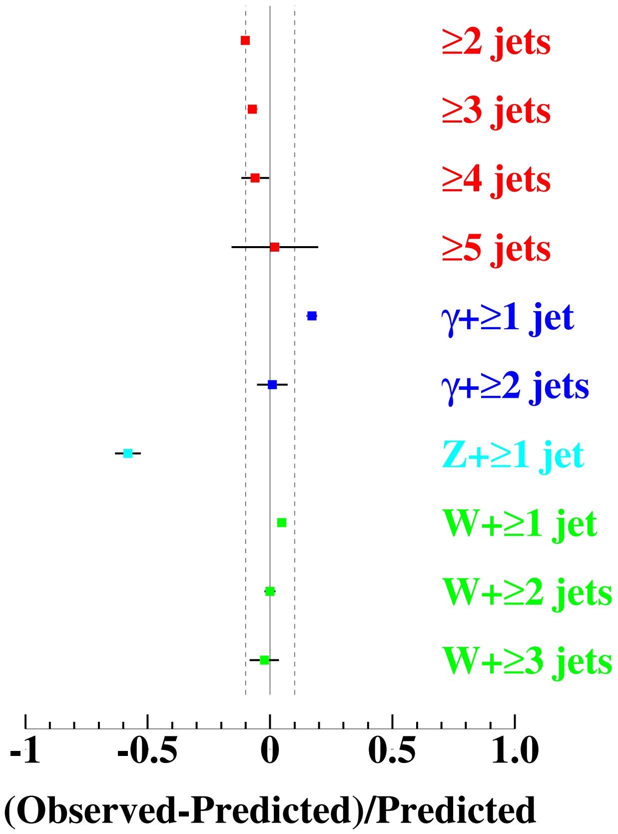

Figure 5.22: Test of the tag rate for Monte Carlo data.

At low jet multiplicities, one or two jets, the data and background prediction are close. For three or more jets there is an excess of events in the data consistent with $t\bar{t}$ production.

A systematic uncertainty of 10% was assigned to the tag rate prediction. Based on the results for the test samples, the low multiplicity W+jets data and the Monte Carlo, we believe that this is a reasonable estimate of the accuracy of the prediction for the $W+$jets background in the $t\bar{t}$ candidate sample.

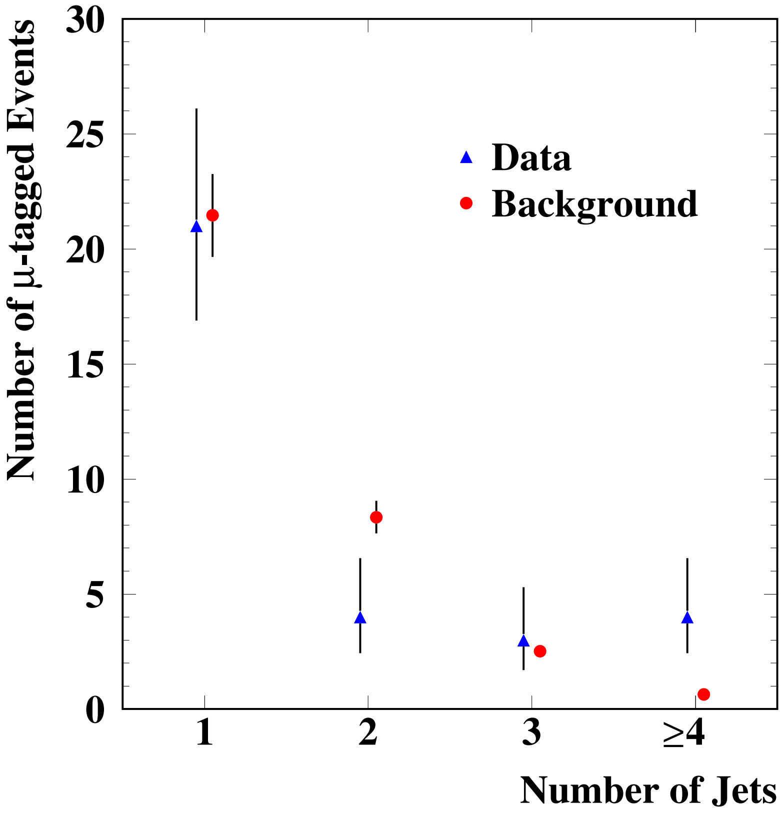

Figure 5.23: Number of muon tagged $e+$jets events versus jet multiplicity. The prediction for the background includes $W+$jets, multijet, and single top. Data taken with the inclusive W trigger `em1_eistrkcc_ms` is included and the electron p_T threshold raised to 25 GeV to minimize trigger biases.

5.4.2.3 Application to the $W+$jets Data

As shown in the second to last row of Table 5.2, there are 67 events in the candidate sample before the muon tag requirement. The average value of the tag rate for these events is almost 0.7% per jet, corresponding to a total of 1.58 expected events with a tagged jet. This includes a contribution from false electron events and from the $t\bar{t}$ signal. The $t\bar{t}$ contribution is discussed in Section 5.4.2.4. The false electron contribution was subtracted as in Section 5.4.1, resulting in 1.33 expected tagged events with a real electron. The weight contributed by false electron events, 0.25, is less than the background calculated directly in Section 5.4.1, 0.32. This is as expected since events containing a real muon are more likely to have the $\not\!\!E_T$ necessary to mimic a W boson decay and it is for this reason that a separate method is used to estimate the false electron background. However, because the difference is small the combined false electron and W+jets background is not very sensitive to the value of ϵ_{tf}: if, for example, ϵ_{tf} were overestimated the false electron background would be overestimated but the false electron corrected $W+$jets background would be underestimated.

5.4.2.4 Correction for Signal Events

When applied to the $W+$jets data, which includes the $t\bar{t}$ signal, the jet tag rate overestimates the number of tagged jets due to the background alone; symbolically, it gives $R \otimes$ (Background + Signal) rather than $R \otimes$ (Background). We subtracted off $R \otimes$ (Signal) by making an independent estimate of the number of $t\bar{t}$ events in the data sample prior to the μ-tag requirement and then multiplying by the average value of the tag rate per $t\bar{t}$ event calculated from the Monte Carlo.

Table 5.7 lists the number of W boson events (with the false electron background subtracted) satisfying the cuts up to and including electron—jet separation, except that instead of the triggers `ele_jet` and `ele_jet_high`, the inclusive W triggers, `ele_high` and `em1_eistrkcc_ms`, were required for Runs 1A and 1B respectively. Run 1C data is not included because there was not a suitable inclusive W trigger. The offline p_T threshold for the electron was raised to 25 GeV to avoid biases from the 20 GeV Level 2 requirement in these triggers. The inclusive W triggers were used because they had no jet requirement, which would bias the jet multiplicity distribution. Also listed in Table 5.7 is an estimated number of $t\bar{t}$ events for the same selection criteria, with the relative numbers of $t\bar{t}$ events at different jet multiplicities taken from the Monte Carlo.

No. of Jets	$W+$jets	$t\bar{t}$
≥ 0	60118	28.1
≥ 1	5608	28.0
≥ 2	745	26.4
≥ 3	122	19.2
≥ 4	20	9.8

Table 5.7: The number of events as a function of the minimum number of jets for the inclusive W data after subtraction of the false electron background and of the $t\bar{t}$ content. The absolute normalization of the number of $t\bar{t}$ events was determined by the fit described in the text.

According to the hypothesis of jet multiplicity scaling [64], the distribution of $W+$jets events in Table 5.7 can be described by a function of the form

$$n_i = n_3^W\,\alpha^{(i-3)} + n_3^{t\bar{t}}\,f_i/f_3 \tag{5.9}$$

where n_i is the number of events with i or more jets, n_3^W is the number of W events with three or more jets, $n_3^{t\bar{t}}$ is the number of $t\bar{t}$ events with three or more jets, f_i is the number of events in the $t\bar{t}$ Monte Carlo sample with i or more jets, and α is a free parameter. From a fit to Equation 5.9 we found $n_3^{t\bar{t}}$ to be 19.2 ± 9.5. The values of the other free parameters determined by the fit are $\alpha = 0.130 \pm 0.053$ and $n_3^W = 94.6 \pm 7.6$. The fit is shown in Figure 5.24. The validity of the claim that the number of events decreases by a constant fraction for each additional radiative jet has been tested for multijet data and the extrapolation has been found to be accurate to within 10% [65].

The distribution of tag rate weights per event for the Monte Carlo events passing all of the standard selection except for the muon-tag requirement is shown in Figure 5.25. The average value of this distribution is $\langle R\rangle_{evts}^{t\bar{t}} = 0.034$ and it's standard deviation is 0.011.

With this information we calculated

$$R \otimes (\text{Signal}) = n_3^{t\bar{t}}\frac{\varepsilon_{3j+H_T+\mathcal{A}}^{standard}}{\varepsilon_{3j}^{scaling}}\frac{L_{A+B+C}}{L_{A+B}}\langle R\rangle_{evts}^{t\bar{t}} \tag{5.10}$$

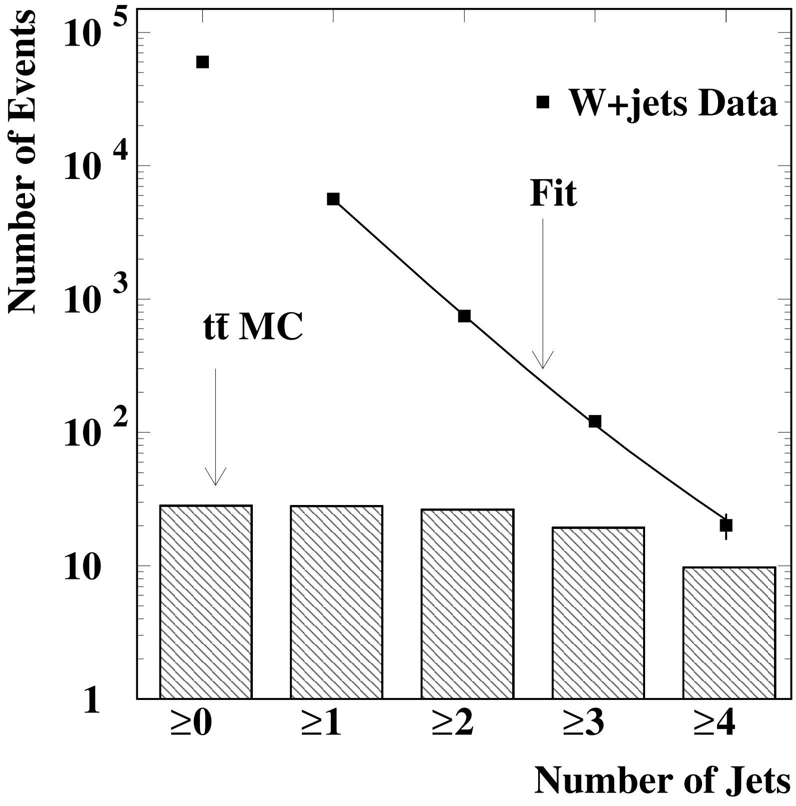

Figure 5.24: The fit for $n_3^{t\bar{t}}$ using jet multiplicity scaling.

where $\varepsilon_{3j+H_T+\mathcal{A}}^{standard} = 0.0359$ is the efficiency for $t\bar{t}$ events to pass all of the standard event selection except for the muon-tag requirement, $\varepsilon_{3j}^{scaling} = 0.0440$ is the efficiency for $t\bar{t}$ events to pass the jet-scaling selection and have at least three jets, and L_{A+B+C}/L_{A+B} is the ratio of the total integrated luminosity to the integrated luminosity in Runs 1A and 1B only. The result is $R \otimes (\text{Signal}) = 0.59 \pm 0.29$. The estimated background including this correction is shown in Table 5.8.

As a consistency check, recall that the tagging efficiency for $t\bar{t}$ events ε_{tag} is 0.158 and note that the jet scaling result predicts $[R \otimes (\text{Signal})]\varepsilon_{tag}/\langle R\rangle_{evts}^{t\bar{t}} = 2.7$ $t\bar{t}$ events in the candidate sample. This is in agreement with five candidates and a background of 1.06.

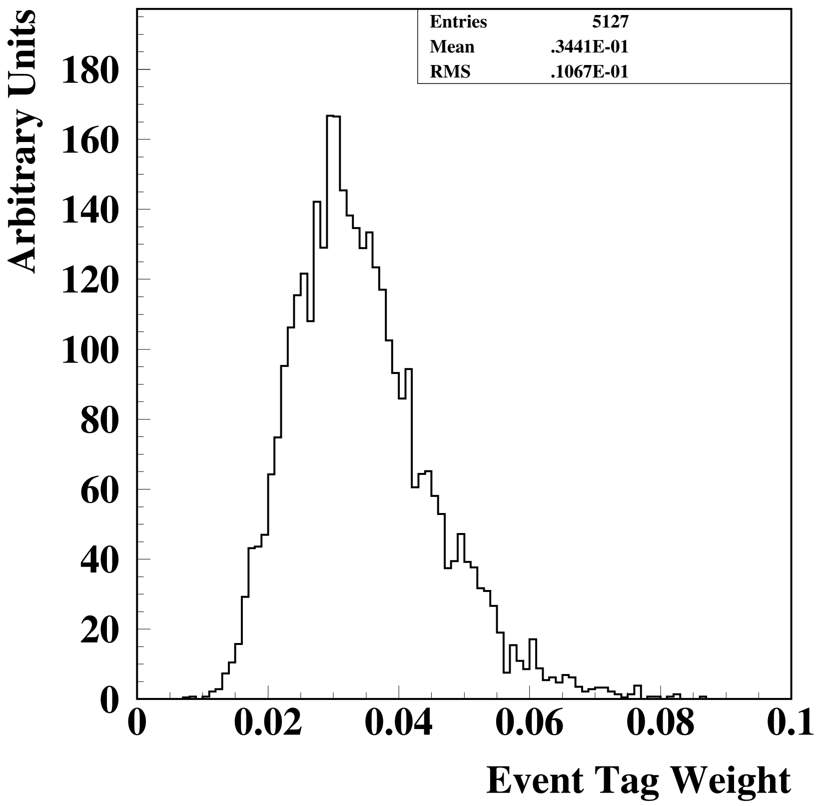

Figure 5.25: Event tag rate.

Alternatively, we can write the cross section in terms of the total uncorrected background $B' = 1.65$

$$\sigma_{t\bar{t}} = \frac{N - [B' - R \otimes (\text{Signal})]}{\mathcal{L}\, \varepsilon^{standard}_{3j+H_T+\mathcal{A}}\, \varepsilon_{tag}}, \tag{5.11}$$

where we have used $\varepsilon = \varepsilon^{standard}_{3j+H_T+\mathcal{A}} \varepsilon_{tag}$. The background correction can be expressed in terms of the cross section as

$$R \otimes (\text{Signal}) = \mathcal{L}\, \sigma_{t\bar{t}}\, \varepsilon^{standard}_{3j+H_T+\mathcal{A}}\, \langle R \rangle^{t\bar{t}}_{evts}. \tag{5.12}$$

Eliminating $R \otimes (\text{Signal})$ from Equations 5.11 and 5.12 gives

$$\sigma_{t\bar{t}} = \frac{N - B'}{\mathcal{L}\, \varepsilon^{standard}_{3j+H_T+\mathcal{A}} \left(\varepsilon_{tag} - \langle R \rangle^{t\bar{t}}_{evts}\right)}. \tag{5.13}$$

False electron	$.32 \pm .07\ (sys.) \pm .25\ (stat.)$
$W +$ jets	$.74 \pm .07\ (sys.) \pm .29\ (jet\, scaling)$
Total	$1.06 \pm .39$

Table 5.8: Expected backgrounds adjusted for $t\bar{t}$ contribution to predicted tags from $W +$ jets.

Using Equation 5.13 the cross section is 6.9 pb. This approach, of enforcing consistency between the cross section result and the background correction, allows one to avoid the necessity of invoking jet multiplicity scaling and produces an estimate of the correction which is of comparable accuracy. However, the correction derived from the consistency requirement is correlated with the statistical uncertainty in the cross section measurement, whereas the scaling estimate is independent. For the present statistics-limited measurements it pays to use the additional information that scaling provides. For future measurements it may not.

5.4.3 Other Physics Backgrounds

There are a number of ways to produce W bosons along with jets in which the jets arise from electroweak processes. These all have small cross sections but the quark flavors can be different on average than when the jets are produced through QCD processes. For example, the cross section times branching fractions to semileptonic decay for WW and WZ are 2.8 pb and 0.15 pb respectively [58]. There are also several processes which yield a single t-quark in the final state. One of these is s-channel production of $t\bar{b}$ (and the charge conjugate states, included implicitly) through a virtual W. The cross section for this process is 1.07 pb assuming $m_t = 170$ GeV/c^2 [59]. Another single t-quark process, W-gluon fusion, is $q'b \to qt$ by t-channel W exchange. The cross section calculated at next-to-leading order is 1.73 pb for $m_t = 170$ GeV/c^2 [60].

The acceptance of the event selection for WW and WZ was estimated using Monte Carlo events produced with PYTHIA/JETSET [61]. PYTHIA is a Monte Carlo generator that uses JETSET routines for final state parton showers and hadronization according to the LUND string fragmentation model. The detector simulation and other procedures from Section 5.3 were applied. For the single t-quark modes the parton level events were generated with CompHEP [62] and further processed with routines from PYTHIA/JETSET for parton showering and hadronization. For W-gluon fusion $q'g \to tqb$ and $q'b \to tq$ were generated separately and the contribution of the two types of event to the total cross section was assumed to be in the ratio calculated in [63].

The results are summarized in Table 5.9. Together the various sources are

Process	σ [pb]	Acceptance [%]	Expected Events	Tag Rate
$q'\overline{q} \to t\overline{b}$	1.07	0.003 ± 0.001	0.0035	0.00089
$q'g \to tqb$	1.02	0.03 ± 0.02	0.033	0.0058
$q'b \to tq$	0.71	0.0004 ± 0.0002	0.00031	0.00010
$WW \to l\nu qq$	2.8	0.011 ± 0.004	0.033	0.024
$WZ \to l\nu qq/llqq$	0.15	0.012 ± 0.004	0.0019	0.0011

Table 5.9: Other physics backgrounds

expected to contribute an additional 0.04 events to the background beyond what is predicted by the tag rate. We note that this is a small amount and do not include it in the cross section calculation.

Chapter 6

Other Signatures

6.1 $\mu + \text{jets}$ (μ-tag)

Muon tagging has also been applied to the study of $t\bar{t}$ decay modes in which one W boson yields a high p_T isolated muon [66]. The kinematic requirements in the event selection were the same as for for the $e + \text{jets}$ (μ-tag) signature; except that instead of a cut on the angle between the $\not{E}_T$ and the muon $\Delta(\not{E}_T, \mu) > 25°$, the angle between the highest p_T muon and the $\not{E}_T$ was required to satisfy $|\Delta(\not{E}_T, \mu) - 90°|/90° < \not{E}_T/(45\text{GeV})$. An additional requirement that the $\not{E}_T$ measured in the calorimeter alone, i.e. without correction for muons, be greater than 20 GeV was made in order to further reduce the multijet background in compensation for the muon momentum resolution.

As before, the principle backgrounds are direct W+jets production and multijet events. There is also an additional background from $Z + \text{jets}$ events where the Z boson decays to $\mu\mu$ and one of the muons overlaps with a jet. This background is reduced by a cut on the χ^2 of a fit to the hypothesis that the event is $Z \to \mu\mu$ with no real $\not{E}_T$. The level of the remaining background was calculated using Monte Carlo.

The $\mu + \text{jets}$ multijet background consists mostly of events with real muons from the semileptonic decay of b-quarks from $b\bar{b}$ production. There are also contributions from c-quark, $\pi^{\pm}$ and $K^{\pm}$ decay, but these are smaller because the muon p_T spectra for these sources are even softer than for $b\bar{b}$. Few objects detected in the muon system are not real muons. However, the momentum resolution for muons is significantly poorer than for electrons. Furthermore, it is the bend angle measurement, to which the momentum is inversely proportional, that has a gaussian resolution. Thus the measured momentum has a long tail at the high end. This allows muons from low energy sources to sometimes pass the high p_T threshold. If the calorimeter energy measurement of the accompanying hadrons fluctuates low, then these muons may also appear isolated. The muon tag rate for such events is higher than for ordinary multijet events because of the presence of the second b-quark.

The level of the multijet background in the candidate sample prior to the μ-tag requirement was estimated using a control sample in which the high p_T muons were not isolated. An estimate of the fraction of these events that have a muon tag was made using Monte Carlo. The $W + \text{jets}$ background was estimated using a tag rate. The results are shown in Table 6.1.

$W + \text{jets}$	0.73 ± 0.13
Multijet	0.50 ± 0.15
$Z \to \mu\mu$	0.16 ± 0.07
Total Background	1.39 ± 0.23
Expected $t\bar{t}$	2.25 ± 0.54
Candidates	6

Table 6.1: μ+jets (μ-tag) results. The expected number of $t\bar{t}$ events was calculated using the theoretical cross section from [23] for $m_t = 170$ GeV/c^2.

6.2 $l+\text{jets}$ (kinematic)

We have seen that by selecting events with $\not\!\!E_T$ and an isolated high p_T lepton we are left with a sample that originated predominantly from direct production of W bosons and that the contribution from $t\bar{t}$ production is comparatively small even after requiring the presence of several additional jets. The strategy described previously to reduce the background from direct W + jets was to look for jets containing muons to tag b-quark jets from t-quark decay. An alternative strategy is to make strict cuts on the kinematic properties of the events.

DØ has also pursued an analysis following this approach. The initial event selection was similar to that in Chapter 5. Events with a μ-tagged jet were removed from the sample to make it mutually exclusive with the tag candidate sample. A tight quality isolated lepton (electron or muon) with $p_T^l > 20$ GeV was required. The $\not\!\!E_T$ cut was set at 25 GeV. Four or more jets with $p_T > 15$ GeV and $|\eta| < 2$ were required. To further reduce the multijet background, the scalar sum of p_T^l and $\not\!\!E_T$ was required to be greater than 60 GeV. The W+jets background was reduced by cuts on H_T and $\mathcal{A}$ (defined in Section 5.2) at 180 GeV and 0.065 respectively. A total of 19 candidate events were found, nine (ten) in which the isolated lepton was an electron (muon). The expected background is 8.67 $\pm$ 1.74 events. The results are shown in Table 6.2.

	e	μ
W + jets	4.14 $\pm$ 0.82	3.20 $\pm$ 0.82
Multijet	0.38 $\pm$ 0.14	0.96 $\pm$ 0.44
Total Background	4.51 $\pm$ 0.91	4.16 $\pm$ 1.02
Expected $t\bar{t}$	8.63 $\pm$ 1.57	5.51 $\pm$ 1.67
Candidates	9	10

Table 6.2: l + jets (kinematic) results. The expected number of $t\bar{t}$ events was calculated using the theoretical cross section from [23] for $m_t = 170$ GeV/c^2.

The multijet backgrounds were estimated using control data samples in a way similar to that described in 5.4.1. The multijet control sample for the $\mu+$jets data was good quality, non-isolated muons.

The $W+$jets background was estimated using simulated $W+$jets events. These were generated using a version of the VECBOS program [64] adapted to produce unweighted events [69]. VECBOS is a leading order calculation of the $W+n$-parton cross section. The parton level events were further processed using HERWIG for parton showering and hadronization, and subsequently passed through the detector simulation. Prior to the $\mathcal{A}$ and H_T requirements, the candidate sample comprised about 100 events. The VECBOS Monte Carlo predicts that if these events were all from direct W production then about nine of them would pass the $\mathcal{A}$ and H_T cuts. This is to be compared to an efficiency of about 50% for $t\bar{t}$ events. Of course, some of the 100 events in the parent sample are multijet and some are $t\bar{t}$, so nine events is an overestimate of the $W+$ jets background. The actual number of $W+$ jets events in the parent sample was estimated using jet multiplicity scaling, as in Section 5.4.2.4.

6.3 Dilepton

The analyses of the dilepton signatures ($e\mu$ [65], ee [67] and $\mu\mu$ [68]) looked for events with two isolated high p_T electrons or muons. The p_T thresholds were set at 15 (20) GeV for $e\mu$ and $\mu\mu$ (ee). For $e\mu$ (ee) the $\not{E}_T$ threshold was 20 (25) GeV. The $\mu\mu$ analysis used a kinematic fit to remove $Z \to \mu\mu$ events rather than making an explicit $\not{E}_T$ cut. All of the dilepton analyses required two or more jets with $p_T > 20$ GeV and $|\eta| < 2.5$. The ee and $e\mu$ selection required that the scalar sum of the p_T of the jets and the highest p_T electron be greater than 120 GeV.

The $\mu\mu$ selection required that the scalar sum of the p_T of the jets be greater than 100 GeV. The results are shown in Table 6.3.

	$e\mu$	ee	$\mu\mu$
$Z/\gamma \to \tau\tau$	0.10 ± 0.18	0.08 ± 0.02	0.03 ± 0.02
$Z/\gamma \to ee$		0.05 ± 0.03	
$Z/\gamma \to \mu\mu$			0.62 ± 0.21
WW	0.07 ± 0.02	0.08 ± 0.02	0.01 ± 0.01
$b\bar{b}/c\bar{c}$		0.06 ± 0.01	
Multijet	0.04 ± 0.13	0.20 ± 0.05	0.07 ± 0.01
Total Background	0.21 ± 0.16	0.47 ± 0.09	0.73 ± 0.25
Expected $t\bar{t}$	2.20 ± 0.48	1.20 ± 0.18	0.64 ± 0.09
Candidates	3	1	1

Table 6.3: Dilepton results. The expected number of $t\bar{t}$ events was calculated using the theoretical cross section from [23] for $m_t = 170$ GeV/c^2.

The physics backgrounds to the $e\mu$ signature are quite low. The largest is $Z \to \tau\tau$ where one τ decays to an electron and the other decays to a muon. The background to the ee signature has a contribution from direct $Z \to ee$ decays but this was effectively suppressed by raising the $\not{E}_T$ threshold to 40 GeV for events in which the mass of the ee pair was within $\pm$ 12 GeV of the Z boson mass, $\simeq$ 91 GeV. The muon momentum resolution makes the identification of $Z \to \mu\mu$ events more difficult. As a result, this background is substantially higher. The acceptance of the event selection for the physics background sources was calculated using Monte Carlo. The simulated Z boson data was tuned to Z + jets data. The multijet background was measured using control data.

6.4 $e\nu$

One last signature, denoted $e\nu$, captures $t\bar{t}$ events which escape the other analyses but which the DØ detector is well suited to identify. The selection requires one isolated electron with $p_T > 20$ GeV, two or more jets with $p_T > 30$ GeV, $\not{E}_T > 50$

GeV and the transverse mass m_T of the electron–$\not\!\!E_T$ system to be greater than 115 GeV. The $t\bar{t}$ acceptance comes from several decay modes: ee and $e\mu$ (50%), $e+$ jets (33%) and $e\tau$ (17%). The strict $\not\!\!E_T$ requirement strongly suppresses the multijet background, which has a rapidly falling $\not\!\!E_T$ distribution. The m_T requirement removes $W+$jets events, for which the neutrino–electron transverse mass distribution falls precipitously beyond the W boson mass at $\simeq 80$ GeV/c^2. The level of the remaining physics backgrounds was estimated using Monte Carlo. The results are shown in Table 6.4.

$W+$jets	0.52 ± 0.27
Multijet	0.47 ± 0.13
WW	0.15 ± 0.05
WZ	0.02 ± 0.1
Total Background	1.17 ± 0.37
Expected $t\bar{t}$	1.66 ± 0.48
Candidates	4

Table 6.4: $e\nu$ results. The expected number of $t\bar{t}$ events was calculated using the theoretical cross section from [23] for $m_t = 170$ GeV/c^2.

6.5 Combined Cross Section Results

The various signatures are summarized in Table 6.5. Altogether, there are 39 candidate events with a background of 13.7 ± 2.2. The combined value of the cross section is 5.7 ± 1.9 pb for $m_t = 170$ GeV/c^2. This is in agreement with QCD calculations of $\sigma_{t\bar{t}}$ for the same mass: 5.83 pb [23], 6.48 pb [24] and 5.62 pb [25].

None of the signatures show a significant excess or deficit of events. The cross sections based on the individual signatures are within errors of one another. Since the uncertainties on the individual measurements are almost completely due to

	ll and $e\nu$	$l+$jets (kin.)	$l+$jets (μ-tag)	Combined
Candidates	9	11	19	39
Background	2.57 ± 0.64	2.44 ± 0.47	8.67 ± 1.74	13.7 ± 2.2
Luminosity	111.1 ± 5.9	106.6 ± 5.6	110.0 ± 5.8	109.6 ± 5.8
Efficiency [%]	0.88 ± 0.16	0.94 ± 0.15	2.21 ± 0.47	4.02 ± 0.69
$\sigma_{t\bar{t}}$ [pb]	6.6 ± 3.4	8.6 ± 3.7	4.3 ± 2.2	5.7 ± 1.9

Table 6.5: Summary of results from all signatures. The efficiencies are for $m_t = 170$ GeV/c^2.

statistics, the correlations between them are negligible for the purpose of this comparison.

The uncertainty assigned to the combined measurement takes correlations into account. The various sources contribute to the uncertainty in the combined cross section as shown in Table 6.6.

The CDF collaboration has reported comparable measurements. They find $m_t = 175.9 \pm 4.8$ (stat.) ± 4.9 (sys.) GeV/c^2 based on kinematic fitting of $l+$jets events and, using acceptances calculated for $m_t = 175$ GeV/c^2, they find $\sigma_{t\bar{t}} = 7.6^{+1.8}_{-1.5}$ pb based on dilepton, l+jets, and all hadronic signatures. For both the mass and cross section, the most important contributions to the CDF measurements are from $l+$jets decay modes where a b-quark jet was identified using a precision silicon vertex detector to observe the displacement between the primary interaction vertex and the vertex from which the decay products of a long lived B hadron emerged. Based on this signature alone, the cross section is $6.2^{+2.1}_{-1.7}$ pb. The results from the other individual signatures are higher. The combined CDF cross section measurement, though higher than the one from DØ, is within two standard deviations of the lowest of the three resummed NLO calculations.

Statistics	25%
Efficiency (detector related)	13%
Efficiency (generator related)	11%
Backgrounds	9%
Luminosity	5%
Total	33%

Table 6.6: Sources of uncertainty in the combined cross section.

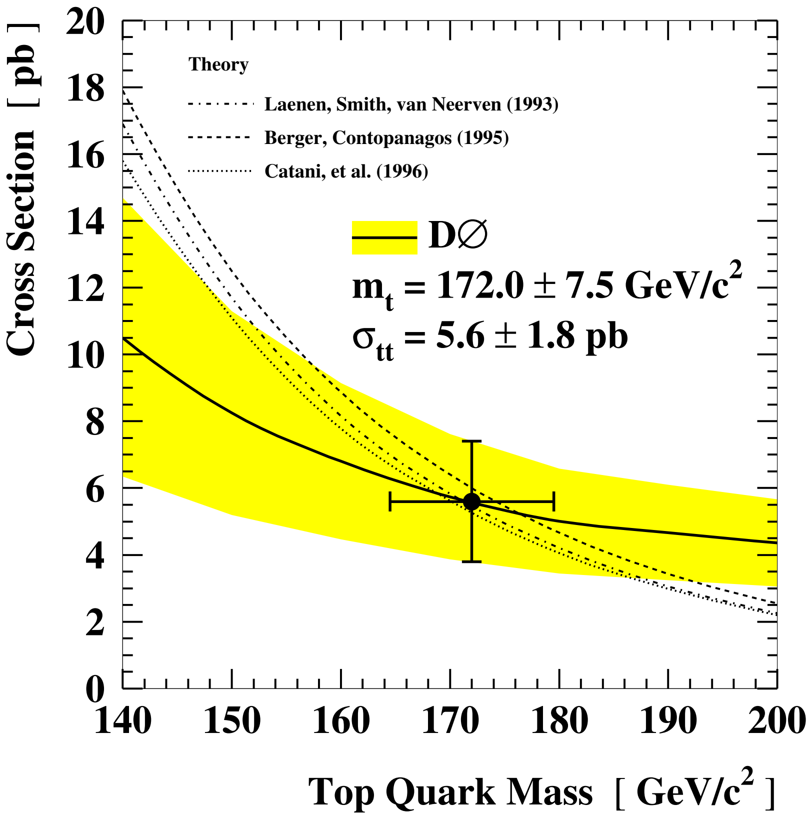

Figure 6.1: The cross section based on the combined signatures as a function of m_t.

Chapter 7

Conclusions

The cross section for $t\bar{t}$ production in $p\overline{p}$ collisions at $\sqrt{s} = 1.8$ TeV has been measured by counting events consistent with the decay of one top quark to $e\nu b$ and the other to $qq'b$. The measured cross section varies as a function of assumed top quark mass from $10.0^{+7.1}_{-4.6}\,(\text{stat.}) \pm 2.2\,(\text{sys.})$ pb to $5.1^{+3.6}_{-2.4}\,(\text{stat.}) \pm 0.8\,(\text{sys.})$ pb between masses of 140 and 200 GeV/c^2. At a mass of 170 GeV/c^2, near the measured value of m_t, the cross section is $6.4^{+4.5}_{-2.9}\,(\text{stat.}) \pm 1.2\,(\text{sys.})$ pb—closer to the expected value than would be expected given the size of the statistical uncertainty. The theoretical cross section decreases more rapidly with m_t than the experimental result, allowing a test of the prediction. The central values of the most recent calculations are within the experimental error band up to masses in excess of 200 GeV/c^2.

Measuring top quark properties depends crucially on controlling the background while preserving the rare signal events. The principle backgrounds to the $e\nu bbqq'$ decay signature are from direct W boson production and from QCD multijet production. The latter was suppressed by tight electron identification and isolation conditions, and by the requirement of substantial $\not{E}_T$ —to indicate the presence of a high p_T neutrino. The former was suppressed by the requirement of substantial hadronic jet activity, including at least one jet containing a muon—to tag the decay of a b-flavored hadron. The estimate of the residual background levels was accomplished using control data samples.

Tagging with muons is the only practical way to identify b-quarks at DØ. Therefore it provides the only evidence of the expected Wtb coupling, and it is the only way to suppress the $W+$ jets background without relying heavily upon simulated data to model the kinematics of $W+$ jets events. The signal to background ratio in the present analysis is about four to one. This compares favorably to the purity of b-tagged $t\bar{t} \to l+$ jets candidate samples used for the cross section measurement at the CDF experiment [80]. They have isolated 34 events with a background of 9.2 $\pm$ 1.5 using displaced vertex tags (made possible by a precision silicon vertex detector), and 40 events with a background of 22.6 $\pm$ 2.8 using soft lepton (electron or muon combined) tags. However, the efficiency for finding at least one muon tag in a $t\bar{t}$ event at DØ is about 16%, while at CDF the efficiency is 39% for the powerful displaced vertex method and 18% for soft leptons.

The five e+jets (μ-tag) candidate events together with other l+jets and dilepton samples from DØ amount to 39 events with a background of 13.7 $\pm$ 2.1. The $t\bar{t}$ cross section based on the combined sample is 5.7 $\pm$ 1.9 for $m_t = 170$ GeV/c^2. Interpolated to the central value of the mass measured at DØ, $m_t = 172.0 \pm 7.5$ GeV/c^2, the value is 5.6 $\pm$ 1.8 pb. These results are consistent with the expected production modes. The values of the cross section determined from the separate individual signatures are consistent with one another and with the expected top quark decay modes. The results from CDF are similar. They find a cross section of 7.6 $^{+1.8}_{-1.5}$ pb for $m_t = 175$ GeV/c^2, based on dilepton, single lepton and all jet signatures [80].

The observation of the top quark and the first measurements of its properties stand in further testimony to the validity of the Standard Model. Nevertheless, the high value of its mass makes the top quark a remarkable object and raises the possibility that it may yet be found to participate in new physical processes. To date, all of the top quark measurements are limited by the scarcity of candidate events. Furthermore, many of the largest systematic uncertainties could be reduced given control samples with improved statistics. Additional data will become available with the next period of collider operation at the Tevatron, Run 2, scheduled to begin in the year 2000.

The accelerator and the DØ and CDF detectors will undergo significant upgrades in preparation for Run 2. A new accelerator ring, the Main Injector, will replace the Main Ring in the accelerator chain, providing a factor of ten increase in the instantaneous luminosity. An additional storage ring will be built for the purpose of recycling antiprotons from one store to the next, providing a factor of two increase in luminosity. As a result, the first phase of Run 2, to last about two years, is expected to yield about 2 fb^{-1} of data. Furthermore, the center of mass energy of the Tevatron will be increased from 1.8 to 2 TeV, resulting in a 35% to 40% increase in the top quark cross section, depending on m_t [25]. Both CDF and DØ will have silicon vertex detectors designed for very good geometrical acceptance of b-quark jets from top quark decays. DØ will add a magnetic field to the tracking volume.

With the larger event yields and higher tagging efficiency for b-quark jets, it is expected that m_t will be measured with an uncertainty of about 1.6 GeV/c^2 and $\sigma_{t\bar{t}}$ with an uncertainty of about 8% [81]. These precisions will be comparable to the differences between theoretical calculations of $\sigma_{t\bar{t}}$ as a function of m_t, about 15% between the two most recent calculations. Most importantly, the improved statistics will allow more precise and compelling consistency checks between top quark signatures and will further test the interpretation of the data within the scope of the Standard Model.

Appendix A

Luminosity

For an idealized collider in which a uniform bunch containing n protons collides with a uniform bunch containing $\overline{n}$ antiprotons and the bunches overlap completely at one interaction region along the ring, the instantaneous luminosity is

$$\dot{\mathcal{L}} = \nu n \overline{n} / A \tag{A.1}$$

where ν is the rotation frequency and A is the cross sectional area of the beam. In a real collider the individual particles are not distributed uniformly in space throughout a bunch and they have motion with respect to the ideal beam orbit. At the Tevatron, information about the structure of the beam is inferred by flipping a wire through the path of the beam and measuring the distribution of interaction products downstream. An estimate of the luminosity can thus be made from first principles [70]. However, there are uncertainties associated with this calculation of order 10% from the number of particles in the bunches and of order 10% from the beam structure [71]

The cross section σ for any process is defined to be

$$\sigma = R / \dot{\mathcal{L}} \tag{A.2}$$

where R is the rate at which the process occurs. DØ determined the luminosity from Equation A.2 by measuring the rate at which minimum bias interactions [1] occurred and using the independently measured total inelastic $p\overline{p}$ cross section σ_{inel}. Let N be the number of beam crossings over a short time (compared to the scale on which the machine luminosity varies) and let N_{MB} be the number of these crossings in which coincident hits were recorded in the Level 0 detectors. N and N_{MB} are related to the average number of interactions per crossing $\overline{N}$ by the Poisson distribution, $\overline{N} = -\ln(1 - N_{MB}/N)$. The rate R at which minimum bias interactions occurred is $\overline{N}/\tau$ where τ is the time between crossings. The cross section for minimum bias interactions σ_{MB} is σ_{inel} times the Level 0 efficiency. The Level 0 efficiency was calculated using specialized Monte Carlo simulations [72]. σ_{inel} has been measured by two experiments [73] [74] using a method which does not rely on knowledge of the luminosity. This method exploits the optical theorem to express the total cross section in terms of the total elastic plus inelastic rate, the elastic rate in the limit of vanishing momentum transfer, and the ratio of the imaginary component of the forward scattering amplitude to the real component. The latter quantity can be measured at low center of mass energies by comparing elastic pp and $p\overline{p}$ scattering at small angles and can be extrapolated to higher energy [75]. The former two quantities are measured in the dedicated experiments. Unfortunately, the two experiments are not in very close agreement. For example, Reference [73] measured the total inelastic cross section to be 55.5 ± 2.2 mb while Reference [74] found 60.3 ± 1.4 mb. DØ uses the weighted average of these measurements and assigns an uncertainty of 5.3% [72]. This uncertainty dominates the uncertainty on the luminosity. The integrated luminosity $\mathcal{L} = \int \dot{\mathcal{L}}\, dt$ for each of the periods of the Run are given in Table A.1 [76].

[1] Minimum bias interactions are defined to be those which fired the Level 0 trigger.

Run Range	$\int L\,dt$ (pb^{-1})
1A	13.9
1B(a)	50.8
1B(b)	33.9
1C	9.6
Total	108.3 $\pm$ 5.7

Table A.1: Integrated luminosity.

Appendix B

Candidate Events

The properties of the $e+$jets (μ-tag) candidate events are tabulated below. Also included are the four events which pass all of the selection criteria except for the H_T or $\mathcal{A}$ cuts. Each event is identified by the run and event numbers assigned by the online data acquisition system. The first table for each event lists the four-momentum components, p_T, η and ϕ of the electron, muons and jets. Jets satisfying $p_T > 15$ GeV and $|\eta| < 2.5$ are listed and they include those which match good electrons and photons. The next table lists the properties of objects found by the trigger. The first column gives the missing transverse energy calculated at Level 2 $\not{E}_T^{l2}$. The second and third columns give the transverse energy of the Level 1 and Level 2 electron candidates (E_T^{l1e} and E_T^{l2e} respectively) which match the offline tight electron. Columns four to six (seven to nine) give the transverse energy, η and ϕ of jets found at Level 1 (Level 2). The next table gives the electron quality variables. The fourth table gives the course hadronic fraction, electromagnetic fraction, and their difference for the jets. The last table gives global properties of the event. The first column lists the z position of the reconstructed vertices with the principle vertex listed first. The second column gives the z-intercept of the electron.[1] The next columns give H_T, aplanarity, the transverse mass M_T^W of the electron-$\not\!\!E_T$ system, the transverse momentum p_T^W of the electron-$\not\!\!E_T$ system, the instantaneous luminosity $\dot{\mathcal{L}}$ in 10^{30} cm^{-2}s^{-1}, and the value of the multiple interaction tool. The value of the multiple interaction tool [79] is based on the timing information from Level 0, the total energy deposited in the calorimeter, and the vertex positions reconstructed using tracking. It has the following meaning: (1) 'Most likely' a single interaction. (2) 'Likely' a single interaction. (3) 'Likely' a multiple interaction. (4) 'Most likely' a multiple interaction. (5) 'Most likely' a multiple interaction and 'likely' three or more interactions.

[1] The z-intercept of the electron's trajectory was determined by a line between the centroid of the EM calorimeter cluster and the average position of the drift chamber hits. This method is more accurate than using the angle of the reconstructed track (about 2 cm resolution compared to about 3 cm resolution) because of errors in the delay line calibration [78].

Run: 62199 Event: 13305

Object	E	p_x	p_y	p_z	p_T	η	ϕ
e	112.3	61.5	-21.9	91.4	65.3	1.14	5.94
$\not{E}_T$	30.6	-8.5	-29.4	.9	30.6	.03	4.43
j	89.7	77.6	-12.5	-39.8	78.6	-.49	6.12
j	92.5	-56.0	71.7	5.6	91.0	.08	2.23
j	119.3	64.8	-24.7	96.9	69.4	1.14	5.92
j	51.1	-46.5	-2.4	19.1	46.5	.40	3.19
j	60.2	-31.4	-6.7	50.2	32.1	1.23	3.35
j	100.1	-11.6	-7.4	99.0	13.8	2.67	3.71
j	23.1	-9.5	8.3	-18.9	12.7	-1.19	2.42
j	15.6	8.5	2.2	-12.7	8.7	-1.17	.26
μ	15.0	-9.5	11.6	.3	15.0	.02	2.26
μ	4.2	-2.6	3.3	-.2	4.2	-.05	2.23

$\not{E}_T^{l2}$	E_T^{l1e}	E_T^{l2e}	E_T^{l1j}	η^{l1j}	ϕ^{l1j}	E_T^{l2j}	η^{l2j}	ϕ^{l2j}
19.7	48.0	70.8	48.2	.9	6.0	73.7	1.0	5.9
			40.5	-.7	6.2	74.8	-.6	6.1
			37.2	-.1	2.3	61.7	.1	2.2
			29.5	1.1	6.0	49.5	.4	3.2
			21.8	.1	3.2	12.4	2.6	3.8
			8.2	-.5	6.2	26.5	1.2	3.4
			8.2	.1	3.0			
			7.8	-.3	2.3			
			5.5	-.7	5.6			
			5.5	-.1	2.1			
			5.0	-.9	5.6			
			4.5	.3	2.1			
			4.2	2.7	3.8			
			4.0	1.1	3.2			
			3.8	.3	3.0			

$\mathcal{I}$	χ_e^2	σ_{trk}	dE/dx	VTX dE/dx	f_{EM}	ϵ_{TRD}	L_e
.052	46.638	1.098	1.155	1.288	.990	.307	.055

CHF	EMF	CHF$-$EMF
-.001	.775	-.775
.064	.431	-.367
.000	.998	-.998
-.003	.947	-.950
.100	.551	-.451
-.002	.779	-.781
.015	.444	-.429
.028	.275	-.247

vertex-z	e z-int.	H_T	$\mathcal{A}$	M_T^W	p_T^W	$\mathcal{L}$	MI tool
-21.883	-25.635	248.240	.076	61.292	73.778	5.574	4
.3							
-40.3							

Run: 84681 Event: 13015

Object	E	p_x	p_y	p_z	p_T	η	ϕ
e	87.5	-60.2	-23.5	-58.9	64.7	-.82	3.51
$\not\!\!E_T$	57.4	41.7	-7.7	-38.7	42.4	-.82	6.10
j	92.0	-63.2	-24.5	-61.9	67.7	-.82	3.51
j	93.8	84.5	3.1	-36.9	84.6	-.40	.07
j	67.7	-57.1	19.2	28.9	60.2	.46	2.82
j	63.7	-22.1	-4.2	59.2	22.5	1.69	3.33
μ	24.7	22.1	-1.3	-11.0	22.1	-.48	6.22

$\not\!\!E_T^{l2}$	E_T^{l1e}	E_T^{l2e}	E_T^{l1j}	η^{l1j}	ϕ^{l1j}	E_T^{l2j}	η^{l2j}	ϕ^{l2j}
62.8	54.8	56.1						

$\mathcal{I}$	χ_e^2	σ_{trk}	dE/dx	VTX dE/dx	f_{EM}	ϵ_{TRD}	L_e
.051	19.569	1.033	2.642	.000	1.002	.041	.192

CHF	EMF	CHF$-$EMF
.001	.973	-.972
.037	.662	-.625
.002	.455	-.453
-.005	.541	-.545

vertex-z	e z-int.	H_T	$\mathcal{A}$	M_T^W	p_T^W	$\mathcal{L}$	MI tool
-14.953	-11.446	167.363	.032	100.748	36.326	4.438	1

Run: 85129 Event: 19079

Object	E	p_x	p_y	p_z	p_T	η	ϕ
e	51.0	20.1	-38.0	27.3	43.0	.60	5.20
$\not{E}_T$	37.4	11.6	34.1	-10.0	36.0	-.27	1.24
j	65.6	-46.1	-4.4	-45.7	46.3	-.87	3.24
j	51.0	20.1	-38.0	27.3	43.0	.60	5.20
j	51.7	-46.6	-21.5	1.4	51.3	.04	3.59
j	29.9	17.3	23.0	6.1	28.7	.21	.93
j	24.7	19.7	-9.0	-11.2	21.6	-.50	5.85
j	45.1	11.8	13.7	-41.2	18.1	-1.56	.86
μ	6.0	-5.7	-1.8	.0	6.0	-.01	3.45
μ	5.6	-5.1	-2.4	.0	5.6	.00	3.58

$\not{E}_T^{l2}$	E_T^{l1e}	E_T^{l2e}	E_T^{l1j}	η^{l1j}	ϕ^{l1j}	E_T^{l2j}	η^{l2j}	ϕ^{l2j}
27.4	35.0	39.6						

$\mathcal{I}$	χ_e^2	σ_{trk}	dE/dx	VTX dE/dx	f_{EM}	ϵ_{TRD}	L_e
.006	49.420	1.056	.736	.995	1.000	.601	.034

CHF	EMF	CHF−EMF
.015	.624	-.609
.000	1.000	-1.000
.168	.231	-.062
.019	.405	-.386
-.014	.470	-.484
.000	.246	-.246

vertex-z	e z-int.	H_T	$\mathcal{A}$	M_T^W	p_T^W	$\mathcal{L}$	MI tool
9.026	12.673	166.117	.090	72.260	31.931	6.554	3

Run: 85781 Event: 10705

Object	E	p_x	p_y	p_z	p_T	η	ϕ
e	23.6	12.2	-20.0	-2.6	23.5	-.11	5.26
$\not{E}_T$	168.9	39.1	-34.2	160.7	51.9	1.85	5.56
j	83.6	-12.4	71.6	40.3	72.7	.53	1.74
j	91.2	-30.2	-1.2	-85.5	30.2	-1.76	3.18
j	23.6	12.2	-20.0	-2.6	23.5	-.11	5.26
j	24.7	-4.7	-23.7	.5	24.1	.03	4.55
μ	6.3	-1.9	-6.0	-.2	6.3	-.03	4.41

$\not{E}_T^{l2}$	E_T^{l1e}	E_T^{l2e}	E_T^{l1j}	η^{l1j}	ϕ^{l1j}	E_T^{l2j}	η^{l2j}	ϕ^{l2j}
47.7	21.2	22.4						

$\mathcal{I}$	χ_e^2	σ_{trk}	dE/dx	VTX dE/dx	f_{EM}	ϵ_{TRD}	L_e
.028	59.086	1.366	.767	1.663	.988	.616	.073

CHF	EMF	CHF−EMF
-.006	.478	-.483
.005	.687	-.682
.000	.989	-.989
.167	.382	-.215

vertex-z	e z-int.	H_T	$\mathcal{A}$	M_T^W	p_T^W	$\mathcal{L}$	MI tool
11.911	11.185	126.979	.006	10.562	74.657	4.619	1

Run: 86570 Event: 8642

Object	E	p_x	p_y	p_z	p_T	η	ϕ
e	88.4	-30.2	28.4	78.1	41.5	1.39	2.39
$\not\!\!E_T$	23.4	18.9	8.4	-10.8	20.7	-.50	.42
j	58.8	-40.8	-34.2	-23.2	53.2	-.42	3.84
j	88.4	-30.2	28.4	78.1	41.5	1.39	2.39
j	73.0	16.0	30.5	-64.0	34.4	-1.38	1.09
j	30.8	13.5	-26.3	-6.4	29.6	-.21	5.19
j	34.8	32.3	-4.2	11.3	32.5	.35	6.13
μ	9.9	9.4	-.6	3.2	9.4	.33	6.22

$\not\!\!E_T^{l2}$	E_T^{l1e}	E_T^{l2e}	E_T^{l1j}	η^{l1j}	ϕ^{l1j}	E_T^{l2j}	η^{l2j}	ϕ^{l2j}
23.1	36.8	35.4						

$\mathcal{I}$	χ_e^2	σ_{trk}	dE/dx	VTX dE/dx	$f_{\rm EM}$	$\epsilon_{\rm TRD}$	L_e
.014	20.254	2.935	.723	.426	.992	.931	.140

CHF	EMF	CHF−EMF
.053	.595	-.542
.000	.993	-.993
.008	.237	-.229
.028	.296	-.268
.088	.663	-.574

vertex-z	e z-int.	H_T	$\mathcal{A}$	M_T^W	p_T^W	$\mathcal{L}$	MI tool
15.194	18.872	149.741	.215	48.836	38.528	4.773	3
-8.3							

Run: 87987 Event: 1228

Object	E	p_x	p_y	p_z	p_T	η	ϕ
e	80.9	42.0	55.6	41.1	69.7	.56	.92
$\not{E}_T$	50.7	-6.8	-43.1	25.8	43.6	.56	4.56
j	81.6	42.5	56.0	41.2	70.3	.56	.92
j	99.5	-17.1	43.1	-87.6	46.3	-1.39	1.95
j	57.7	3.0	-56.5	5.1	56.5	.09	4.76
j	23.8	-21.6	-4.8	5.5	22.1	.25	3.36
μ	14.6	.8	-14.6	1.2	14.6	.08	4.77

$\not{E}_T^{l2}$	E_T^{l1e}	E_T^{l2e}	E_T^{l1j}	η^{l1j}	ϕ^{l1j}	E_T^{l2j}	η^{l2j}	ϕ^{l2j}
56.5	60.5	61.5						

$\mathcal{I}$	χ_e^2	σ_{trk}	dE/dx	VTX dE/dx	f_{EM}	ϵ_{TRD}	L_e
.025	39.527	1.569	1.138	1.398	1.003	.747	.029

CHF	EMF	CHF−EMF
.001	.995	-.994
.179	.107	.072
.143	.284	-.141
.000	.494	-.494

vertex-z	e z-int.	H_T	$\mathcal{A}$	M_T^W	p_T^W	$\mathcal{L}$	MI tool
11.811	9.686	125.028	.051	106.986	37.338	8.137	1

Run: 89372 Event: 12467

Object	E	p_x	p_y	p_z	p_T	η	ϕ
e	137.3	80.1	103.3	41.8	130.7	.31	.91
$\not{E}_T$	53.8	11.4	43.4	-29.8	44.8	-.62	1.31
j	189.8	-64.7	-169.7	-50.5	181.7	-.27	4.35
j	140.1	80.7	105.3	44.1	132.7	.33	.92
j	105.5	-22.1	-38.1	-95.8	44.1	-1.52	4.19
j	30.6	-11.5	24.6	12.9	27.2	.46	2.01
j	41.3	8.5	36.9	-14.5	37.9	-.44	1.36
μ	18.1	4.2	16.8	-5.2	17.3	-.30	1.32

$\not{E}_T^{l2}$	E_T^{l1e}	E_T^{l2e}	E_T^{l1j}	η^{l1j}	ϕ^{l1j}	E_T^{l2j}	η^{l2j}	ϕ^{l2j}
64.1	61.8	90.2	75.8	.3	4.4	162.7	-.2	4.4
			62.8	.9	.9	119.8	.5	.9
			31.0	.3	4.2	29.7	.4	2.0
			10.2	.9	2.1	44.0	-1.4	4.2
			10.0	.5	4.4			
			8.8	.1	4.2			
			8.5	-1.1	4.2			
			7.8	-1.3	4.2			
			6.8	.1	4.4			
			6.0	.7	.9			
			4.2	.5	4.2			
			3.0	.1	1.5			

$\mathcal{I}$	χ_e^2	σ_{trk}	dE/dx	VTX dE/dx	$f_{\rm EM}$	$\epsilon_{\rm TRD}$	L_e
.036	46.625	1.876	1.125	.000	.979	.572	.107

CHF	EMF	CHF−EMF
.034	.575	-.541
.004	.975	-.970
.004	.176	-.172
.027	.127	-.100
.091	.460	-.369

vertex-z	e z-int.	H_T	$\mathcal{A}$	M_T^W	p_T^W	$\mathcal{L}$	MI tool
60.581	58.650	290.791	.021	30.665	172.886	9.632	2

Run: 91206 Event: 13727

Object	E	p_x	p_y	p_z	p_T	η	ϕ
e	121.0	95.6	-16.3	-72.2	97.0	-.69	6.11
$\not\!\!E_T$	37.9	28.9	19.4	15.2	34.8	.42	.59
j	200.7	-163.3	-56.2	-92.4	172.7	-.48	3.47
j	121.0	95.6	-16.3	-72.2	97.0	-.69	6.11
j	125.9	85.3	42.6	-81.6	95.3	-.78	.46
j	50.0	-46.1	-.1	17.1	46.1	.36	3.14
μ	16.9	-11.4	-4.3	-11.7	12.2	-.85	3.50

$\not\!\!E_T^{l2}$	E_T^{l1e}	E_T^{l2e}	E_T^{l1j}	η^{l1j}	ϕ^{l1j}	E_T^{l2j}	η^{l2j}	ϕ^{l2j}
22.7	61.8	75.9	63.2	-.9	6.2	155.7	-.9	.1
			44.0	-.7	3.4	135.6	-.6	3.4
			43.0	-1.1	.5	36.2	.2	3.1
			16.5	-.7	3.6			
			15.0	.1	3.2			
			14.8	-.9	.5			
			11.8	-.9	3.4			
			8.2	-.5	3.6			
			8.0	.3	3.2			
			6.5	-.5	3.4			
			6.2	-1.1	3.4			
			5.8	.1	3.0			
			4.5	-.9	3.2			
			4.2	-.7	3.2			
			4.2	.3	3.0			
			3.8	-.7	6.2			
			3.5	-.3	3.6			
			3.2	-1.1	3.2			

$\mathcal{I}$	χ^2_e	σ_{trk}	dE/dx	VTX dE/dx	$f_{\rm EM}$	$\epsilon_{\rm TRD}$	L_e
.025	44.293	.996	.669	1.168	.983	.496	.066

CHF	EMF	CHF−EMF
.039	.530	-.491
.000	.988	-.988
.185	.643	-.458
.023	.274	-.252

vertex-z	e z-int.	H_T	$\mathcal{A}$	M_T^W	p_T^W	$\mathcal{L}$	MI tool
-31.283	-28.686	314.068	.028	43.143	124.531	11.433	4
20.5							

Run: 95653 Event: 10822

Object	E	p_x	p_y	p_z	p_T	η	ϕ
e	62.7	52.6	-4.1	-33.8	52.8	-.60	6.20
$\not{E}_T$	73.6	56.1	-5.7	47.3	56.4	.76	6.18
j	99.0	-80.2	-23.3	-52.4	83.5	-.59	3.42
j	62.7	52.7	-4.1	-33.8	52.8	-.60	6.20
j	47.7	-23.0	24.7	-32.7	33.7	-.86	2.32
j	38.9	-8.5	-26.4	27.3	27.7	.87	4.40
j	31.8	.0	26.0	17.5	26.0	.63	1.57
μ	16.3	-13.1	-4.4	-8.6	13.8	-.59	3.47

$\not{E}_T^{l2}$	E_T^{l1e}	E_T^{l2e}	E_T^{l1j}	η^{l1j}	ϕ^{l1j}	E_T^{l2j}	η^{l2j}	ϕ^{l2j}
33.5	61.8	55.8						

$\mathcal{I}$	χ_e^2	σ_{trk}	dE/dx	VTX dE/dx	f_{EM}	ϵ_{TRD}	L_e
.038	23.609	1.713	1.085	.000	.985	.096	.023

CHF	EMF	CHF−EMF
.052	.600	-.548
.000	.995	-.995
-.006	.597	-.603
.000	1.000	-1.000
.006	.563	-.558

vertex-z	e z-int.	H_T	$\mathcal{A}$	M_T^W	p_T^W	$\mathcal{L}$	MI tool
29.915	34.956	143.203	.077	1.242	109.163	-3.000	1

Appendix C

Electron Finding Efficiency

The efficiency of the electron quality requirements was measured using $Z \to ee$ data. By imposing good electron quality requirements on one of the two electrons candidates, called the 'tag,' the background can be reduced to a low (and measurable) level—leaving the other electron, the 'probe,' for a nearly unbiased test of the efficiency.

Data taken with the trigger `em1_eistrkcc_esc` were used. Offline, events having two EM clusters with $p_T > 20$ GeV and $\eta_{det} \leq 20$ were selected. The requirements for the tag were $\chi^2_e < 100, \mathcal{I} < 0.15$, and a match to a trigger Level 2 cluster satisfying the `eis` conditions. Each of the two clusters in an event were considered as the probe if the other met the tag conditions. For each probe that satisfied $\mathcal{I} < 0.1$ the invariant mass m_{ee} of the pair of clusters was entered in a histogram, shown in Figure C.1 or C.2 depending on whether the probe was in the CC or EC. Also shown in Figures C.1 and C.2 are the m_{ee} distributions for probe electrons which, in addition to meeting the isolation requirement, had an associated track from the principle interaction vertex to the cluster, and the m_{ee} distributions for probe electrons which satisfied all of the tight electron conditions.

The number of entries in the signal region 80 GeV/c^2 $< m_{ee} <$ 100 GeV/c^2 was counted for each distribution and the background was subtracted to estimate

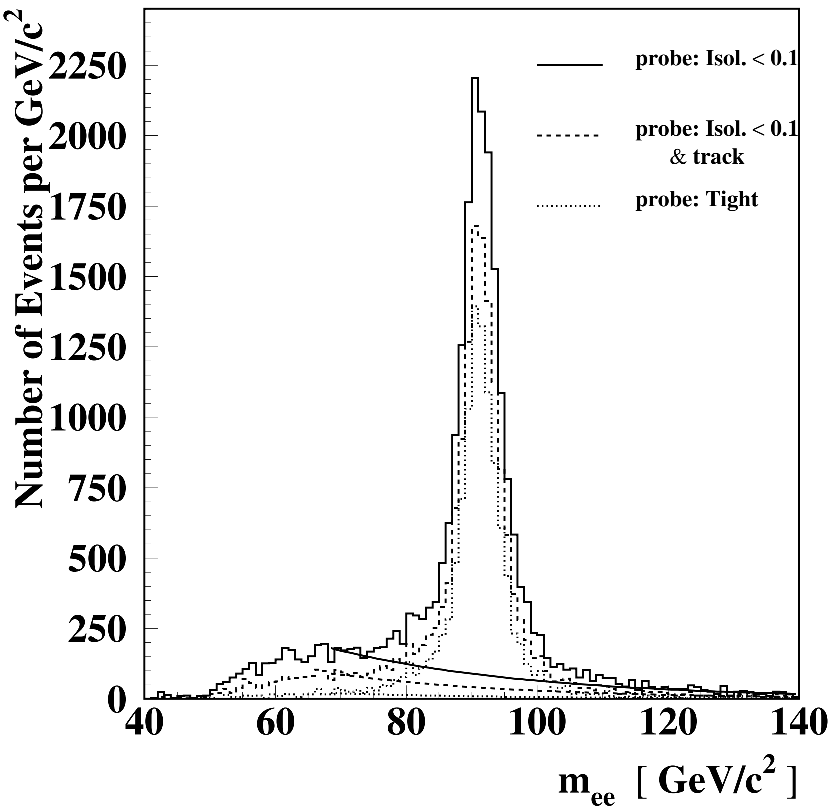

Figure C.1: Mass of electron candidate pairs with a good tag electron and a probe electron in the CC. The smooth curves are the background distributions determined from the fit.

the number of real electron probes. The track finding efficiency ε_{trk} is the ratio of the number of real electron probes passing the isolation cut and having a track to the number which pass the isolation cut. The quality cut efficiency ε_q is the ratio of the number isolated probes having a track and passing the remaining tight electron requirements, *viz.* the likelihood and χ^2 cuts, to the number which are isolated and have a track.

Two background subtraction methods were used. In the first method the background estimate was the number of entries with 60 GeV/c^2 $< m_{ee} <$ 70 GeV/c^2 or 110 GeV/c^2 $< m_{ee} <$ 120 GeV/c^2. In the second method the distribution from 68

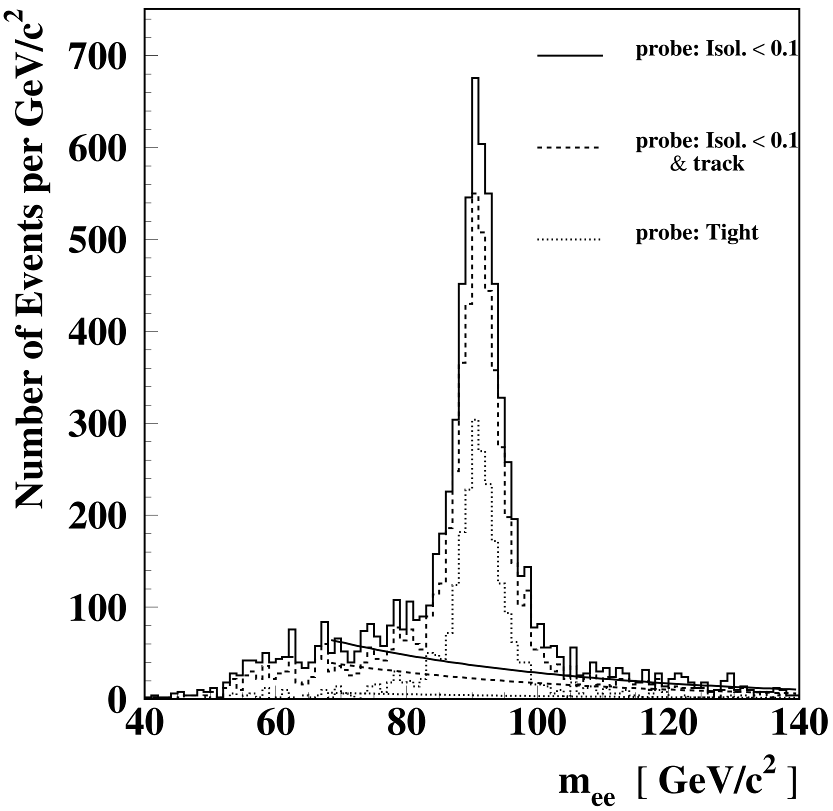

Figure C.2: Mass of electron candidate pairs with a good tag electron and a probe electron in the EC. The smooth curves are the background distributions determined from the fit.

GeV/c^2 to 140 GeV/c^2 was fit to a function representing the sum of a background and a signal shape. The background shape was taken to be an exponential with both the slope and normalization free parameters. This form accurately describes the shape of the invariant mass distribution for EM clusters in a control sample where both clusters were required to fail good electron quality conditions. The fit to the control sample is shown in Figure C.3. The values of the slope for the CC and EC control samples are consistent with the values for the corresponding Z candidate samples. The shape of the signal distribution was obtained by convoluting a gaussian kernel with the mass distribution for Z boson events calculated

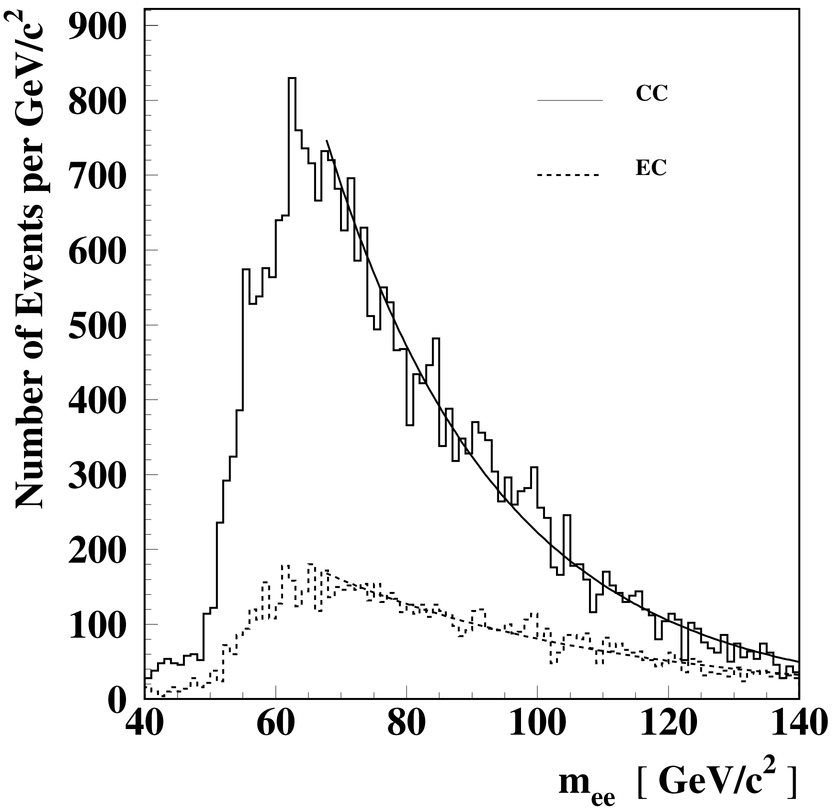

Figure C.3: Mass of EM cluster pairs for the background control sample. The smooth curves are fits to an exponential.

using ISAJET. The normalization, width of the gaussian, and location of the mass peak were allowed to float.

The results using the second background subtraction method for the CC (EC) are $\varepsilon_{trk} = 0.753 \pm 0.004 \pm 0.002$ ($0.825 \pm 0.007 \pm 0.004$) and $\varepsilon_q = 0.794 \pm 0.003$ $\pm\ 0.008$ ($0.513 \pm 0.008 \pm 0.001$), where the first error is statistical and the second is the difference with the first background subtraction method. The dependence of these quantities on the number of jets in the event is shown in Figures C.4 and C.5.

The EC values appear to trail off at high jet multiplicity, although the statistics are poor for events with jets. This is not a major concern because only about 7% of the acceptance for $t\bar{t}$ events is from electrons in the EC. There is not a clear

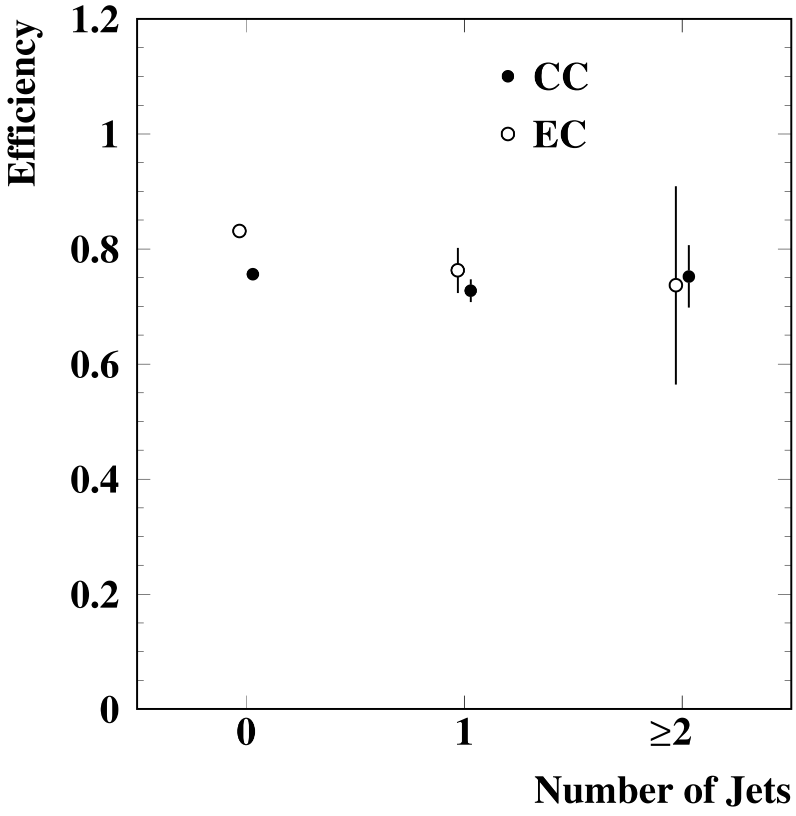

Figure C.4: Dependence of ε_{trk} on jet multiplicity.

trend in the values for the CC but again the statistics are low for the data with two or more jets. It has been found in studies of simulated data— including noise and multiple interactions [77] and the the full `GEANT` detector simulation— that the inefficiency in finding the track of an electron due to errors in locating the principle interaction vertex (see Section 5.3.2) should decrease with jet multiplicity because of the increase in the number of tracks from the principle interaction [47]. The effect of always identifying the correct interaction vertex was studied by imposing the additional requirement that tag electrons have a track consistent with the reconstructed principle vertex. The efficiencies then improve to $\varepsilon_{trk} = 0.831 \pm$

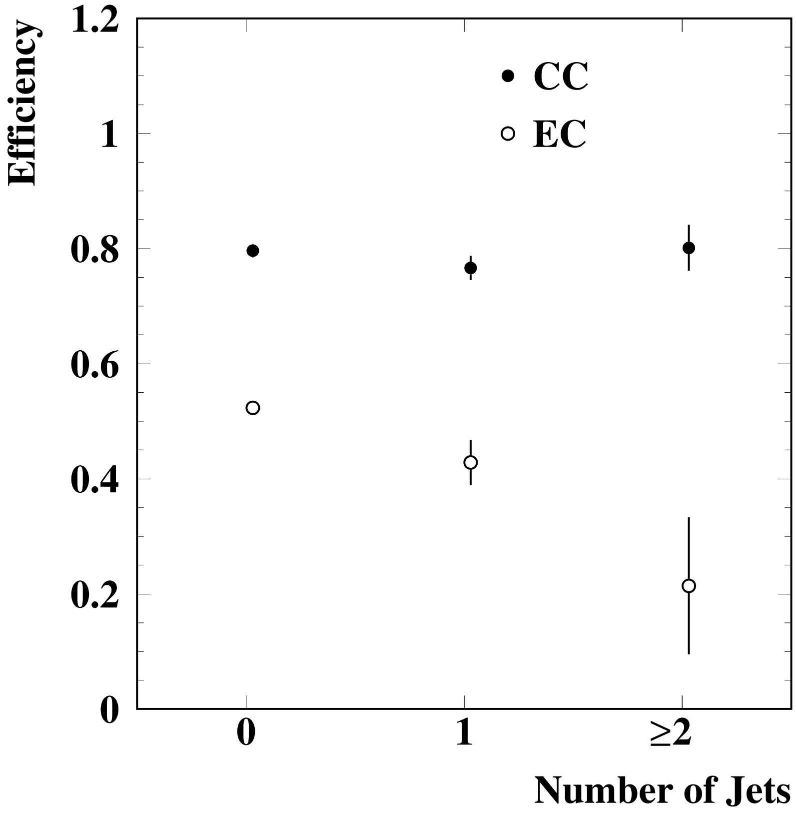

Figure C.5: Dependence of ε_q on jet multiplicity.

0.006 ± 0.005 ($0.852 \pm 0.010 \pm 0.004$) and $\varepsilon_q = 0.812 \pm 0.007 \pm 0.006$ ($0.534 \pm 0.010 \pm 0.001$).

For consistency with the analyses of other $t\bar{t}$ signatures the values used to determine the weights applied to Monte Carlo events were the ones shown in Table C.1.

	CC	EC
ε_{trk} (simulation)	95.1 ± 1.0	96.0 ± 2.0
ε_{trk} (data)	82.8 ± 2.0	86.6 ± 2.0
ε_{q} (data)	81.9 ± 2.0	54.9 ± 4.0

Table C.1: Electron efficiencies [%].

Appendix D

Extracting a Systematic Error for the Tag Rate

One approach to studying the systematic uncertainty in using the tag rate to predict the number of $W+$jets events with a tagged jet is to look at the accuracy with which we can predict the number of tagged events in several (N) control samples. In the ith data set we count the number of events with a tagged jet x_i and assume each x_i is a random number taken from a Poisson distribution with mean μ_i. The true value of μ_i is not known. From the measured tag rate we obtain an estimate of μ_i, which we call y_i. Let us assume that this estimate has a fractional uncertainty α. Specifically, assume that y_i is a random number taken from a Gaussian distribution with mean μ_i and standard deviation $\alpha\mu_i$.

The probability to obtain our observed values $x_1, \ldots, x_N, y_1, \ldots, y_N$ given parameters $\alpha, \mu_1, \ldots, \mu_N$ is then

$$L(x_1, \ldots, x_N, y_1, \ldots, y_N | \alpha, \mu_1, \ldots, \mu_N) = \prod_{i=1}^{N} P(x_i, y_i | \alpha, \mu_i) \qquad \text{(D.1)}$$

where

$$P(x_i, y_i | \alpha, \mu_i) = \frac{1}{\sqrt{2\pi\mu_i}} e^{-\frac{1}{2}\frac{(x_i-\mu_i)^2}{\mu_i}} \times \frac{1}{\sqrt{2\pi}\,\alpha\mu_i} e^{-\frac{1}{2}\left(\frac{y_i-\mu_i}{\alpha\mu_i}\right)^2} \qquad \text{(D.2)}$$

In Equation D.2 the Poisson distribution is approximated by a Gaussian.

The maximum likelihood estimate of the parameter α is the solution of the equation $\partial L/\partial\alpha = 0$. This solution depends on the values of the N 'nuisance' variables $\mu_1, \ldots, \mu_N$. The likelihood function can be simplified (at the expense of information about $\mu_1, \ldots, \mu_N$) by considering only the differences $D_i = x_i - y_i$. Instead of Equation D.1 we then have

$$L^D(D_1, \ldots, D_N|\alpha, \mu_1, \ldots, \mu_N) = \prod_{i=1}^{N} \int_{-\infty}^{\infty} dx_i \int_{-\infty}^{\infty} dy_i \, P(x_i, y_i|\alpha, \mu_i)\, \delta(D_i - x_i + y_i) \tag{D.3}$$

Evaluating the integrals gives

$$L^D = \prod_{i=1}^{N} \frac{1}{\sqrt{2\pi(\alpha^2\mu_i^2 + \mu_i)}}\, e^{-\frac{1}{2}\frac{D_i^2}{\alpha^2\mu_i^2+\mu_i}} \tag{D.4}$$

Using

$$\frac{\partial \ln L^D}{\partial\alpha} = \sum_{i=1}^{N} -\frac{\alpha\mu_i^2}{\alpha^2\mu_i^2 + \mu_i} + \frac{D_i^2\alpha\mu_i^2}{(\alpha^2\mu_i^2 + \mu_i)^2} \tag{D.5}$$

the condition

$$\frac{\partial \ln L^D}{\partial\alpha} = 0 \tag{D.6}$$

becomes

$$\sum_{i=1}^{N} \frac{(D_i/\mu_i)^2 - \alpha^2 - 1/\mu_i}{(\alpha^2 + 1/\mu_i)^2} = 0 \tag{D.7}$$

We approximated μ_i by y_i and solved Equation D.7 numerically.

REFERENCES

[1] S. Weinberg, Phys. Rev. Lett. **19**, 1264 (1967).

A. Salam in *Elementary Particle Theory*, ed. N. Svartholm (Almquist and Wiksells, Stockholm, 1969) p. 367.

S.L. Glashow, J. Iliopoulos, and L. Maiani, Phys. Rev. **D2**, 1285 (1970).

[2] S.W. Herb *et al.*, Phys. Rev. Lett. **B295**, 136 (1977).

[3] For reviews of the history of the search for the top quark through its discovery and references to the original literature, see

M. Mangano and T. Trippe, Phys. Rev. D **54**, 309 (1996).

C. Campagnari and M. Franklin, Rev. Mod. Phys.,

[4] D0 Collaboration, S. Abachi *et al.*, Phys. Rev. D **52**, 4877 (1995).

[5] W. Bartel *et al.*, Phys. Lett. **B146**, 437 (1984).

[6] See, for example, the discussion in

G. L. Kane, 'Top Quark Topics' in *Gauge Bosons and Heavy Quarks: Proceedings of the Eighteenth SLAC Summer Institute on Particle Physics*, p. 123. J. Hawthorne, ed. 1990.

[7] P. Langacker, Phys. Rev. Lett. **63** 1920 (1989).

[8] J. Ellis and G.L. Fogli, Phys. Lett. **B232** 139 (1989).

[9] Albajar *et al.*, Phys. Lett. **B257** 459 (1991).

[10] CDF Collaboration, F. Abe *et al.*, Phys. Rev. D **50**, 2966 (1994).

[11] D0 Collaboration, S. Abachi *et al.*, Phys. Rev. Lett. **74** 2422 (1995).

[12] D0 Collaboration, S. Abachi *et al.*, Phys. Rev. Lett. **74**, 2632 (1995).

[13] CDF Collaboration, F. Abe *et al.*, Phys. Rev. Lett. **74**, 2626 (1995).

[14] D0 Collaboration, S. Abachi *et al.*, to be published in Phys. Rev. Lett.

[15] D0 Collaboration, S. Abachi *et al.*, submitted to Phys. Rev. Lett.

[16] D0 Collaboration, S. Abachi *et al.*, to be published in Phys. Rev. Lett.

[17] S.L. Glashow, E. E. Jenkins, Phys. Lett. **196B**, 233 (1987).

[18] C. Hill, S. Parke. Fermilab Report No. FERMILAB-PUB-93/397-T, 1993.

[19] The Particle Data Group, R.M. Barnett *et al.*, "Review of Particle Physics." Phys. Rev. D **54**, 1 (1996).

[20] F.J. Gilman, K. Kleinknecht, and B. Renk, Phys. Rev. D **54**, 94 (1996).

[21] A summary of the electroweak data and their implications is given in P. Langacker and J. Erler, Phys. Rev. D **54**, 85 (1996).

[22] I. Hinchliffe, Phys. Rev. D **54**, 77 (1996).

[23] E. Laenen, J. Smith, and W. van Neerven. Phys. Lett. B **321**, 254 (1994).

[24] E. Berger and H. Contopanagos, Phys. Lett. **361B**, 115 (1995) and Phys. Rev. D **54**, 3085 (1996).

[25] S. Catani, M. L. Mangano, P. Nason and L. Trentadue, Phys. Lett. **378B**, 329 (1996).

[26] J. Thompson, FERMILAB-TM-1909, 1994.

[27] D0 Collaboration, S. Abachi *et al.*, Nucl. Instrum. Methods Phys. Res., Sect. A **338**, 185 (1994).

[28] W. R. Leo, *Techniques for Nuclear and Particle Physics Experiments.* (Springer-Verlag, Berlin, 1987), pp. 119-148.

[29] D0 Collaboration, S. Abachi *et al.*, Phys. Rev. Lett. **77**, 3309 (1996).

[30] D0 Collaboration, S. Abachi *et al.*, Phys. Rev. Lett. **74**, 3548 (1995).

[31] M. Narain and U. Heintz, "A Likelihood Test for Electron ID." DØNote 2386, 8 December 1994 (unpublished).

[32] A. Pluquet, "The TRD_ANALYSIS Package." DØNote 1899, 24 September 1993 (unpublished).

[33] J. Bantly *et al.*, "The Level 0 Trigger for the DØ Detector." DØ Conf-94-1, IEEE Trans. Nucl. Sci. 1993.

[34] E. Gallas, "The MTC Package (Muon Tracking in the D0 Calorimeter)." DØNote 2066, 23 August 1995 (unpublished).

[35] J. Butler, "D0 Muon Chamber Pulse Heights: June 1992 to September 1994 Shutdown." DØNote 2319, 26 October 1994 (unpublished).

[36] T. Marshall and H. Haggerty, "Crud Removal from Muon Drift Chamber Wires using 'ZAP' Cleaning." DØNote2556, 8 September 1995 (unpublished).

[37] J. Butler, "EF Muon ID for b-Tagging in the Post-Zap Era." DØNote 2602, 28 June 1995 (unpublished).

[38] J. Thompson, "Search for the Top Quark in the Muon+Jets Channel at DØ." Ph. D. Thesis, State University of New York at Stony Brook, 1994.

[39] S. Parke, X International $\overline{p}p$ Workshop, Fermilab, Ill., 1995. FERMILAB-Conf-95/307-T.

[40] N. Grossman,"A Study of Hot Cells and Jets: Should We Add Hotcells Back into Events." DØNote 2525, 10 March 1995 (unpublished).

[41] D. Baden, "Searching for top in $e+$jets." DØNote 1506, 20 Oct. 1992 (unpublished).

[42] V. Barger and R. Phillips, *Collider Physics*, (Addison-Wesley, Reading, MA, 1987), p. 281.

[43] G. Marchesini *et al.*, Computer Phys. Commun. **67**, 465 (1992).

[44] R. Brun *et al.*, `GEANT` Users's Guide v3.14, CERN Program Library (unpublished).

[45] F. Paige and S. Protopopescu, BNL Report BNL38034, 1986 (unpublished), release v. 7.21.

[46] W. Dharmaratna, R. Raja and C. Stewart, "The D0 Shower Library-Version 2.0." DØNote 1730, 12 May 1993 (unpublished).

[47] M. Narain, private communication.

[48] T. Diehl and P. Quintas, "MU_SMEAR PACKAGE", 8 April 1994 (unpublished).

[49] Paul Quintas, "Reconstruction and Selection Efficiencies for High p_T Muons in Run 1B." DØNote 2865, 29 February 1996 (unpublished).

[50] Dave Hedin, "Run 1b Muon Event Scanning," DØNote 2712, 1995.

[51] John Hobbs, private communication.

[52] D0 Collaboration, S. Abachi *et al.*, Phys. Rev. D **53**, 6000 (1996).

[53] DELPHI Collaboration, K. Hamacher *et al.*, contribution 548 to EPS HEP95, Brussels.

[54] A version of the CLEO Monte Carlo `QQ` which can be used with `HERWIG` is available from `ftp.fnal.gov`.

[55] F. Hsieh, R. Partridge, S. Snyder. "Jet Energy Scale Uncertainty for Top Cross Section PRL." DØNote, 25 Mar. 1997 (unpublished).

[56] G. Manning, "Estimation of the Background to $W+$jets and $Z+$jets." DØNote 2452, 20 January 1995 (unpublished).

[57] D0 Collaboration, S. Abachi *et al.*, Phys. Rev. Lett. **77**, 5011 (1996).

[58] John Hobbs, private communication.

[59] T. Stelzer and S. Willenbrock, `hep-ph/9595433`, 31 May 1995.

[60] T. Stelzer, Z. Sullivan and S. Willenbrock, `hep-ph/9705398` 22 May 1997.

[61] H. U. Bengtsson and T. Sjostrand, Comput. Phys. Commun. **46**, 43 (1987).

[62] E. E. Boos *et al.*, in *Proceedings of the XXVIth Recontres de Moriond, High Energy Hadronic Interactions, Les Arcs, France, 1991*, (Editions Frontieres, 1991) J. Tran THan Van, ed., p. 501 and

E. E. Boos *et al.*, in *Proceedings of the Second International Workshop on Software Engineering, Artificial Intelligence and Expert Systems for High Energy and Nuclear Physics, La Londe Les Maures, France, 1992.* D. Perret-Gallix, ed., (World Scientific, 1992), p. 665.

[63] A. P. Heinson, A. S. Belyaev and E. E. Boos, `hep-ph/9612424`, 19 Dec. 1996.

[64] F. A. Berends, H. Kuijf, B. Tausk and W. T. Giele, Nucl. Phys. **B357**, 32 (1991).

[65] J. Butler *et al.*, "Measurement of the Top Quark Production Cross Section Using Lepton+Jets Events." DØNote 2978, 12 Dec. 1995 (unpublished).

[66] H. Zhu, "Measurement of the $t\bar{t}$ production cross section in the $t\bar{t} \rightarrow \mu+$ Jets $+\mu$–tag channel." D0Note 3194, 27 March 1997 (unpublished).

[67] R. Kehoe, "Search for the Top Quark in Dielectron Final States at $\sqrt{s} = 1.8 TeV$ and Measurement of the Response of the DØ U/Lar Calorimeter to Jets." Ph. D. Thesis, University of Notre Dame, 1997 (unpublished).

[68] J. Bantly and R. Hall, "Top Counting in the Dimuon Channel: DØ Analysis of Run 1." DØNote 3088, 7 February 1997 (unpublished).

[69] D. Chakraborty, "VECBOS at D0: A Sorcerer's Manual." DØNote 2337, 25 April 1994 (unpublished).

[70] S. Saritepe, "Future Collider Runs in the Tevatron: Beam-Beam Simulation Results." FERMILAB-FN-563, April 1991.

[71] N. Amos, *et al.*, "Luminosity Calculations for DØ." DØNote 2031, Jan. 1994 (unpublished).

[72] J. Bantly, *et al.*, "Improvement to the DØ Luminosity Monitor Constant." DØNote 2544, 29 Dec. 1995 (unpublished).

[73] N. Amos *et al.*, Phys. Lett. **B243**, 158 (1990).

[74] CDF Collaboration, F. Abe *et al.*, Phys. Rev. D **50**, 5550 (1994).

[75] M. M. Block and R. N. Cahn, Rev. Mod. Phys. **57**, 563, April 1995.

[76] Tom Rockwell, private communication.

[77] A. Mincer, P. Nemethy and A. Boehnlein, "The Noisy Package." NOISY package documentation, 20 September 1993 (unpublished).

[78] E. Flattum, "A Measurement of the W Boson Mass in $p\overline{p}$ Collisions at $\sqrt{s} = 1.8$ TeV." Ph. D. Thesis, Michigan State University, 1996 (unpublished).

[79] W. Carvalho and T. Taylor, "Multiple Interaction Tool Study for Run 1." DØNote 2798, 5 December 1995 (unpublished).

[80] CDF Collaboration, F. Abe *et al.*, Phys. Rev. D **50**, 5550 (1994).

[81] D. Amidei *et al.*, "Future Electroweak Physics at the Fermilab Tevatron: Report of the TeV2000 Study Group," Fermilab Report No. FERMILAB-PUB-96/082-T, 1996.